DESIGN OF BIOINSPIRED CONDUCTIVE SMART TEXTILES

Hussain R. Rizvi, B.S., M.S.

Dissertation Prepared for the Degree of:

DOCTOR OF PHILOSOPHY

UNIVERSITY OF NORTH TEXAS

August 2017

APPROVED:

Nandika A. D'Souza, Major Professor
Sheldon Q. Shi, Committee Member
Vijay Vaidyanathan, Committee Member
Xiaohua Li, Committee Member
Hyeonu Heo, Committee Member
Kuruvilla John, Chair of the Department of Mechanical and Energy Engineering
Costas Tsatsoulis, Dean of College of Engineering
Victor R. Prybutok, Vice Provost of the Toulouse Graduate School

Rizvi, Hussain R. *Design of Bioinspired Conductive Smart Textiles*. Doctor of Philosophy (Mechanical Engineering), August 2017, 139 pp., 22 tables, 56 figures, chapter references.

Electrically conductive fabrics are one of the major components of smart textile that attracts a lot of attention by the energy, medical, sports and military industry. The principal contributors to the conductivity of the smart textiles are the intrinsic properties of the fiber, functionalization by the addition of conductive particles and the architecture of fibers. In this study, intrinsic properties of non-woven carbon fabric derived from a novel linear lignin, poly-(caffeyl alcohol) (PCFA) discovered in the seeds of the vanilla orchid (*Vanilla planifolia*) was investigated. In contrast to all known lignins which comprise of polyaromatic networks, the PCFA lignin is a linear polymer. The non-woven fabric was prepared using electrospinning technique, which follows by stabilization and carbonization steps. Results from Raman spectroscopy indicate higher graphitic structure for PCFA carbon as compared to the Kraft lignin, as seen from G/D ratios of 1.92 vs 1.15 which was supported by a high percentage of graphitic (C-C) bond observed from X-ray photoelectron spectroscopy (XPS). Moreover, from the XRD and TEM a larger crystal size (Lc=12.2 nm) for the PCFA fiber was obtained which correlates to the higher modulus and conductivity of the fiber. These plant-sourced carbon fabrics have a valuable impact on zero carbon footprint materials. In order to improve the strength and flexibility of the non-woven carbon fabric, lignin was blended with the synthetic polymer poly acrylonitrile (PAN) in different concertation, resulting in electrical conductivity up to (7.7 S/cm) on blend composition which is enough for sensing and EMI shielding applications. Next, the design of experiments approach was

used to identify the contribution of the carbonization parameters on the conductivity of the fabrics and architecture of the fibers, results show carbonization temperature as the major contributing factor to the conductivity of non-woven fabric. Finally, a manufacturing procedure was develop inspired by the architecture of plant fibers to induce controlled porosity either on the skin or core of fibers which results in stiffness and flexibility in the fibers. Coaxial electrospinning and physical foaming (CO_2 foaming) techniques were utilized to create the hierarchical fiber architecture. Finite Element model was developed to design for mechanical properties of the bioinspired fiber mesh. Results show the polymers contributes less in a coaxial design as compared to the individual fibers for mechanical properties. This manufacturing method can use for hierarchical functionalization of fibers by adding conductive nanoparticles at different levels of fiber cross-section utilized for sensing applications in sports and medical industry.

ACKNOWLEDGEMENTS

First of all, I would like to gratefully thank my advisor, Dr. Nandika Anne D‘Souza for her kind support, mentoring, and encouragement during the whole process of accomplishing my dissertation.

To my committee members, Dr. Sheldon Shi, Dr. Vijay Vaidyanathan, and Dr. Xiaohua Li, for their comments and suggestions. It has been an honor and privilege for me to have you all on my committee.

I am also grateful to the CART staff for their support during my graduate study and Craig Collins, Robbin Shull and John Sawyer for helping me at all times.

To my invaluable group of supportive friends: Shaheer Iqbal, Shakila Sultana, Andres Garcia, Mangesh Nar, MD Salah Uddin, Reinaldo Santos, Nelson Martinez, Michael Mendoza, Jonova Thomas, Changlei Xia, Zach Hoyt, Amaal Al-Shenawi, Yoni Mercier, and Kayode Oluwabunmi.

Lastly to my wife, Komal, my brothers Hasan, Zain and Ahmed and my Parents who supported me unconditionally.

TABLE OF CONTENTS

Page

LIST OF TABLES

Page

LIST OF FIGURES

Page

CHAPTER 1

BACKGROUND

During the last few decades, breakthroughs in fiber materials and manufacturing processes have led to a transformation in textiles. This is being referred to as the dawn of smart textiles [1]. The term “Smart textiles” refers to a wide range of products that increase the functionality of common fabrics. Lightweight structural fabric for use in bullet proof vests [2], flexible surface sensors that can be attached to the skin to detect upcoming medical events [3], motion sensing wearable textiles [4], and wearable lightweight solar textiles for the next generation clothing [5] are few of the innovations being considered. With the advancement in manufacturing processes, non-woven fabric can be manufactured having individual fibers as small as 50-100 nm in diameter. These dimensional characteristics have made it feasible for water filtration systems that can both filter solids and microbes [6], provide extremely high areal capacity for charge storage in batteries [7] and piezo-functionality for power generation applications [8]. In the near future, we can expect fabrics having the ability to observe their surroundings, communicate, store and convert energy, change their color and regulate temperature.

One of the major areas of smart textiles that attract a lot of attention by the sports, medical, military and energy industry is electrically conductive fabrics. The first generation of conductive smart textiles came in the market with Industrial Clothing Design Plus (ICD+) line coats a joint venture of Levi’s and Philips at the end of the 1990s. The coat uses the conventional materials and was designed to accommodate external devices such as the microphone, earphone, remote control, a mobile phone, and an MP3 player. Since then the smart textiles are rapidly evolving. Research in the

2000s was mainly targeted to develop textile electrodes for heart rate monitoring for health, sports, and military applications. ECG electrodes made by combinations of stainless steel and polyester [9], reconstruction of the body posture by embedding piezoelectric sensors on the fabrics [10], wearable motherboards to detect bullet wounds [11] and Intellitex baby suit [12] to monitor sudden infant death syndrome are examples of that era where they used optical fibers and stainless steel yarn embroidered on the suit for detection. A major drawback was the compatibility of these fibers with the regular textile fibers due to its stiff and abrasive nature. These challenges led to research directed toward the development of new conductive materials and structures that are compatible with the regular textiles, low cost, environmentally stable and mechanically strong and flexible. The functionality of these conductive textiles is mainly attributed to the intrinsic conductivity of the fiber materials [13] and functionalization by the addition of conductive nanoparticles. [14] The use of fiber cross-sectional design has not been considered. The D'Souza laboratory has worked with faculty in biology investigating the contributions of architecture and chemical composition in natural fibers. The goal of using bioresources by themselves are critical as awareness of finite mineral and fossil fuel resources and a need for renewable materials becomes a pressing need. The conversion of bioresources to valuable engineering products is another frontier. In particular carbon is a material source that is is consumed in the billions of pounds. Using bioresources is critical

In this dissertation, studies have been carried out on the intrinsic properties of fiber material and hierarchical fiber architecture for conductive smart textiles. A novel linear lignin from poly caffeyl alcohol (PCFA) has being studied to produce textile based

non-woven conductive carbon fabric using a low-cost electrospinning technique. The fabric shows superior mechanical and electrical properties being derived from a biological source. Different fiber material composition and architecture was investigated to improve strength, conductivity, and flexibility of the non-woven fabric by blending PCFA with Poly acrylonitrile (PAN) and Poly ethylene oxide (PEO) polymers. A manufacturing technique was developed to engineer a bioinspired architecture of the fibers by inducing controlled porosity on the surface or core of fibers. A finite element model was developed to design the fabric for mechanical properties. This manufacturing method can use for hierarchical functionalization of fibers by adding conductive nanoparticles at different levels of fiber cross-section.

In this chapter, the background to the elements of this dissertation is given. First, we review the intrinsic materials properties for carbon fibers and challenges due to the environment and energy concern (1.1). Next, the architecture of biological fibers and attributes associated with it are reviewed (1.2). Then the manufacturing techniques to create synthetic fibers are provided in section1.3. Finally, the scope of the dissertation is presented in section 1.4.

1.1 Intrinsic Properties of Carbon Fibers

Carbon fibers have become an essential engineering material for design and manufacturing. The increasing surface area on the fiber surface through porosity lends itself to a high surface area substrate whose interfacial coupling has been shown to counter the negatives from high defect density in carbon formed in high volumes [15]. Carbon fiber applications cover a diverse spectrum and its usage is expected to reach

90k tons by 2020 [16]. The mechanical, thermal and electrical conductivity of the fibers are correlated to the graphitic structure and orientation of the planes [17]. Yarns from carbon have been shown to have value in the battery, fuel cell electrodes and textiles [18]. The conductivity has proven to have a contribution to mitigating biofouling in paints by providing an electric pathway for cathodic protection [19]. In lithium ion batteries they have increased electrical connectivity and mechanical integrity to enhance cycle life [20-22]. In fuel cells, they are used in Pt free catalysts [23,24] and enhance resistance to photooxidation in solar cells [22]. For water purification, they provide mechanical and electrochemical robust networks with controlled nanoscale porosity. These are able to electrochemically oxidize organic contaminants [25], bacteria and viruses [26]. As biosensors functionalized carbon demonstrates high electrical impedance [27] and optical properties [28] in response to adsorption of targets onto the surface. Biocompatibility has been associated with the surface chemistry enabling it to be engineered [29].

The use of lignin in carbon formation is associated with growing consumption of carbon [15] and environmental /energy concerns. Currently, carbon fiber is manufactured predominantly from polyacrylonitrile (PAN) with a small fraction originating in pitch. PAN-based carbon fiber uses the acrylonitrile monomer which has a high cost [30]. Additional graphitization with Argon has increased the carbon yield to 80% for PAN fibers [31]. The high temperature of the PAN process contributes to a larger energy footprint and the consequent impact on materials formed from them for carbon footprint calculations. Because of such concerns, the development of a source of carbon fiber based on plant materials is being strongly promoted [32]. Compared to

PAN and pitch precursors, lignin is cost effective and has an aromatic structure that is carbon rich for higher carbon yield [33]. The conductivity values of lignin based fabrics is reported in between (0.2-21.3 S/cm) based on different processing conditions [34]. Therefore there is considerable interest in determining whether lignin can be developed as a cost-effective feedstock for carbon-based applications, potentially as a byproduct of the processing of lignocellulosic liquid biofuels [35]. Polyethylene oxide (PEO) [36-38] and PAN [39,40] have both been considered as optimal polymers to be blended with lignin to form carbon fibers with flexibility and strength required for weaving operations.

1.1.1 Lignin

Among plant resources, lignocellulose is a dominant constituent of plant dry matter, consisting of a complex of cellulose and hemicellulose embedded in lignin. Lignin is the second most abundant natural polymer on earth, produced by oxidative polymerization of *p*-hydroxycinnamyl alcohols (monolignols). Lignins are primarily found in plant secondary cell walls and are particularly abundant in vascular tissues. The presence of this lignin reduces forage digestibility and hinders agro-industrial processes for generating pulp or biofuels from lignocellulosic plant biomass. There has therefore been considerable attention given to reducing lignin content in plant feedstocks and developing value added products for the lignin that is grown [41-44].

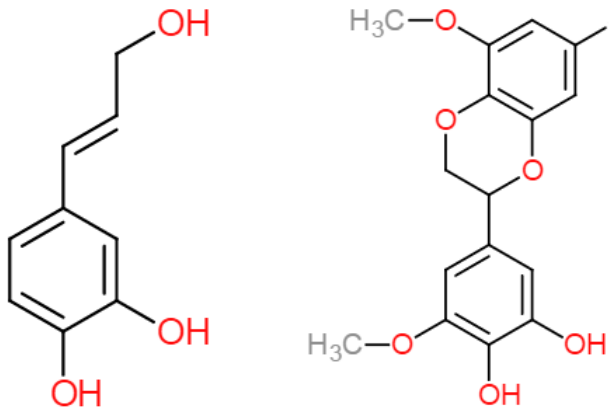

Figure 1-1. Chemical structure of (a) caffeyl alcohol monomer, (b) benzodioxanes unit.

Recently Chen et al. [45-47] discovered that seed coats of a variety of plant species contain a previously unsuspected class of lignin-like molecule made entirely from caffeyl alcohol units (essentially G units lacking the methyl group on the 3-oxygen) which are not found in softwood, hardwood or grass lignin. This is termed as C-lignin or PCFA. Figure 1-1 shows the chemical structure of caffeyl alcohol monomer and its C subunit. Analysis of the lignin monomer composition of seed coat of *V. planifolia and* Brazilian cactus *Melocactus salvadorensis* by thioaciolysis indicates that the lignin is a linear polymer derived almost totally from caffeyl alcohol monomers linked head to tail into benzodioxane chains via the 'endwise' radical coupling reactions that typify lignification. Interestingly the β-aryl ether units, which are the dominant linkage units found in both hardwood and softwood lignins derived from coniferyl and sinapyl alcohols, were absent, whereas benzodioxanes were the dominant lignin units accounting for over 98% of the identifiable dimeric units in the polymer.

1.1.2 PAN

PAN is semi-crystalline synthetic organic polymer resin, having a linear formula of $(C_3H_3N)n$. It comes under the category of thermoplastic polymers, however, it only melts at a higher heating rate i.e. above 50 ^{0}C per minute, around 300 ^{0}C [48]. Lower heating rate results in degradation rather than melting. Synthesis of PAN is based on free radical polymerization of acrylonitrile (AN), with vinyl co monomers in a small percentage (1-10%) based on the application. Fibers from PAN are used for ultrafiltration membrane, reverse osmosis and as a precursor to carbon fibers.

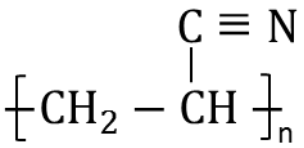

Figure 1-2. Chemical structure of polyacrylonitrile

1.1.3 PEO

Polyethylene oxide is a nontoxic synthetic polyether having high molecular weight. It is soluble in water as well as organic solvents. It is also a thermoplastic polymer which gives processing flexibility. PEO is mostly synthesized by anionic ring-opening polymerization of ethylene oxide. It is used in a variety of applications including pharmaceutical formulations due to the absence of immunogenicity [49], mining and cleaning products. Figure 1-3 shows the chemical structure of polyethylene oxide.

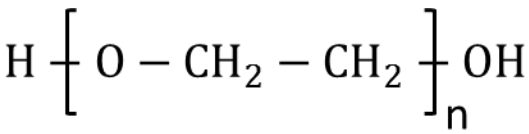

Figure 1-3. Chemical structure of polyethylene oxide.

1.2 Bioinspired Architecture

Nature provides the architectural and performance incentive for new fiber architectures to be considered. The structural and chemical properties of plant fibers arise in response to the conditions of growth and development. Plant fibers are the cell-wall remains of specialized cells that provide structure and support to the plant. Cell walls expand with growth but also resist the cells internal pressure as an elastomer-plastomer leading to the final size and shape of cells. Walls are composites of interpenetrating polymeric networks of cellulose, hemicelluloses, pectins, glycoproteins, and lignin (a phenolic polymer that cross-links with other components of the wall). Remarkably, through natural design, a low modulus natural fiber achieves a specific stiffness that rivals synthetic glass fiber. In a natural fiber, the cell wall surrounds the living protoplast, and the space occupied by the protoplast forms a central hollow pore through the fiber which along with chemical composition, contributes significantly to plant-fiber viscoelastic behavior [50-52]. D'Souza et al [53-55] show that by controlling the retting of the fiber, the cross section of the fibers can be made porous or non-porous depending on the processing of the fiber from harvested to dried (retted). This porosity coupled to chemical changes (increased fiber age/growth lead to increased cellulose content) lead to both an elastic and viscous response.

1.3 Fiber Manufacturing

Conversion of polymer to synthetic fibers was first introduced industrially in the late 19th century. From then different techniques have emerged however all of then follow a similar principle i.e. a viscous solution of polymer is passed through fine holes, the liquid jet hardens to form a solid fiber.

1.3.1 Spinneret

Polymer fiber spinning techniques require the solid state of polymer to be converted into liquid, gel, melt or emulsion form. This can be achieved by either dissolving the polymer in a solvent or heating to form a melt. This lowers the entanglement of polymer chains allowing them to move freely. Then the solution is passed through a spinneret (a device having small holes), to develop fine jets of solution, the solvent evaporates resulting in fiber filament. Different names have been given depending upon the initial polymer state including solution spinning, melt spinning, gel spinning, and emulsion spinning.

1.3.2 Extrusion

Extrusion is one of the high throughput fiber manufacturing process, in which the polymer in the form of pellets, granules or powder along with the colorant or additives is fed down into the extruder. The polymer is gradually melted by the mechanical mixing of rotating screw and temperature profile applied along the length of the barrel. As the melt reaches the end of the screw it moves across the beaker plate which changes the motion of the melt from rotational to longitudinal. The melt is then passed through a die to give the required shape. For fibers a circular die is normally used, molten after die is cooled down to solidified either in air or water and collected on spools.

1.3.3 Electro-Spinning Process

The ability to create uniform fibers having diameters up to few nanometer has made the electrospinning approach revive in last decade. Electrospinning works on the

principle of electrostatic charge difference between the tip of the ejecting needle and the collector, the polymer solution is subjected to high voltage which induces a polarity to the solution causing it to be attracted to the opposite polarity charge. Due to the application of high voltage, the electrically charged solution formed a conical tip at the end of the needle also known as Taylor's cone. The polymer solution undergoes two types of electrostatic forces, first is due to the electrostatic repulsion in between the surface charges of the solution while second is the coulombic force generated from the externally applied voltage. The charged liquid forming a Taylor's cone is elongated due to the application of an external electric field. Once the electrostatic repulsion overcomes the surface tension of the solution, the liquid starts ejecting from the tip of Taylor's cone. During the flight of the jet, the solvent starts evaporating and current flow shifts from Ohmic to connective currents as the charges moves to the surface of the fiber. The jet undergoes bending instabilities which start with small bends and increases exponentially until it reaches the collector. Figure 1-4 shows the pictorial description of the fiber spinning mechanism.

After the initial straight path, the jet undergoes the bending perturbations, which grows to form a coil like structure with increasing trajectory. Each perturbation causes an elongation of the jet and reduces the dimension of the fiber. The number of bending perturbations varies based on the intrinsic properties of the fluid and operating parameters are mainly governed by the electrostatic forces. Figure 1-5 shows the graphical representation of the bending instabilities of the jet by Reneker et al. [56].

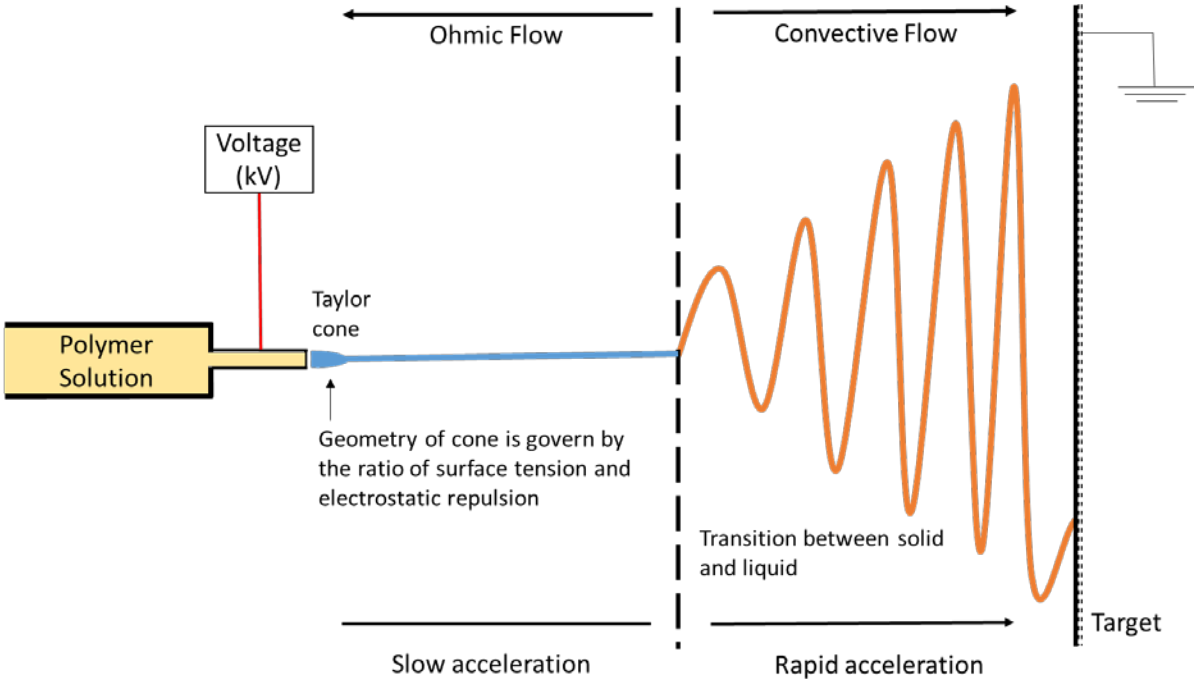

Figure 1-4. Fiber formation by electrospinning, adapted from [49].

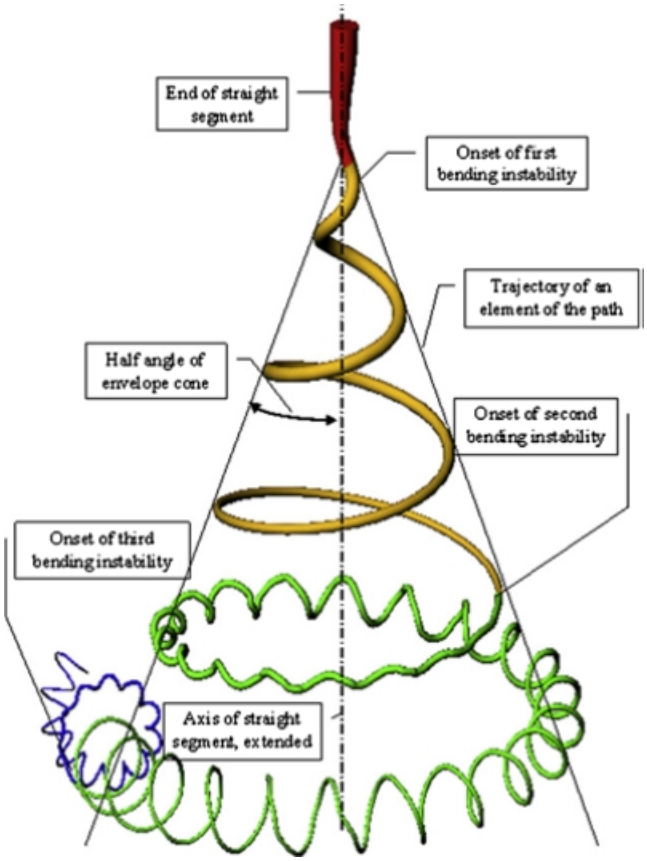

Figure 1-5. Bending instabilities of the electrospun jet by reneker D.H. et al. [50]

The dimensions of the electrospun fibers depend on intrinsic properties of the polymer and operational parameters. Properties such as viscosity [57], conductivity [58], the surface tension of the polymer solution [59] play a key role to achieve beadles smooth fibers of varying dimensions. Apart from three basic factors, fillers [60] and multi-solvents [61] used in preparing the polymers solution can also add functionality and alter the architecture of the fibers [62]. Apart from intrinsic properties of the polymer solution, there are also operational parameters that affect the architecture of the electrospun nanofiber, these include applied voltage [63], needle diameter, collector distance, flow rate, temperature, humidity, and pressure [64].

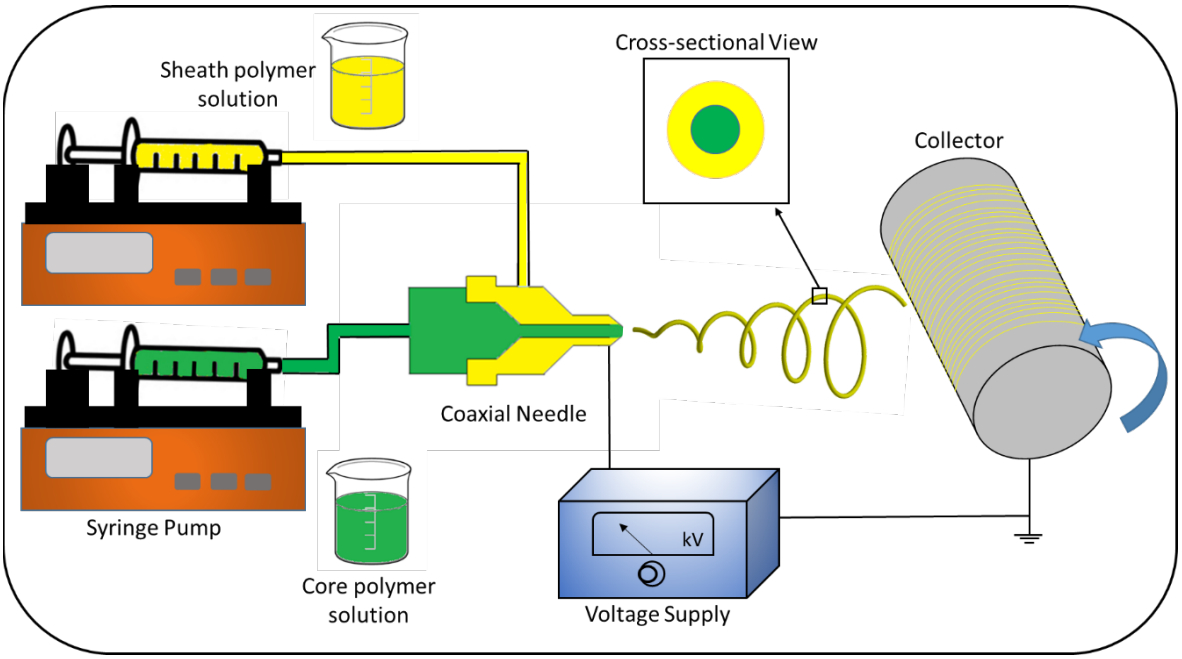

Figure 1-6. Coaxial electrospining setup

1.3.4 Coaxial Electrospinning

Coaxial electrospinning is a special type of electrospinning in which one polymer is enclosed by another resulting in a core-shell format of the fiber. Figure 1-6 shows a graphical representation of the coaxial electrospinning setup for two polymers. One of

the critical parameters to consider for optimal electrospun fibers is the applied critical voltage at which both of the polymer solutions spin concurrently at a value lower than the critical voltage. This results in the dripping of one solution, while higher values cause separate jets for each polymer to form.

1.4 Scope of the Dissertation

Plant-sourced carbon has a valuable impact on zero carbon footprint materials for automotive, aerospace, water filtration, and other applications. A new lignin, poly-(caffeyl alcohol) (PCFA, also known as C-lignin), has recently been discovered in the seeds of the vanilla orchid (*Vanilla planifolia*). In contrast to all known lignins which comprise of polyaromatic networks, the PCFA lignin is a linear polymer derived almost totally from caffeyl alcohol monomers linked head to tail into benzodioxane chains via the ‘endwise’ radical coupling reactions that typify lignification. In Chapter 2 we investigate carbon fiber formed from this linear C-lignin and compare it to a Kraft lignin.

In Chapter 3 PCFA was blended with poly-acrylonitrile (PAN) via an electrospinning process. The effect of blending on the spinnability, miscibility, chemical crosslinking and thermal properties of precursor blend fibers was investigated by SEM, DSC, FTIR.

In Chapter 4, we examine an environment friendly approach by omitting the use of organic solvent and blending low molecular weight (PCFA) with high molecular weight poly ethylene oxide (PEO) in aqueous sodium hydroxide solution.

Natural fiber offers unique properties enabled by a porous core and solid sheath. The introduction of surface porosity has enabled improved composite performance. In

Chapter 5, we develop a fabrication process and examine this architecture in electrospun meshes. Porosity in the fibers was introduced using supercritical CO_2, a solvent free physical foaming agent. Polycaprolactone (PCL) and Poly butylene adipate-co-terephthalate (PBAT) were used because of they offer a CO_2 miscible and CO_2 immiscible choice. In Chapter 6, viscoelastic modeling of porous electrospun fibers was performed to analyses the effect of the cellular material on the mechanical properties of fibers.

1.5 Reference

[1] http://news.mit.edu/2016/national-public-private-institute-innovations-fibers-fabrics-0401

[2] https://web.stanford.edu/group/frg/active_research_themes/fabric.html

[3] http://www.nature.com/news/the-inside-story-on-wearable-electronics-1.18906

[4] Zhang, M., Wang, C., Wang, H., Jian, M., Hao, X., & Zhang, Y. (2017). Carbonized cotton fabric for high-performance wearable strain sensors. Advanced Functional Materials, 27(2), 1604795-n/a. doi:10.1002/adfm.201604795

[5] Wu, C., Kim, T. W., Guo, T., & Li, F. (2017). Wearable ultra-lightweight solar textiles based on transparent electronic fabrics. Nano Energy, 32, 367-373. doi:http://doi.org/10.1016/j.nanoen.2016.12.040

[6] Zander, N.E.; Gillan, M.; Sweetser, D. Recycled PET Nanofibers for Water Filtration Applications. Materials2016, 9, 247.

[7] Krause, A., DÃ¶rfler, S., Piwko, M., Wisser, F. M., Jaumann, T., Ahrens, E., et al. (2016). High area capacity lithium-sulfur full-cell battery with prelitiathed silicon nanowire-carbon anodes for long cycling stability. Scientific Reports, 6, 27982. Retrieved from http://dx.doi.org/10.1038/srep27982

[8] http://www.electrospintech.com/piezopowergen.html#.WCY3d_krJaQ

[9] Rattfält, L., et al., Electrical characteristics of conductive yarns and textile electrodes for medical applications. Medical and Biological Engineering Computing, 2007. 45: p. 1251-1257.

[10] Lorussi, F., et al., Wearable, Redundant Fabric-Based Sensor Arrays for Reconstruction of Body Segment Posture. IEEE Sensors Journal 2004. 4(6): p. 807- 818.

[11] http://www.smartshirt.gatech.edu/

[12] Catrysse M, Puers R, Hertleer C et al (2004) Towards the integration of textile sensors in a wireless monitoring suit. Sens Actuators A Phys 114(2–3):302–311

[13] Nar, M., Rizvi, H. R., Dixon, R. A., Chen, F., Kovalcik, A., & D'Souza, N. (2016). Superior plant based carbon fibers from electrospun poly-(caffeyl alcohol) lignin. Carbon, 103, 372-383. doi:http://dx.doi.org/10.1016/j.carbon.2016.02.053

[14] Gashti, M. P., Pakdel, E., & Alimohammadi, F. (2016). Nanotechnology-based coating techniques for smart textiles. In Active Coatings for Smart Textiles (pp. 243-268). Woodhead Publishing.

[15] M. Zhang, K. R. Atkinson, R. Baughman, Multifunctional carbon nanotube yarns by downsizing an ancient technology.Science, 306, 1358(2004)

[16] Global carbon fibre market remains on upward trend, Market report, Reinforced Plastics, May 2014.

[17] M. Minus, and S. KumarThe processing, properties, and structure of carbon fibers. Jom, 57, 52-58.(2005)

[18] M. D. Lima, S. Fang, X. Lepró, C. Lewis, R. Ovalle-Robles, J. Carretero-González, E. Castillo-Martínez, M. E. Kozlov, J. Oh, N. Rawat, C. S. Haines, M. H. Haque, V. Aare, S. Stoughton, A. A. Zakhidov and R. H. Baughman,,Biscrolling Nanotube Sheets and Functional Guests into Yarns,Science 331, 51 (2011)

[19] A. Beigbeder, P. Degee S. L. Conlan, R. J. Mutton, A. S. Clare, M. E. Pettitt, M. E. Callow , J. A. Callow P. Dubois, Biofouling, 24, 291 (2008)

[20] L. Dai, D. W. Chang, J. B. Baek, W. Lu, Carbon nanomaterials for advanced energy conversion and storage. Small 8, 1130 (2012)

[21] C. Sotowa, G. Origi, M. Takeuchi , Y. Nishimura K. Takeuchi, Y. Jang Y. Kim, T. Hayashi, Y. A.Kim, M. Endo, M. S. Dresselhaus, The Reinforcing Effect of Combined Carbon Nanotubes and Acetylene Blacks on the Positive Electrode of Lithium-Ion Batteries, ChemSusChem 1, 911 (2008)

[22] E. Evanoff, Adv. Mater. 24, 533 (2012)

[23] J. M. Lee, J. S. Park, S. H. Lee, H. Kim, S. Yoo, S. O. Kim, Selective electron- or hole-transport enhancement in bulk-heterojunction organic solar cells with N- or B-doped carbon nanotubes, .Adv. Mater. 23, 629 (2011)

[24] A. Le Goff, V. Artero, B. Jousselme, P. D. Tran, N. Guillet, R. Métayé, A. Fihri S. Palacin, M. Fontecave, .From hydrogenases to noble metal-free catalytic nanomaterials for H2 production and uptake. Science 326, 1384 (2009)

[25] G. Gao, C. D. Vecitis, Electrochemical carbon nanotube filter oxidative performance as a function of surface chemistry. Environ. Sci. Technol 45, 9726 (2011)

[26] Z. Shi , K. G. Neoh , and E. T. Kang, Antibacterial and Adsorption Characteristics of Activated Carbon Functionalized with Quaternary Ammonium Moieties, Ind. Eng. Chem. Res.,46,439 (2006)

[27] S. Kassegne, , M. Vomero, R. Gavuglio, M. Hirabayashi, E. Özyilmaz, S. Nguyen, J. Rodriguez, E. Özyilmaz, P. van Niekerk, A. Khosla, Electrical impedance, electrochemistry, mechanical stiffness, and hardness tunability in glassy carbon MEMS µECoG electrodes, Microelectronic Engineering, 133,36 (2012)

[28] K. Mui, D. K. Basa, F. W. Smith, and R. Corderman, Optical constants of a series of amorphous hydrogenated silicon-carbon alloy films: Dependence of optical response on film microstructure and evidence for homogeneous chemical ordering Phys. Rev. B 35, 8089 (1987)

[29] A. Bianco, K. Kostarelos, M. Prato, Making carbon nanotubes biocompatible and biodegradable,.Chem Commun, 47, 10182(2011)

[30] V. B. Fedorov, M. Kh. Shorosov, D. K. Khakimova, Carbon and Its Reactions with Metals, Metallurgiya, Moscow 1978.

[31] Rahaman, M. S. A., Ismail, A. F., and Mustafa, A. (2007). A review of heat treatment on polyacrylonitrile fiber. Polymer Degradation and Stability, 92(8), 1421-1432.

[32] Jason Hilla, Stephen Polaskya, Erik, Nelsonc, David Tilmanb, Hong Huod, Lindsay Ludwige, James Neumanne, Haochi Zhenga, and Diego Bontaa, Climate change and health costs of air emissions from biofuels and gasoline, PNAS February 10, 2009 vol. 106 no. 6 2077-2082.

[33] Compere, A. L., Griffith, W. L., Leitten, C. F., and Shaffer, J. T. (2001, August). Low cost carbon fiber from renewable resources. In International SAMPE Technical Conference (Vol. 33, pp. 1306-1314).

[34] Dallmeyer, I., Lin, L. T., Li, Y., Ko, F., & Kadla, J. F. (2014). Preparation and characterization of interconnected, kraft lignin-based carbon fibrous materials by electrospinning. Macromolecular Materials and Engineering, 299(5), 540-551

[35] Ragauskas, A. J., Beckham, G. T., Biddy, M. J., Chandra, R., Chen, F., Davis, M. F., Davison, B. H., Dixon, R. A., Gilna, P., Keller, M., Langan, P., Naskar, A. K.,

Saddler, J. N., Tschaplinski, T. J., Tuskan, G. A., and Wyman, C. E. (2014). Lignin valorization: improving lignin processing in the biorefinery. . Science 344, 709

[36] Kadla, J.F., Kubo, s., Gilbert, R.D., Venditti, R.A., Compere, A.L., Griffith, W.L.Lignin-based carbon fibers for composite fiber applications, Carbon 40 (2002) 2913–2920

[37] Kubo, S. and Kadla, J. F. (2005), Kraft lignin/poly(ethylene oxide) blends: Effect of lignin structure on miscibility and hydrogen bonding. J. Appl. Polym. Sci., 98: 1437–1444.

[38] Satoshi Kubo and and John F. Kadla, Poly(Ethylene Oxide)/Organosolv Lignin Blends: Relationship between Thermal Properties, Chemical Structure, and Blend Behavior, Macromolecules 2004, 37, 6904-6911

[39] Seo, D.K., Jeun, J.P., Kim, H.B., Kang, P.H. Preparation and characterization of the carbon nanofibers mat produced from electrospun PAN/lignin precursors by electron beam irradiation. Rev Adv Mater Sci 2011;28:31-34.

[40] Xu, X., Zhou, J., Jiang, L, Lubineau, G., Payne, S.A., Gutschmidt, D. Lignin-based carbon fibers: Carbon nanotube decoration and superior thermal stability. Carbon 2014;80:91-102.

[41] Chen, F., and Dixon, R.A. (2007). Lignin modification improves fermentable sugar yields for biofuel production. Nature Biotechnology 25, 759-761.

[42] Reddy, M.S.S., Chen, F., Shadle, G.L., Jackson, L., Aljoe, H., and Dixon, R.A. (2005). Targeted down-regulation of cytochrome P450 enzymes for forage quality improvement in alfalfa (Medicago sativa L.). Proc Natl Acad Sci USA 102, 16573-16578

[43] Vanholme, R., Morreel, K., Darrah, C., Oyarce, P., Grabber, J.H., Ralph, J., and Boerjan, W. (2012). Metabolic engineering of novel lignin in biomass crops. New Phytologist 196, 978-1000.

[44] Tsuji, Y., Vanholme, R., Tobimatsu, Y., Ishikawa, Y., Foster, C. E., Kamimura, N., et al. (2015). Introduction of chemically labile substructures into arabidopsis lignin through the use of LigD, the Cα-dehydrogenase from sphingobium sp. strain SYK-6. Plant Biotechnology Journal, 13(6), 821-832. doi:10.1111/pbi.12316

[45] Chen, F., Tobimatsu, Y., Havkin-Frenkel, D., Dixon, R.A., and Ralph, J. (2012). A polymer of caffeyl alcohol in plant seeds Proceedings of the National Academy of Sciences USA 109, 1772-1777.

[46] Chen, F., Tobimatsu, Y., Jackson, L., Ralph, J., and Dixon, R.A. (2013). Novel seed coat lignins in the Cactaceae: structure, distribution and implications for the evolution of lignin diversity. . Plant Journal 73, 201-211.

[47] Tobimatsu, Y., Chen, F., Nakashima, J., Jackson, L.A., Dixon, R.A., and Ralph, J. (2013). Coexistence but independent biosynthesis of catechyl and guaiacyl/syringyl lignins in plant seeds. Plant Cell 25, 2587-2600.

[48] Gupta, A. K., Paliwal, D. K., & Bajaj, P. (1998). Melting behavior of acrylonitrile polymers. Journal of Applied Polymer Science, 70(13), 2703-2709. doi:10.1002/(SICI)1097-4628(19981226)70:13<2703::AID-APP15>3.0.CO;2-2

[49] Mahato, R.I. Biomaterials for delivery and targeting of proteins and nucleic acids, CRC Press (2005).

[50] B. G. Ayre, K. Stevens, K. D. Chapman, C. L. Webber III, K. L. Dagnon, N. A. D'Souza, Viscoelastic Properties of Kenaf Bast Fiber in Relation to Morphology of Development , Textile Research Journal, 79, 973–980, 2009.

[51] D. Ramesh, B. G. Ayre, N. D'Souza, C. L. Webber III, Dynamic mechanical analysis, surface chemistry and morphology of alkali and enzymatic retted kenaf fibers, Textile Research Journal, 85, 2059-2070 (2015)

[52] N. A. D'Souza, M. S. Allen, K. Stevens, B. Ayre, D. K. Visi, S. Vidhate, I. Ghamarian, and C. L. Webber III, (2011) Biocomposites: The Natural Fiber Contribution from Bast and Woody Plants . In: C.L. Webber III and A. Liu (Eds.). Plant Fibers as Renewable Feedstocks for Biofuel and Bio-based Products. CCG International Inc (2011).

[53] B. G. Ayre, K. Stevens, K. D. Chapman, C. L. Webber III, K. L. Dagnon, N. A. D'Souza, Viscoelastic Properties of Kenaf Bast Fiber in Relation to Morphology of Development , Textile Research Journal, 79, 973–980, 2009.

[54] D. Ramesh, B. G. Ayre, N. D'Souza, C. L. Webber III, Dynamic mechanical analysis, surface chemistry and morphology of alkali and enzymatic retted kenaf fibers, Textile Research Journal, 85, 2059-2070 (2015)

[55] N. A. D'Souza, M. S. Allen, K. Stevens, B. Ayre, D. K. Visi, S. Vidhate, I. Ghamarian, and C. L. Webber III, (2011) Biocomposites: The Natural Fiber Contribution from Bast and Woody Plants . In: C.L. Webber III and A. Liu (Eds.). Plant Fibers as Renewable Feedstocks for Biofuel and Bio-based Products. CCG International Inc (2011)

[56] Reneker, D. H., & Yarin, A. L. (2008). Electrospinning jets and polymer nanofibers. Polymer, 49(10), 2387-2425. doi:http://dx.doi.org/10.1016/j.polymer.2008.02.002

[57] McKee, M. G., Wilkes, G. L., Colby, R. H., & Long, T. E. (2004). Correlations of solution rheology with electrospun fiber formation of linear and branched polyesters. Macromolecules, 37(5), 1760-1767. doi:10.1021/ma035689h.

[58] Fundamentals of Fiber Science, By Xiangwu Zhang

[59] Nezarati, R. M., Eifert, M. B., & Cosgriff-Hernandez, E. (2013). Effects of humidity and solution viscosity on electrospun fiber morphology. Tissue Engineering.Part C, Methods, 19(10), 810-819. doi:10.1089/ten.tec.2012.0671

[60] Wang, Y., Li, Y., Sun, G., Zhang, G., Liu, H., Du, J., et al. (2007). Fabrication of Au/PVP nanofiber composites by electrospinning. Journal of Applied Polymer Science, 105(6), 3618-3622. doi:10.1002/app.25003.

[61] Liu, R., Ye, H., Xiong, X., & Liu, H. (2010). Fabrication of TiO2/ZnO composite nanofibers by electrospinning and their photocatalytic property. Materials Chemistry and Physics, 121(3), 432-439. doi:http://dx.doi.org/10.1016/j.matchemphys.2010.02.002

[62] Qin, Xiaohong, and Dequn Wu. 2012. Effect of different solvents on poly(caprolactone) (PCL) electrospun nonwoven membranes. Journal of Thermal Analysis and Calorimetry 107 (3) (03/01): 1007-13, http://dx.doi.org/10.1007/s10973-011-1640-4.

[63] Deitzel, J. M., J. Kleinmeyer, D. Harris, and N. C. Beck Tan. 2001. The effect of processing variables on the morphology of electrospun nanofibers and textiles. Polymer 42 (1) (1): 261-72.

[64] Peresin, Maria S., Youssef Habibi, Arja-Helena Vesterinen, Orlando J. Rojas, Joel J. Pawlak, and Jukka V. SeppalÌˆlalÌˆ. 2010. Effect of moisture on electrospun nanofiber composites of poly(vinyl alcohol) and cellulose nanocrystals. Biomacromolecules 11 (9) (09/13; 2014/10): 2471-7, http://dx.doi.org/10.1021/bm1006689.

CHAPTER 2

INTRINSIC CONDUCTIVITY: LOW CARBON FOOTPRINT BIOBASED CARBON[1]

2.1 Introduction

Carbon fibers are a high volume, high performance product in applications ranging from carbon fiber reinforced epoxy for aerospace [1] and marine applications [2], electromagnetic interference shielding [3], biomedical applications for regenerative medicine and cancer treatment [4], energy storage devices [5] and water filtration [6]. A major application of carbon fibers is in composites where enhanced strength to weight ratio is obtained over fiberglass reinforced composites. Currently carbon fiber is manufactured predominantly from polyacrylonitrile (PAN) with a small fraction originating in pitch. PAN-based carbon fiber uses the acrylonitrile monomer which has a high cost. Pitch raw materials are cheaper but the processing involves cleanup leading to high final cost. Pitch from petroleum is preferred over coal pitch from the perspective of raw material clean up, but vacuum cleaning is required to remove volatile matter [7]. To form carbon fibers, wetting of PAN prior to carbonization is employed. Typical carbon yields for PAN-based and pitch-based carbon fibers are about 50-60% and 70-80% respectively [8]. A pre-oxidation step to carbonization has been shown to result in higher carbon yield [9]. Additional graphitization with argon has increased the carbon yield to 80% for PAN fibers [10]. Synthetic polymers such as polyacetylene [11], polyethylene [12], and polybenzoxazole [13] have also been investigated as a potential route for obtaining carbon but the performance of the final products has been found to be inferior

[1] This entire chapter is reproduced from Nar, M., Rizvi, H. R., Dixon, R. A., Chen, F., Kovalcik, A., & D'Souza, N. (2016). Superior plant based carbon fibers from electrospun poly-(caffeyl alcohol) lignin. *Carbon, 103*, 372-383. doi:http://dx.doi.org/10.1016/j.carbon.2016.02.053

to PAN. The high temperature of the PAN process contributes to a larger energy footprint and consequent impact on materials formed from them for carbon footprint calculations. Because of such concerns, the development of a source of carbon fiber based on plant materials is being strongly promoted [14].Compared to PAN and pitch precursors, lignin is cost effective and has an aromatic structure that is carbon rich for higher carbon yield [15]. There is therefore considerable interest in determining whether lignin can be developed as a cost-effective feedstock for carbon-based applications, potentially as a byproduct of the processing of lignocellulosic liquid biofuels [16].

Among plant resources, lignocellulose is a dominant constituent of plant dry matter, consisting of a complex of cellulose and hemicellulose embedded in lignin. Lignin is the second most abundant natural polymer on earth, produced by oxidative polymerization of p-hydroxycinnamyl alcohols (monolignols). Lignins are primarily found in plant secondary cell walls, and are particularly abundant in vascular tissues. The presence of this lignin reduces forage digestibility and hinders agro-industrial processes for generating pulp or biofuels from lignocellulosic plant biomass. There has therefore been considerable attention given to reducing lignin content in plant feedstocks and developing value added products for the lignin that is grown [17-20].

Lignin consists of a random polyaromatic network of linked phenylpropanoid units along with various functional groups [21]. They are broadly divided into three categories: softwood (gymnosperm), hardwood (angiosperm) and grass or annual plant (graminaceous) lignin [22]. These different classes of lignin are mainly derived from the copolymerization of three p-hydroxycinnamyl alcohol monomers known as monolignols. The primary monolignols (monomers) are p-coumaryl, conferyl and sinapyl alcohols

[23]. From Figure 2-1 it can be seen these monolignols differ from each other due to the number of methoxyl group attached to the 3 and 5 position of the aromatic ring.

The polymerization of these monomers give rise to subunits which couple in different percentages to form different classes of lignin. P-coumaryl alcohol gives rise to a p-hydroxyphenyl (H) subunit, coniferyl alcohols gives a guaiacyl (G) subunit and sinapyl alcohol gives a syringyl (S) subunit (Figure 2-1).

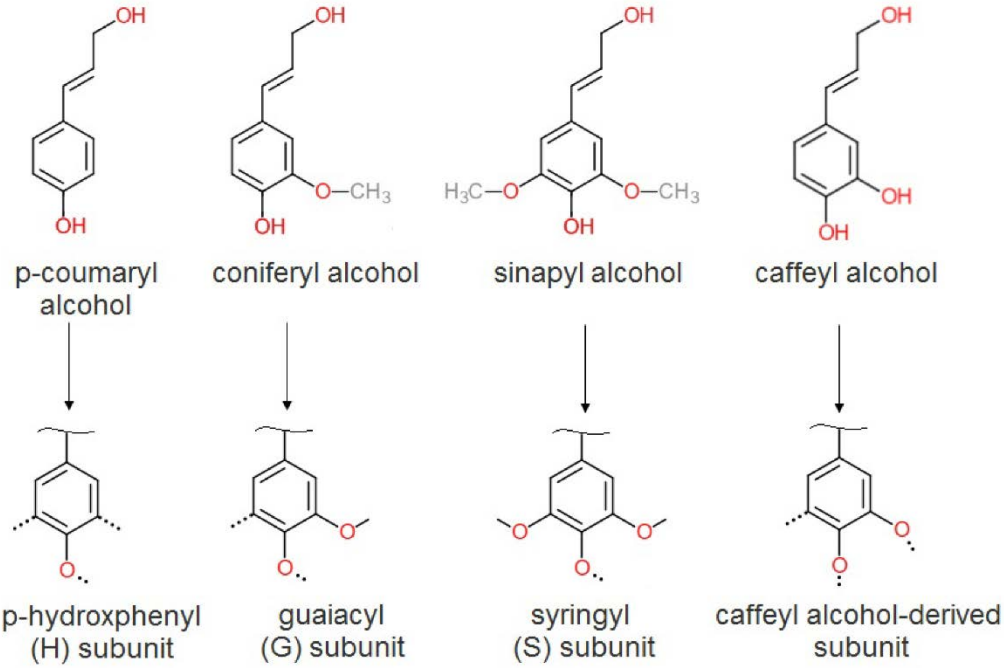

Figure 2-1. Lignin monomers and their derive subunits.

Softwood lignins are mainly derived from the guaiacyl (G) subunit, having low levels of the p-hydroxyphenyl (H) and syringyl (S) subunit. Hardwood lignin consists mainly of both (G) and (S) with low level of (H) subunit. On the contrary grass lignin consists of a high quantity of (H) subunit as compare to (G) and (S) subunits [24]. The random combination of these subunits gives rise to high variability in chain sequences and conformation. However there are characteristic linkages which are predominantly

found in different percentages due to the combination of these subunits which distinguish each of them.

Figure 2-2 shows the chemical structure off these linkages. There are typically four types of functional groups attached to these linkages including phenolic hydroxyl, aliphatic hydroxyl, methoxyl and carbonyl groups. Table 2-1 lists the percentage of these linkage in softwood and hardwood lignin [25]. The topology of grass lignin has not been extensively clarified [26].

Table 2-1. Percentage of linkages type is lignin.

Linkage Type	Dimer Structure	% of linkages in Softwood	% of linkages in Hardwood
β-O-4	Phenylpropane β−aryl ether	45-50	60
5-5	Biphenyl and Dibenzodioxocin	18-25	20-25
β -5	Phenylcoumaran	9-12	6
β-1	1,2-Diaryl propane	7-10	7
α-O-4	Phenylpropane α−aryl ether	6-8	7
4-O-5	Diaryl ether	4-8	7
β - β	β – β- linked structures	3	3

Recently Chen et al. [27-29] discovered that seed coats of a variety of plant species contain a previously unsuspected class of lignin-like molecule made entirely from caffeyl alcohol units (essentially G units lacking the methyl group on the 3-oxygen) which are not found in softwood, hardwood or grass lignin. This is termed as C-lignin or PCFA. Figure 2-1 shows the chemical structure of caffeyl alcohol monomer and its C subunit. Analysis of the lignin monomer composition of seed coat of V. planifolia and Brazilian cactus Melocactus salvadorensis by thioaciolysis indicates that the lignin is a

linear polymer derived almost totally from caffeyl alcohol monomers linked head to tail into benzodioxane chains via the ‘endwise’ radical coupling reactions that typify lignification. Interestingly the β-aryl ether units, which are the dominant linkage units found in both hardwood and softwood lignins derived from coniferyl and sinapyl alcohols, were absent, whereas benzodioxanes were the dominant lignin units accounting for over 98% of the identifiable dimeric units in the polymer. Figure 2-2 shows the resulting repeated benzodioxanes unit.

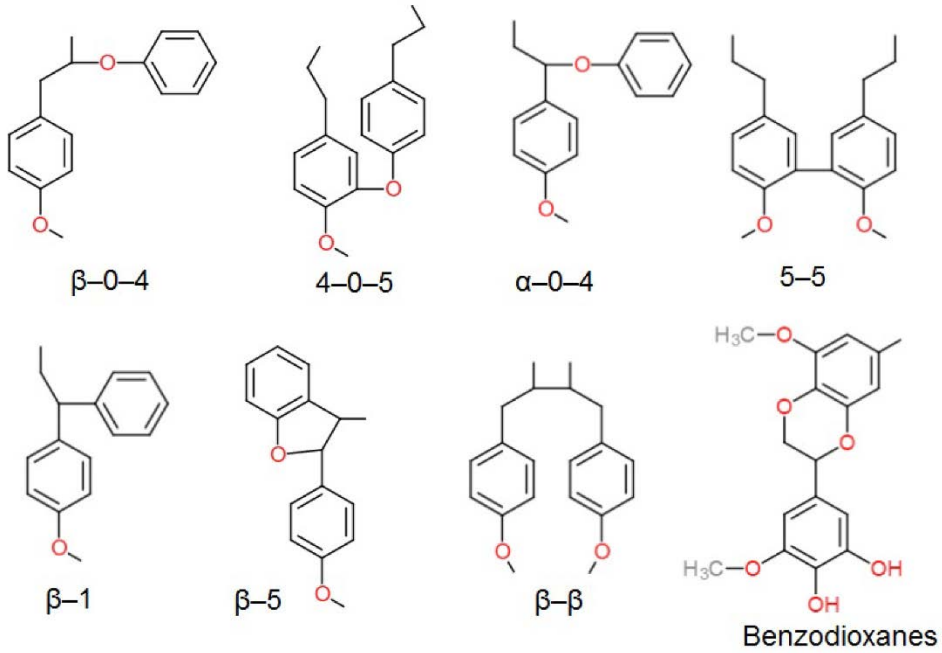

Figure 2-2. Common linkages found in lignin structure.

To isolate lignin from the biomass there are number of industrial and experimental methods that are being employed. The main purpose of theses pulping method is to minimize the degradation of the carbohydrate component. These chemical pulping processes can be classified into alkaline, acidic or neutral. Some of these main process include Kraft, soda, acid sulfite and organosolv pulping each of which results in different structural modification and degradation.

Kraft lignin, extracted from hardwoods, has been extensively studied as a feedstock for bioresourced synthetic products. It is a high volume waste obtained as a by-product from the pulp and paper industry [30]. To facilitate the melting of the lignin, organic solvent based extraction, chemical treatment or melt blending are employed [31]. The value of lignin as a source for carbon fibers obtained from melt and dry spinning of hardwood Kraft lignin (HKL), softwood Kraft lignin (SKL) and alkali softwood Kraft lignin was first shown by Otani et al. [32]. Sudo used hydrogenation with NaOH using Raney-Ni [33], followed by steam explosion to isolate the lignin and then modification to lower its softening point, thereby facilitating melt spinning of the fibers. However, this method was expensive and a cheaper alternative was attempted using creosote for phenolysis [34]. Although phenolysis improved the yield to 40 %, tensile properties were low when compared to hydrogenation. Acetic acid pulping from hardwood gave fusible lignin that could be melt-spun [35]. Lignin from softwood resulted in a high fraction of high molecular weight infusible lignin that must be separated from the fusible fraction in order to facilitate melt spinning [36].

Chemo-enzymatic treatment (sulfonication) [37] has been shown to transform water insoluble Kraft and organosolv lignin to water soluble material, and facilitates grafting of acrylic compounds onto the lignin backbone. Esterification of lignin from sources such as palm trunk, poplar, maize, barley, wheat, and rye with succinate anhydride [38] showed relatively low substitution of succinate, but gave thermal stability ranging from 100 to 600 °C, with the highest for lignin from rye.

Conversion of lignin to carbon fiber has followed many routes. One approach requires modification of the fiber surface during fiber formation through use of a low

boiling point solvent such as ethanol in a coaxial die [12]. Switching from Kraft to Allcell lignin has also been employed. Lallave et al. [39] electrospun Alcell lignin (an organosolv lignin that is highly hydrophobic and, unlike Kraft lignin, contains no measurable sulfur and very low ash) into fibers without polymer as a binder, using ethanol in a coaxial needle as an outer sheath to enable fiber formation or using a tri-axial needle with glycerin as a core material and ethanol as an outer sheath.

The second approach uses catalysts such as platinum and a third uses secondary polymers blended in with lignin. Blending polymers with lignin enables fiber integrity through improved melt strength. Poly(ethylene oxide) (PEO) has been widely studied for imparting spinnability into lignin for fiber formation. Incorporation of 3% and 5% PEO in hardwood Kraft lignin (HKL) improved spinning capability and tensile properties, respectively [40] and [41]. With an Alcell/PEO blend, strong hydrogen bonding resulted in miscible blends aiding spinning of fibers, although the addition of PEO did not improve the mechanical properties of the fiber [42]. To overcome brittleness, lignin was blended with polyethylene terephthalate (PET) and polypropylene (PP). Blends of PET and PP with HKL gave fiber diameter ranges from 30 to 76 µm, and blends with 25% polymers yielded 60% carbon after carbonation [43]. A caveat was that this route did not improve the physical properties of the fibers. Similarly, polyethylene glycol (PEG)-lignin was used for single needle melt spinning by Lin et al. [44] to obtain 23 µm diameter fibers at 170 °C. To electrospin lignin, Ago et al. [45] reported adding 25 % of poly(vinyl alcohol) (PVA) to lignin resulting in bead-free uniform diameter fibers. It was also presented that the spinning performance of lignin solution can be improved by its mixing with polyacrylonitrile (PAN) [46,47].

Considerable work remains to be done to obtain carbon from plant sources. In this paper we examine the carbon fiber formed from a new lignin, recently discovered [27- 29]. We predict that such a linear structure would enhance the ability to generate carbon fibers by electrospinning. We here test this hypothesis, comparing samples of PCFA from seed coats of Vanilla planifolia with Kraft lignin.

2.2 Experimental

2.2.1 Materials

Sulphuric acid, 98 %, p.a. and tetrahydrofuran, 99.9% were purchased from Carl Roth (Austria). Hydrochloric acid, 37 %, was supplied by Sigma Aldrich (Germany).

PCFA (C-lignin) was obtained from seed coats of Vanilla planifolia. Vanilla seeds were ground to a powder using a freezer/mill 6870, then extracted with chloroform and methanol three times consecutively. To isolate PCFA, the extracted seeds were mixed with 1% NaOH in a liquid to solid ratio of 10. The mixture was then heated to 120 °C, and the temperature maintained at 120 °C for 1 h in an autoclave. After cooling, the black liquid was separated from the residue by filtration, and PCFA was precipitated from the liquid phase by adjusting the pH to 3.0 with concentrated HCl. The precipitated PCFA was separated by centrifugation, washed with water and freeze dried.

Black liquor (with pH 11.0, total solids 88.9 %, Klason lignin 25.1 %, and ash 63.8 %) was obtained from Zellstoff Pöls AG, Austria, as a by-product during sulphate pulping of 70% spruce, 25% pine and 5% larch. Kraft lignin was isolated from the black liquor by precipitation with 37% HCl. After lowering the pH to 2.0, the precipitated sample was filtered with a Buchner funnel and washed with distilled water twice, to

remove unreacted compounds. The filtered sample was purified for 7 days by dialysis against Milli-Q water and subsequently freeze dried.

2.2.2 Analyses of Lignin Samples

The purity of Kraft and PCFA lignin was specified by the determination of Klason lignin (acid insoluble lignin), acid soluble lignin and ash according Tappi Standard procedures (T 13 m-54, T 222 om-02, and T 15 os-58).

The composition of non-acetylated lignin samples was determined by C, H, N, S elemental analysis by a Vario El III Universal-Elemental analyser. Results are presented as average values of two measurements.

The molecular weight averages of lignin samples were determined by size exclusion chromatography (SEC-3010, WGE-DR. Bures instrument equipped with ultraviolet and refractive index detectors). The pure GPC-ORG columns were calibrated using a series of polystyrene standards (Polymer Standard Service). The acetylated lignin samples [48] were dissolved in tetrahydrofuran at a concentration of 4 $mg.mL^{-1}$ and were analysed at room temperature. Tetrahydrofuran was used as eluent at a flow rate of 1.0 $mL.min^{-1}$ and the injection volume was 100 µL.

2.2.3 Electrospinning

A 50 % solution of PCFA was prepared in 1, 4 dioxane (boiling point of 101 °C). The powder was mixed at 50 °C for 4 h, and then transferred to the syringe for electrospinning at room temperature. The same process was repeated for Kraft lignin. A 5 ml syringe (National Scientific, Model #57510-5) with an 18 gauge (1.27 mm) 1”

long stainless steel blunt needle with a Luer polypropylene hub was used. The syringe with needle was placed on a Razel syringe pump (Model #R99-FM, Razel Scientific Instruments, St. Albans, VT).

The syringe pump flow rate was adjusted to 2.65 $ml.h^{-1}$, to have a continuous flow of solution through the tip of the needle i.e. any bead of solution wiped from the tip is immediately replace by another. The voltage was increase slowly to observe the drops attracting to the collector until a uniform Taylor's cone was observed and fixed at 20 kV. Distance between the needle and the collector was initial set 10 cm, which gives wagging stream, this was overcome by increasing the distance to 20 cm for a uniform and aligned stream from the tip of needle. To form fibers, the solution was pumped from the syringe following which the needle was charged to the prescribed voltage using a high voltage power supply (Model #ES30P-5W/DAM, Gamma High Voltage Research Inc., Ormond Beach, FL). The collector plate was set at the prescribed distance from the needle, covered with non-stick aluminium foil, and grounded. As the syringe pump and the high voltage power supply were switched on, the lignin solution came out of the needle forming a Taylor cone that was attracted by the electrostatic force towards the grounded collector plate.

2.2.4 Environmental Scanning Electron Microscopy (ESEM)

A FEI Quanta Environmental scanning electron microscope (ESEM; FEI Company, Oregon, USA) was used to image the burnt PCFA and Kraft lignin fibers at an accelerating voltage of 12.5 kV at 10 mm working distance. The samples were

sputter coated with gold-palladium to make them conductive and make imaging possible.

2.2.5 Carbonization

The conditions for thermal stabilization of PCFA and Kraft fibers selected based on our experimental survey and literature were the following [49]: heating from room temperature to 300 °C at a heating rate of 1 °C.min^{-1}, for 60 min in an air forced laboratory oven by cascade TEK . The stabilized fibers were then carbonized in Carbolite HZS 12/600 Horizontal Tube Furnace with an alumina tube having an internal diameter of 3-5/8” and outer diameter of 4”. The heating rate during carbonization step was 5 °C.min^{-1}. Fibers were held at 900 °C for 45 min under a flow of nitrogen of 0.5 standard cubic feet per hour (SCFH).

2.2.6 Raman Spectroscopy

A 532 nm intensity laser was used at 25 % power with aperture of 10 µm slit and objective lens with 10X zoom; this gave a spot size of 2.1 µm. The scan was done from 750 to 2000 cm^{-1}. The exposure time was 15 sec and background and sample exposure was performed five times. Background was collected before every sample. This background was subtracted from the Raman spectroscopy results and a baseline correction was performed.

2.2.7 Nanoindentation

Mechanical properties of Kraft and PCFA was measured along the axial and transverse direction of the electrospun fiber using MTS nanoindenter XP. Samples for the nanoindentation test were prepared by embedding carbonized fibers in an epoxy resin (EPO-FIX Embedding Resin Kit by Electron Microscopy Sciences). CSM (Continuous Stiffness Measurement) method for standard hardness and modulus with a diamond Berkovich tip was used for indentation [50]. In order to eliminate the effect of environmental noise, a combination of a minus k vibration isolation table and a thermal vibration isolation cabinet was used. Prior to the test, the equipment was tested for calibration on a fused silica reference sample. Eight indents each, in axial and transverse direction on randomly selected Kraft and PCFA carbon fibers, were made. Loading and depth curve obtained from nanoindentation were investigated as defined by Oliver and Parr [51] and [52]. Reduce Modulus depending upon the slope of the unloading curve $S = \frac{dP}{dh}$ (stiffness), contact area $A_c$which is a function of indentation depth and geometry of the indenter was calculated using the following equation.

$$E_r = \frac{\sqrt{\pi}}{2\beta}\frac{S}{\sqrt{A_c}} \dots\dots\dots\dots (1)$$

where β is the geometry constant, for Berkovich tip β=1.034. Elastic modulus of the fiber E_f is given as a function of Reduce Modulus and mechanical properties of the indenter, according to the following relation.

$$\frac{1}{E_r} = \frac{1-\vartheta_f^2}{E_f} + \frac{1-\vartheta_i^2}{E_i} \dots\dots\dots\dots (2)$$

where v_f is the Poisson ratio of the fiber (assumed to be 0.3 for both Kraft lignin and PCFA), E_i is the elastic modulus of the diamond indenter and v_i is the Poisson ratio of the indenter having values of 1141 GPa and 0. 07 respectively.

2.2.8 Zeta Potential

Samples for measurement of Zeta potential were prepared using the cryomilling technique. The PCFA and Kraft lignin were milled using a freezer mill as describe above. The milling was carried for 15 min to obtain fine powder. A Delta NanoC particle analyzer from Beckman Coulter was used to determine Zeta potential. The dispersions of the PCFA powder and Kraft lignin were made in deionized water at room temperature with sonication for 1 h.

2.2.9 X-Ray Photoelectron Spectroscopy (XPS)

The chemical structure of Kraft and PCFA carbon fiber was analysis by X-ray photoelectron spectroscopy (XPS) using a monochromatic 1486.6 eV Al Ka radiation with a PHI 5000 VersaProbe (Physical Electronics, Chanhassen, MN). Initially the low resolution survey was performed to identify the elements present on the surface. Then high resolution C1s regions were analysis to get the binding characteristics of the fiber surface. Shirley background and Gaussian–Lorentzian functions were used for peak fitting.

2.2.10 Transmission Electron Microscopy (TEM)

TEM samples were prepared using dual beam FIB-scanning electron microscope (FEI Nova 200 NanoLab) system with a Ga+ ion source. Firstly, a layer of platinum was

deposited on the surface for protection, then coarse and medium milling was performed until the sample thickness reaches around 1 µm, Next, the Omni probe was used to lift the sample and attached to the TEM half grid for fine thinning of the sample. TEM imaging was performed using the Tecnai G2 F20 field-emission Scanning Transmission Electron Microscope (S/TEM) operating at 200 kV.

2.2.11 X-Ray Diffraction (XRD)

To measure the crystallite size, interplanar spacing and degree of graphitization of carbon fiber from Kraft and PCFA X-ray diffraction was performed using a Rigaku model D/Max–Ultima III (Rigaku Tokyo). X-rays were generated at 44 mA current and 40 kV voltage with Cu Kα wavelength (λ) of 1.542 Å. Diffractograms of PCFA and Kraft Carbon fiber were recorded at room temperature in an angular 2θ range of 10 to 50 degrees with a step size of 0.05 and a scanning rate of 2 degrees/min.

2.2.12 Thermogravimetric Analysis (TGA)

TGA experiments were conducted in an inert environment of argon having a flow rate of 60 ml/min. Samples were heated from room temperature to 800 °C with a heating rate of 10 °C/min to observe thermal stability of each fiber. Experiments were carried out on STA 449 F3 Jupiter from Netzsch.

2.3 Results and Discussion

2.3.1 Composition of Lignins

The amounts of carbon, hydrogen, nitrogen, sulfur, Klason lignin, acid soluble lignin and ash for PCFA and Kraft lignin are listed in Table 2-2. The PCFA preparation shows about 13.8 % higher total lignin content and about 4.8 % higher ash content than Kraft lignin. The higher total lignin content means lower content of other non-lignin admixtures such as carbohydrates and extractives present in the PCFA preparation. Lignin derived from one-year-old herbaceous tissues typically contain higher ash content than lignin derived from mature wood due to the high concentration of minerals (silicon, aluminum, calcium, magnesium, potassium and sodium) [53]. The elemental analysis showed 52.9 % of carbon, 6.4 % of hydrogen, 13.5 % of nitrogen and 8.7 % of sulfur present in PCFA. In comparison with Kraft lignin, the PCFA preparation contains a lower percentage of carbon, hydrogen and oxygen (oxygen content = 100 – carbon – hydrogen – nitrogen – sulfur - ash) but a higher percentage of nitrogen, sulfur and ash. The higher ash content indicates a higher presence of an inorganic fraction in the seed-derived PCFA preparation than is typical for lignin derived from stem tissues [54]. The detected differences in the elemental compositions of the two lignin preparations are associated with their origins and the applied isolation methods [55].

Table 2-2. Values of lignin content based on solid residue and elemental analysis.

Sample	Klason lignin (%)	Acid soluble lignin (%)	aTotal lignin (%)	Ash content (%)	C (%)	H (%)	N (%)	S (%)
Kraft Lignin	71.5	5.3	76.8	1.7	62.4	7.9	2.9	1.9
PCFA	76.8	13.8	90.6	6.5	52.9	6.4	13.5	8.7

a Total lignin was calculated as Klason + acid soluble lignin

The molecular weight distributions of acetylated PCFA and Kraft lignin are shown in Figure 2-3 and tabulated in Table 2-3. PCFA lignin exhibited 1.76-fold lower weight-average molecular weight with a narrower weight distribution ($\overline{Mw}$ = 1700 and PDI =1.6) than Kraft lignin with ($\overline{Mw}$ = 4700 and PDI = 2.6). The narrower molecular weight distribution indicates the higher molecular uniformity of PCFA lignin, which favors its use for fiber applications.

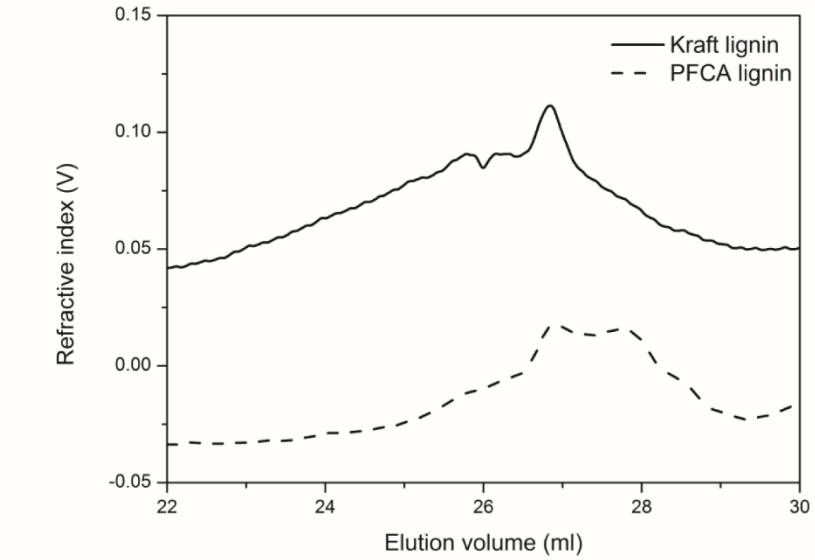

Figure 2-3. SEC chromatogram of Kraft and PCFA lignins.

Table 2-3. SEC characterization of lignins.

Sample	$\overline{M_n}$	$\overline{M_w}$	Polydispersity index (PDI)
Kraft lignin	1830	4740	2.6
PCFA lignin	1040	1700	1.6

2.3.2 Electrospun Fibers

Solutions of both PCFA and Kraft lignin are electrospinnable. Continuous electrospun fibers were obtained under conditions of 20 kV and 2.65 cc/h solution flow rate with a distance of 20 cm to the stationary collector plate. The conditions were selected as the common conditions that enabled both lignins to form fibers after examining voltages from 5 to 35 kV, distances of 20 to 40 cm (in increments of 5) for both lignins at the same flow rate. The preliminary ranges were similar to those we employed in a polysaccharide fiber electrospinning investigation [56]. The ESEM images suggest that the fibers obtained are highly uniform with no beads. Obtaining bead-free fibers depends on the conductivity of the solution which elongates the Taylor cone formed at the tip of the needle to give electrospun fibers. During electrospinning of both PCFA and Kraft lignin a minimum voltage of 20kV was essential to overcome the surface tension of the Taylor cone. A 50 % solution in 1, 4 dioxane at 50 °C provided enough entanglement in PCFA to spin it into fibers.

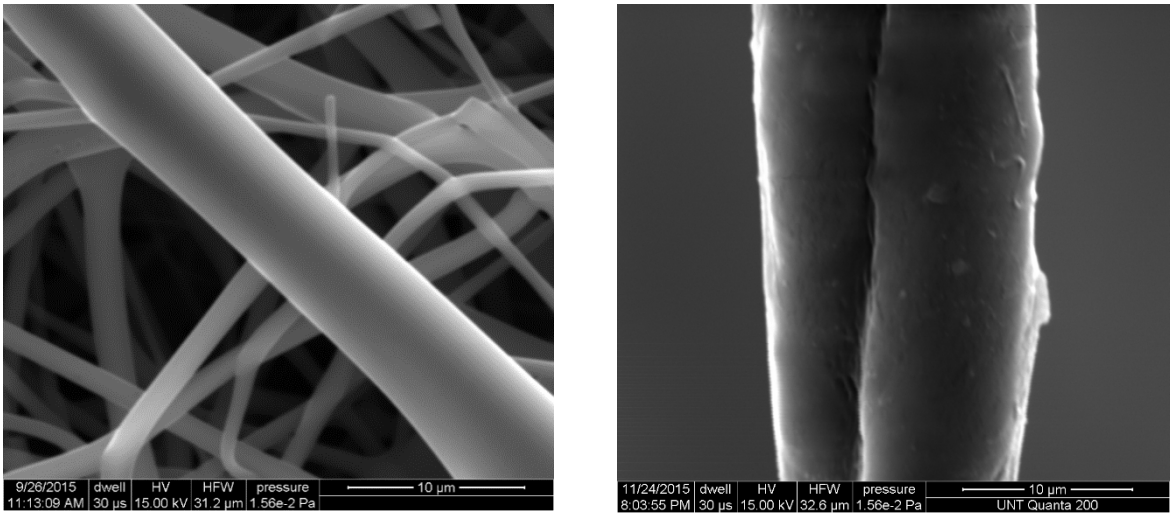

A B

Figure 2-4. ESEM image of electrospun carbon fibers. (A) Kraft, (B) PCFA lignin.

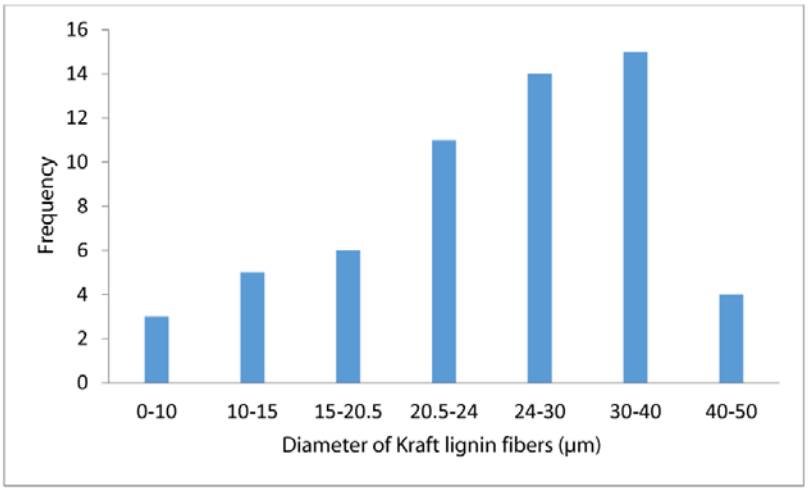

A

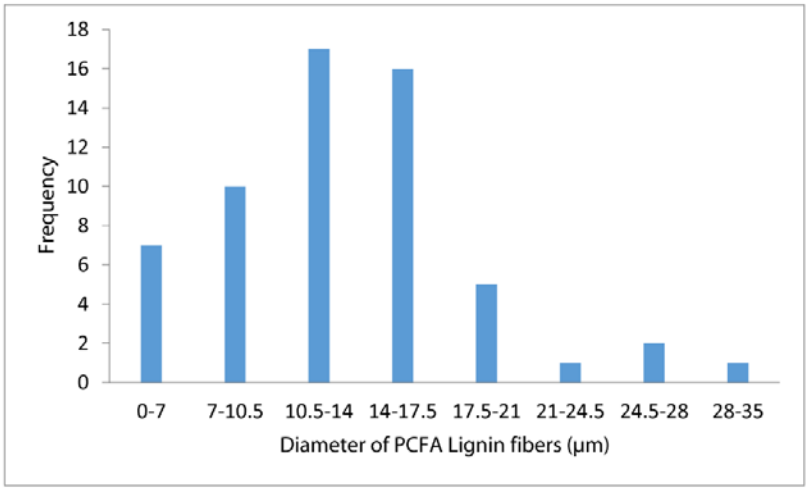

B

Figure 2-5. Histogram of the diameters of electrospun carbon fibers. (A), Kraft, (B) PCFA lignin.

The ESEM images (Figure 2-4) were analyzed using ImageJ® software. The images were corrected for the scale from pixels of the original tiff image to the known distance on the image to calibrate for scale. A total of 58 measurements of diameters were made and the histogram was plotted for the most frequent occurrence of the diameter range. PCFA produced fine uniform fibers and processed unceasingly compared to Kraft lignin which could only electrospin for a short period (approximately 50.8 mm length compared to continuous spinning for PCFA) prior to fracture (Figure 2-5). The diameters of the electrospun fibers from PCFA and Kraft lignin were in the range of 10.5 to 14 µm and 30 to 40 µm, respectively. The viscosity of the two source solutions entering the syringe pump was determined to be 5333 mPa.s for Kraft lignin and 4267 mPa.s for PCFA solutions at 12 rpm using a Brookfield viscometer in conjunction with a Spindle # 27.

2.3.3 Zeta Potential of Carbon Powders

The Zeta potential for PCFA and Kraft lignin carbon powders in deionized water are similar (Figure 2-6), around -43.35 ± 0.48 mV and -42.05 ± 2.37 mV respectively. This suggests that the stability of the carbon particles obtained from PCFA is good enough to keep them in suspension for long durations. The Zeta value indicates repulsion between the particles, thus stopping them from attracting each other and flocculating. The low mobility and conductivity values (Table 2-4) indicate that the ionic double layer is thick due to low ionic strength. The mobility of the particles in the suspension, 3.40e-004 ± 00 cm2/Vs, indicates that the attraction of particles to the

electrodes is very low. The higher ionic conductivity of Kraft lignin points to remnant impurities and complex sources of the originating liquid compared to that of PCFA.

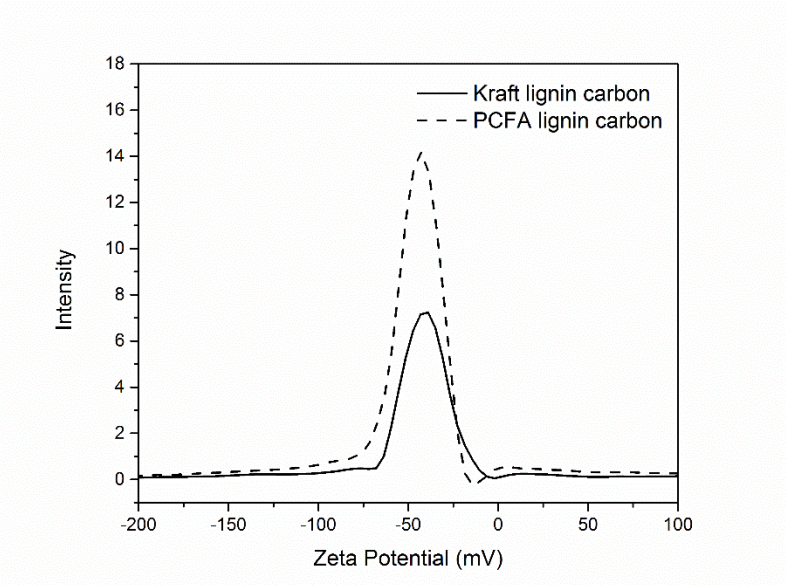

Figure 2-6. Zeta potentials of carbon from carbonized fibers of Kraft and PCFA lignin.

Table 2-4. Suspension properties of carbon from PCFA and Kraft lignin.

Sample	Zeta potential (mV)	Mobility (cm2/Vs)	Ionic conductivity (mS/cm)
PCFA powder	-43.35 ± 0.48	3.40e-004 ± 00	0.028 ± 0.00042
Kraft lignin	-42.05 ± 2.37	-3.1e-04 ± 2.0E-06	0.6457 ± 0.00051

2.3.4 Raman Spectroscopy

Raman spectroscopy was performed to compare the purity of carbon obtained from PCFA and Kraft lignin powder samples. The deconvoluted spectra of carbonized fiber of Kraft lignin and PCFA are represented in Figure. 2-6(A) and 2-6(B) respectively. The spectra shows the characteristic D band at about 1335 cm^{-1} for both lignin while the

G band lies at about 1588 cm^{-1} for Kraft lignin carbon and 1512 cm-1 for PCFA. The D and G bands give the defect-derived structures and graphite derived structure of the carbon, respectively. The D band is due to the breathing modes of sp2 atoms in the aromatic ring while the G band results from sp2 site stretching of C=C bonds. A high G/D ratio is symptomatic of higher crystalline structure. Carbon from PAN has G/D ratios ranging from 0.57-0.67, while pitch-based carbon shows higher crystal perfection with G/D ratios ranging from 2.27 to 7.6 [57]. In deconvolution of spectra one more band is present at 1190 cm^{-1} for Kraft lignin carbon (Figure 2-6A) and at 1273 cm^{-1} for PCFA carbon (Figure 2-6B), referred to as the D4 band which represents ionic impurities and/or oxygen superficial group [58]. The intensity of G and D4 band are given relative to the total integrated in Table 2.5 along with the full width at half maximum of G (WG) and D (WD) band.

Table 2-5. Parameters obtained from deconvolution of Raman spectrum of PCFA and Kraft lignin after carbonization.

Sample	I_G/I_T (%)	I/I_T (%)	WD (cm^{-1}) FWHM	WG (cm^{-1}) FWHM
Kraft Lignin Carbon	39.7	3.7 { I_{1190}/I_T (%)}	140.2	80.9
PCFA Carbon	58.8	23.4 { I_{1273}/I_T (%)}	100.5	103.9

The G-band intensity can also be used to check the purity of the samples; this is because, unlike with the D band, there is no effect of chirality on the G-band [59]. The width of the G and D bands correspond to the structural disorder. Thus the Raman spectra show that high purity carbon obtained from PCFA is comparable to that obtained from PAN [60] and [61]. The highly ordered graphitic structure in PCFA-derived carbon is correlated with higher mechanical stiffness, thermal and electrical

conductivity. Kraft lignin carbon shows a higher value of WD and lower intensity of the G band which indicates more structural disorder as compared to PCFA carbon. Thus, PCFA shows a higher carbon purity and structural order.

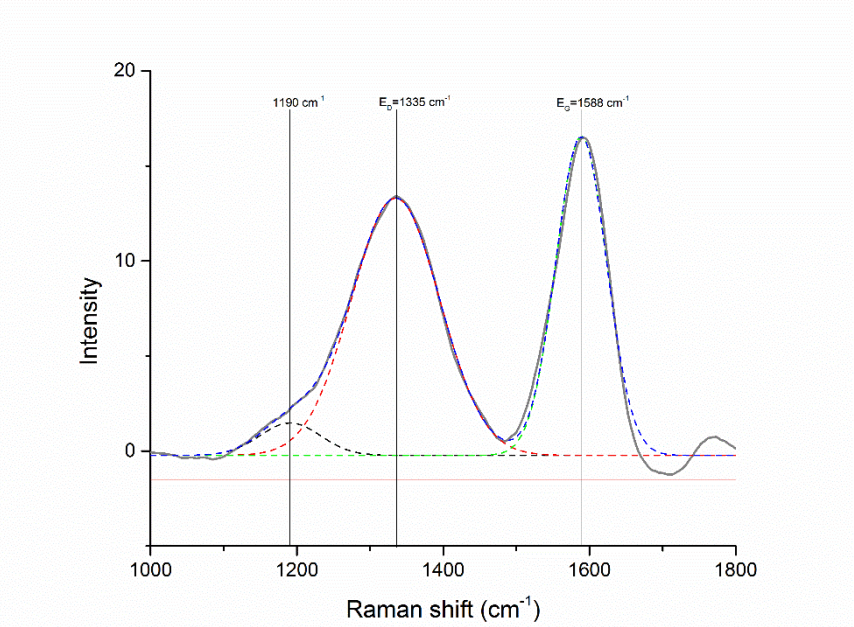

A

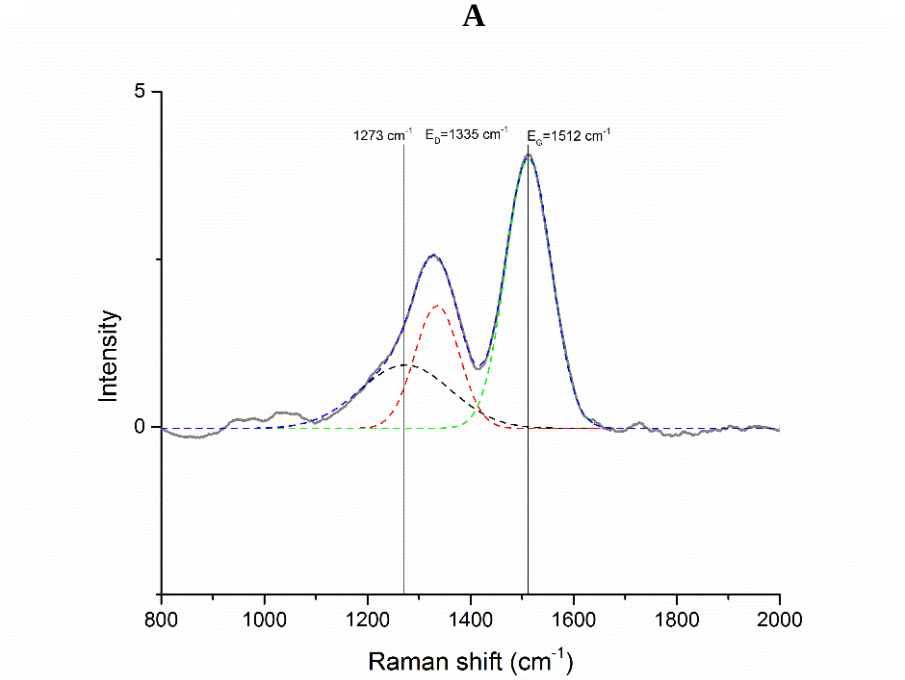

B

Figure 2-7. Raman spectroscopy deconvoluted spectra of derived carbon (A) Kraft, (B) PCFA Lignin.

2.3.5 Mechanical Properties

Methods to measure the transverse and axial modulus of fibers having diameters of only a few microns are limited. Nanoindentation is one of the techniques that is being currently explored to effectively measure the mechanical properties of small dimensioned samples, especially carbon based fillers such as nanotubes and graphene [62]. Carbon fiber samples were embedded in epoxy resin and then polished for the axial and transverse measurements. Table 2-6 compares the axial and transverse modulus of the fibers from Kraft lignin and PCFA. It can be seen that the axial and transverse moduli of PCFA fibers are greater than those of Kraft lignin fibers. The elastic modulus of carbon fiber is correlated to the bond structure and strength [63], as well as to the percentage of graphitic molecular structure. The Raman G/D ratio of 1.92 for PCFA as compared to 1.15 for Kraft lignin carbon (Table 2-5) is indicative of higher crystalline structure, consistent with the higher modulus values in both axial and transverse direction. The higher ratio of the axial to the transverse modulus of Kraft lignin fibers as compared to the PCFA fibers indicates that Kraft lignin is more aligned resulting in the lower transverse properties [64]. The higher carbon purity of PCFA is also a factor that could account for its improved mechanical properties. The properties of PCFA carbon fiber compare favorably with non biosourced carbon fibers prepared commercially. Determination of transverse properties of commercial carbon fibers by nanoindentation has been performed on M46J carbon fibers [65]; modulus was around 14 GPa. In a second study of the indentation of two PAN type commercial fibers, MK40 and MK46, the transverse moduli were measured as 15 $\pm$ 4.9GPa and 14 $\pm$ 5.7GPa respectively. In contrast, the value for a pitch based commercial fiber from Mitsubishi

(Pitch K637) was shown to be 10.7 + 3.1GPa [64]. Gind-Altmutter et al. [66] performed nanoindentation of carbonized commercial Kraft lignin microparticles at 2000 °C, reported the indentation modulus of 8.2 ± 3.04 GPa, higher than the modulus reported in Table 2-6 for Kraft lignin carbon (4.25 ± 0.82GPa) which was carbonized at 900 °C. This can be explained by the higher temperature for carbonization leading to an increase in the graphitic structure causing an increase in crystallinity and modulus. Fan et al. reported the axial and transverse modulus of a commercial fiber T700SC using nanoindentation to be 23.17 ± 1.27 GPa and 1.81 ± 0.406 GPa [67]. The axial modulus is in the same range as that for both Kraft lignin and PCFA fibers, while the lower transverse modulus indicates lower alignment in PCFA carbon compared to the commercial T700SC fiber.

Table 2-6. Nanoindentation parameters of the carbon fiber.

Sample	Modulus in Transverse Axis (GPa)	Modulus in Axial Axis (GPa)	Axial by Transverse Ratio
Kraft Lignin Carbon	4.25± 0.82	27.63 ± 5.01	6.5
PCFA	15.51 ± 0.78	34.52 ± 7.61	2.2

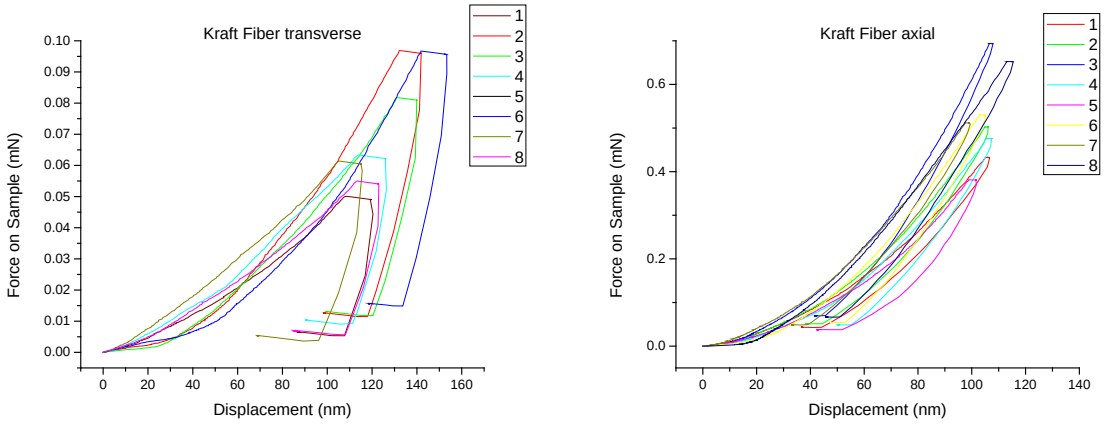

A

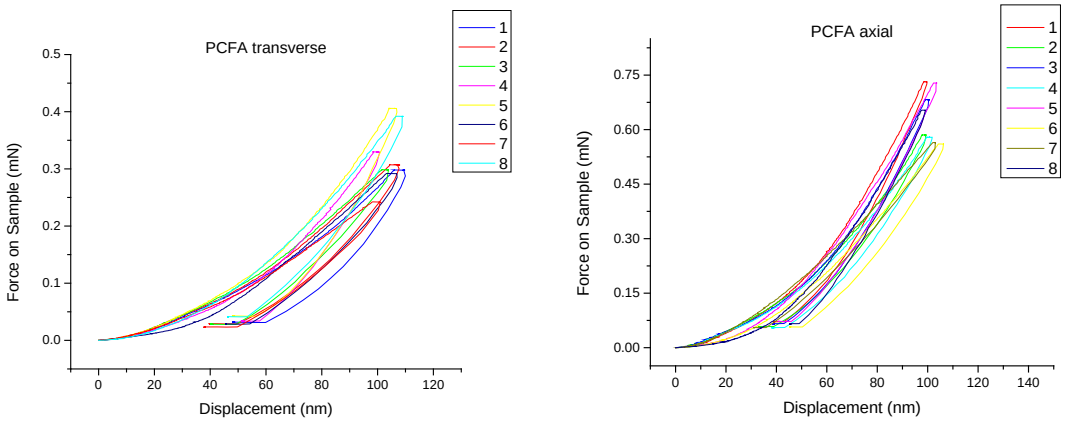

B

Figure 2-8. Loading and depth curve of carbon fibers indented in transverse and axial axis derived from (A) Kraft, (B) PCFA lignins.

2.3.6 X-Ray Photoelectron Spectroscopy (XPS)

XPS was performed to identify the state of chemical bonding of carbon in Kraft and PCFA fibers. First, a low resolution survey was performed to identify the percentage of carbon present of the surface. Table 2-7 lists all the main elements having atomic percent higher than 0.1. It shows PCFA containing more carbon percentage as compared to the Kraft carbon fiber.

Table 2-7. Atomic percentage of the surface of carbon fibers using XPS.

Sample	Element atomic (%)		
	C (at%)	O (at%)	Si (at%)
PCFA	88.07	11.93	-
Kraft Carbon	79.07	18.11	2.83

High resolution C1s regions were analyzed to get the binding characteristics of the fiber surface. The deconvolution of the C1s was performed using the PHI

MultipakTM software. The background was subtracted using the Shirley method, while the peak was fitted by Gauss-Lorentz mixed function. Figure 2-9A and 2-9B represents the C1s curve fitting using Gauss-Lorentz function of Kraft and PCFA carbon fiber. Carbon was present in three states: the graphitic (C-C) peak at 284.3-284.7 eV, the ether (C-O) or hydroxyl group (C-OH) peak at 285.9-286.5 and the carbonyl or quinine group (C=O) at binding energy of 287.1-287.9 eV [68-70].

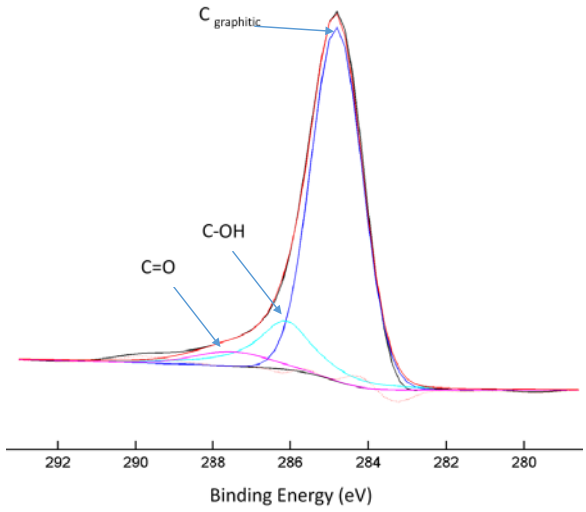

A

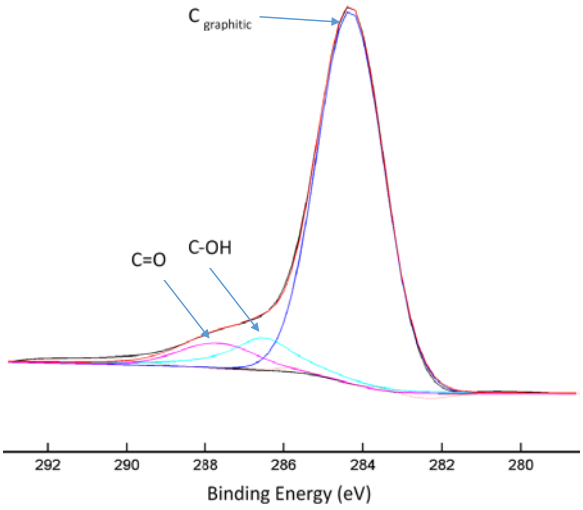

B

Figure 2-9. Deconvolution of C 1s region of (A) Kraft (B) PCFA carbon fiber.

XPS results show a higher percentage of graphitic structure of carbon in PCFA as compared to Kraft lignin (Table 2-8). It is expected to correlate to better mechanical performance as the crystallinity of the structure reinforces the fiber leading to increased modulus. This is confirmed by the nanoindentation results. The graphitic peak for XPS also correlates to the G band intensity from the Raman spectroscopy which shows a similar trend.

Table 2-8. Deconvolution of C 1s region for the Kraft and PCFA carbon fiber.

Sample	Graphite (C-C)		C-O		C=O	
	BE (eV)	M(%)	BE (eV)	M(%)	BE (eV)	M(%)
Kraft	284.7	73.16	285.9	23.47	287.1	3.37
PCFA	284.3	81.43	286.5	13.46	287.9	5.11

2.3.7 Transmission Electron Microscopy (TEM)

The TEM image and corresponding SAD ring pattern images for Kraft and PCFA carbon fibers are shown in Figure 2-10A and 2-10B respectively. Both consist of multi crystals according to the diffraction rings. There is a difference in the crystal dimensions. Kraft lignin has a smaller crystallite as compared to the PCFA. A small crystal dimension enhances tensile strength [71] whereas a large crystal enhance the stiffness and modulus of the fibers [72]. This correlates to the nanoindentation results of PCFA having higher modulus.

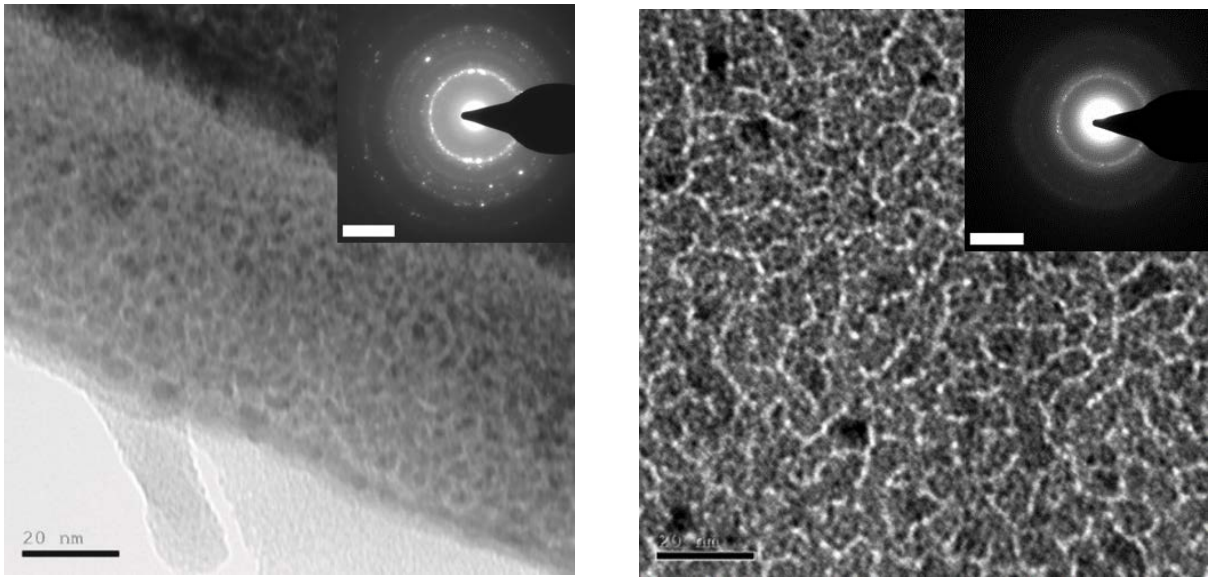

A B

Figure 2-10. TEM and electronic diffraction image of (A) Kraft (B) PCFA carbon fiber.

2.3.8 XRD

From the diffraction pattern (Figure 2-11A and B), one can observe both the Kraft and PCFA fibers show reflections at (002) and (001) plane characteristics of carbon fibers from plant sources [73]. The broader peak of (002) observed for Kraft lignin carbon fiber is indicative of a large number of small crystallites present in the fiber. Ring diffraction pattern from TEM also show a large number of crystallites for Kraft. The narrow peak and higher intensity of the (002) peak for PCFA shows higher crystallinity for PCFA fibers. The lattice parameter was calculated using Bragg's law and apparent crystallite thickness (Lc) was calculated using the Scherrer formula reported in Table 4-9. Both the fibers are in between turbostratic and graphitic structure, PCFA tends more towards graphitic structure as observe from degree of graphitization value. These

results indicates that the PCFA has a more orderly arrangement of carbon atoms as compared to the Kraft.

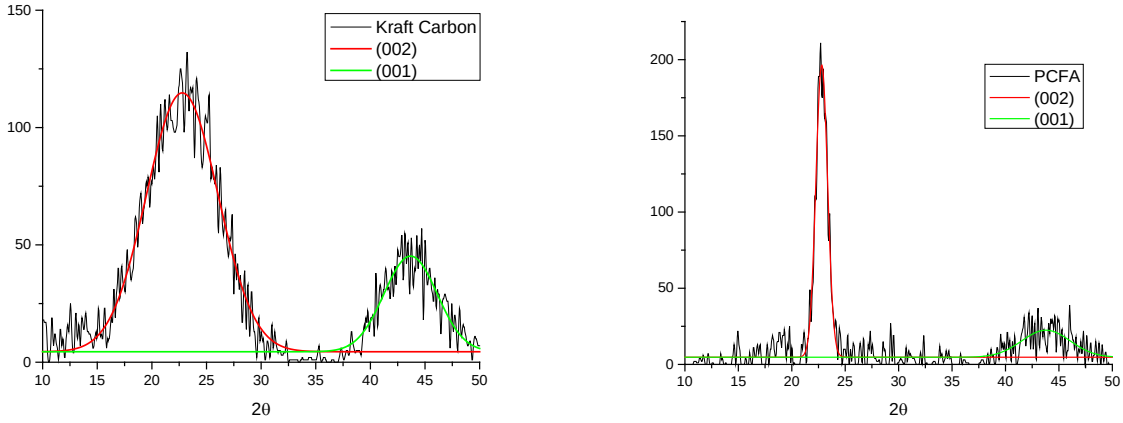

A B

Figure 2-11. X-ray diffraction pattern of (A) Kraft (B) PCFA carbon fiber.

Table 2-9. Structure parameters of X-ray diffraction of Kraft and PCFA Carbon fiber.

Sample	d(002) (nm)	d(001) (nm)	Lc (nm)	g(%)
Kraft Lignin Carbon	0.391	0.207	2.07	-5.46
PCFA	0.389	0.206	12.28	-5.23

2.3.9 Thermogravimetric Analysis (TGA)

TGA was used to assess the thermal stabilities of the obtained CFs. Figure 2-12 compares the TGA curves of Kraft and PCFA CFs up to 800 °C and the residual weights. PCFA demonstrated good thermal stability as compared to Kraft carbon fiber having 59.8 % residual weight as compared to the 16.7 % for Kraft lignin carbon fiber at 800 °C. (Table 2-10) The weight loss observed below 100 °C mainly in PCFA may be due to the moisture absorbed on the surface of the fiber as noted by others [74]. The

weight loss from 100 °C to 400 °C may be because of liable oxygen containing group present in the material [75]. Both fibers show some stability till 400 °C. There is a sudden decrease in weight for Kraft carbon and PCFA at temperature around 450 °C similar to reported by Xu et al. [47] as Tonset for carbon fiber from a 50:50 lignin/PAN source. This can be due to the removal of more stable oxygen functionalities [76]. PCFA seems more stable overs the temperature range which it is comparable to the carbonized lignin/PAN fiber thermal stability which was shown by Xu et al. [47]. The residual is 76.1 % wt. at 700 °C as compared to 67.9% for PCFA at the same temperature.

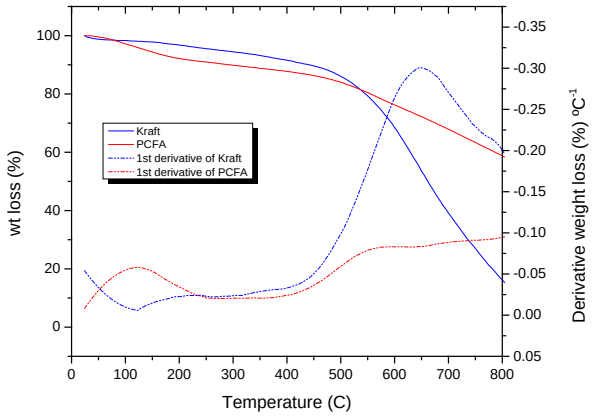

Figure 2-12. TGA curve and 1st derivative of Kraft and PCFA carbon fiber.

Table 2-10. Residue weights of Kraft and PCFA Carbon Fibers at different temperatures determined by TGA.

Sample	Residue weight (wt.%)		
	400 °C	600 °C	800 °C
PCFA	87.7	76.2	59.8
Kraft	91.4	68.3	16.7

2.4 Conclusions

In this chapter we have reported the formation of PCFA-based carbon fiber, and compared its properties to those of fibers derived from Kraft lignin. Kraft-lignin had a higher molecular weight than PCFA, and the percentage of carbon in the Kraft lignin was higher than in PCFA prior to pyrolysis arising from differences in their lignins. Notable to our approach is that the fibers were successfully electrospun directly from solution without any chemical treatment or addition of polymers to provide fiber extensional flow strength. Kraft lignin in the unmodified state (no coaxial die with ethanol coating or blended polymers used by others to produce sub-micron Kraft fibers) produced fibers that were of high diameter (~50 μm). In contrast, the PCFA-sourced carbon fibers were of low diameter (~10 μm). Carbonization at 900 °C imparted more graphitic properties to the PCFA carbon than to the Kraft lignin, as seen from G/D ratios of 1.92 vs 1.15 respectively. In this respect, the PCFA-derived carbon compares very well to commercial carbon from PAN and approaches that based on pitch. The carbon content is around 86 % for both lignin bio-sources of carbon based on elemental analysis. Higher G band peaks are associated with both crystal perfection and low impurities. Nanoindentation results showed that the carbon from PCFA and Kraft had comparable axial moduli compared to commercial carbon. The transverse moduli of the PCFA was better than Kraft and commercial carbon fibers. XPS results show 88% graphitic C-C bond for PCFA as compared to 79% for the Kraft lignin indicating higher crystallinity, which can be correlated to high G/D Raman ratio for PCFA. Moreover, from the XRD and TEM a larger crystal size for the PCFA fiber was obtained which is correlates to the higher nanoindentation modulus of the fiber. TGA curves also show

higher thermal stability for PCFA indicating higher graphitization. The higher impurities in Kraft lignin were reflected in the zeta potential higher ionic conductivity and lower mobility compared to PCFA carbon. The carbon from both lignin showed good dispersion stability in DI water. On the basis of our results, PCFA appears to be a promising new renewable source of both carbon fibers and pure carbon. The subject of our further research will be to shift PFCA lignin extraction to green chemistry by applying steam explosion combined with enzymatic hydrolysis.

2.5 References:

[1] G. Williams, R. Trask, I. Bond, A self-healing carbon fibre reinforced polymer for aerospace applications, Composites Part A: Applied Science and Manufacturing, Volume 38, Issue 6, June 2007, Pages 1525-1532

[2] Sastri, S. B., Armistead, J. P. and Keller, T. M. (1996), Phthalonitrile-carbon fiber composites. Polym Compos, 17: 816–822. doi: 10.1002/pc.10674

[3] D.D.L Chung, Electromagnetic interference shielding effectiveness of carbon materials, Carbon, Volume 39, Issue 2, February 2001, Pages 279-285

[4] Naoto Saito,Kaoru Aoki, Yuki Usui, Masayuki Shimizu, Kazuo Hara, Nobuyo Narita, Nobuhide Ogihara, Koichi Nakamura, Norio Ishigaki, Hiroyuki Kato, Hisao Haniu,c Seiichi Taruta,d Yoong Ahm Kimd and Morinobu Endod, Application of carbon fibers to biomaterials: A new era of nano-level control of carbon fibers after 30-years of development , Chem. Soc. Rev., 2011, 40, 3824–3834.

[5] James F. Snyder, Emma L. Wong, and Clifford W. Hubbard, Evaluation of Commercially Available Carbon Fibers, Fabrics, and Papers for Potential Use in Multifunctional Energy Storage Applications, Journal of The Electrochemical Society, 156 A215-A224 2009.

[6] Marcus Rose,Emanuel Kockrick,Irena Senkovska,Stefan Kaskel, High surface area carbide-derived carbon fibers produced by electrospinning of polycarbosilane precursors , Carbon Volume 48, Issue 2, February 2010, Pages 403–407.

[7] V. B. Fedorov, M. Kh. Shorosov, D. K. Khakimova, Carbon and Its Reactions with Metals, Metallurgiya, Moscow 1978.

[8] MInus, M., and Kumar, S. (2005). The processing, properties, and structure of carbon fibers. Jom, 57(2), 52-58.

[9] Wangxi, Z., Jie, L., and Gang, W. (2003). Evolution of structure and properties of PAN precursors during their conversion to carbon fibers. Carbon, 41(14), 2805-2812.

[10] Rahaman, M. S. A., Ismail, A. F., and Mustafa, A. (2007). A review of heat treatment on polyacrylonitrile fiber. Polymer Degradation and Stability, 92(8), 1421-1432.

[11] Mavinkurve, A., Visser, S., and Pennings, A. J. (1995). An initial evaluation of poly (vinylacetylene) as a carbon fiber precursor. Carbon, 33(6), 757-761.

[12] Horikiri, S., Iseki, J., and Minobe, M. (1978). U.S. Patent No. 4,070,446. Washington, DC: U.S. Patent and Trademark Office.

[13] Newell, J. A., and Edie, D. D. (1996). Factors limiting the tensile strength of PBO-based carbon fibers. Carbon, 34(5), 551-560.

[14] Jason Hilla, Stephen Polaskya, Erik, Nelsonc, David Tilmanb, Hong Huod, Lindsay Ludwige, James Neumanne, Haochi Zhenga, and Diego Bontaa, Climate change and health costs of air emissions from biofuels and gasoline, PNAS February 10, 2009 vol. 106 no. 6 2077-2082.

[15] Compere, A. L., Griffith, W. L., Leitten, C. F., and Shaffer, J. T. (2001, August). Low cost carbon fiber from renewable resources. In International SAMPE Technical Conference (Vol. 33, pp. 1306-1314).

[16] Ragauskas, A. J., Beckham, G. T., Biddy, M. J., Chandra, R., Chen, F., Davis, M. F., Davison, B. H., Dixon, R. A., Gilna, P., Keller, M., Langan, P., Naskar, A. K., Saddler, J. N., Tschaplinski, T. J., Tuskan, G. A., and Wyman, C. E. (2014). Lignin valorization: improving lignin processing in the biorefinery. . Science 344, 709

[17] Chen, F., and Dixon, R.A. (2007). Lignin modification improves fermentable sugar yields for biofuel production. Nature Biotechnology 25, 759-761.

[18] Reddy, M.S.S., Chen, F., Shadle, G.L., Jackson, L., Aljoe, H., and Dixon, R.A. (2005). Targeted down-regulation of cytochrome P450 enzymes for forage quality improvement in alfalfa (Medicago sativa L.). Proc Natl Acad Sci USA 102, 16573-16578

[19] Vanholme, R., Morreel, K., Darrah, C., Oyarce, P., Grabber, J.H., Ralph, J., and Boerjan, W. (2012). Metabolic engineering of novel lignin in biomass crops. New Phytologist 196, 978-1000.

[20] Tsuji, Y., Vanholme, R., Tobimatsu, Y., Ishikawa, Y., Foster, C. E., Kamimura, N., et al. (2015). Introduction of chemically labile substructures into arabidopsis lignin through the use of LigD, the Cα-dehydrogenase from sphingobium sp. strain SYK-6. Plant Biotechnology Journal, 13(6), 821-832.

[21] Sjöström, E. Wood Chemistry: Fundamentals and Application. Academic Press: Orlando. 293 pp. (1993).

[22] Pearl, I.W. The Chemistry of Lignin. Marcel Dekker, Inc.: New York. 339 pp. (1967).

[23] Boerjan, W., Ralph, J., and Baucher, M. (2003). Lignin biosynthesis. Annual Review of Plant Biology 54, 519-546.

[24] Ralph, J.; Lundquist, K.; Brunow, G.; Lu, F.; Kim, H.; Schatz, P. F.; Marita, J. M.; Hatfield, R. D.; Ralph, S. a.; Christensen, J. H.; Boerjan, W. Lignins: Natural polymers from oxidative coupling of 4-hydroxyphenyl- propanoids. Phytochemistry Reviews 2004, 3, 29–60.

[25] Patil, R. A. (2012). “Cleaveage of acetyl groups of acetic acid production in Kraft pulp mills.” Thesis, University of Maine.

[26] Kocheva, L.S.; Karmanov, A.P.; Mironov, M.V.; Belyi, V.A.; Belyaev, V.Y.; Monakov, Y.B. Straw lignins: Hydrodynamic and conformational properties of the macromolecules. Russ. J.Appl. Chem. 2008, 81, 2033-2039.

[27] Chen, F., Tobimatsu, Y., Havkin-Frenkel, D., Dixon, R.A., and Ralph, J. (2012). A polymer of caffeyl alcohol in plant seeds Proceedings of the National Academy of Sciences USA 109, 1772-1777.

[28] Chen, F., Tobimatsu, Y., Jackson, L., Ralph, J., and Dixon, R.A. (2013). Novel seed coat lignins in the Cactaceae: structure, distribution and implications for the evolution of lignin diversity. . Plant Journal 73, 201-211.

[29] Tobimatsu, Y., Chen, F., Nakashima, J., Jackson, L.A., Dixon, R.A., and Ralph, J. (2013). Coexistence but independent biosynthesis of catechyl and guaiacyl/syringyl lignins in plant seeds. Plant Cell 25, 2587-2600.

[30] Thakur, V. K., Thakur, M. K., Raghavan, P., and Kessler, M. R. (2014). Progress in green polymer composites from lignin for multifunctional applications: A review. ACS Sustainable Chemistry \and Engineering, 2(5), 1072-1092. doi:10.1021/sc500087z

[31] Baker, D. A., Gallego, N. C. and Baker, F. S., On the Characterization and spinning of an organic purified lignin toward the manufacture of low-cost carbon fiber, Journal of Applied Polymer Science, 124, 227-234 (2012)

[32] Otani, S.; Fukuoka, Y.; Igarashi, B.; Sasaki, K. US Pat. 3,461,082, 1969, FR Pat. 1,458,725, (1966).

[33] Sudo, K., Shimizu. A New Carbon Fiber from Lignin, Journal of Applied Polymer Science, Vol. 44, 127-134 (1992)

[34] Sudo, K., Shimizu, K., Nakashima, N., Yokoyama, A. A New Modification Method of Exploded Lignin for the Preparation of a Carbon Fiber Precursor, Journal of Applied Polymer Science, Vol. 48, 1485-1491 (1993)

[35] Uraki, Y., S. Kubo, N. Nigo, et al. "Preparation of Carbon Fibers from Organosolv Lignin Obtained by Aqueous Acetic Acid Pulping" Holzforschung - International Journal of the Biology, Chemistry, Physics and Technology of Wood, 49.4 (2009): 343-350.

[36] S. Kubo, Y. Uraki, Y. Sano, Preparation of carbon fibers from softwood lignin by atmospheric acetic acid pulping, Carbon, Volume 36, Issues 7–8, 1998, Pages 1119-1124

[37] Mai, C., Majcherczyk, A., Hüttermann, A. Chemo-enzymatic synthesis and characterization of graft copolymers from lignin and acrylic compounds, Enzyme and Microbial Technology 27 (2000) 167–175

[38] Xiao, B., Sun, X.F., Sun, R.C. The chemical modification of lignins with succinic anhydride in aqueous systems, Polymer Degradation and Stability, Volume 71, Issue 2, 2001, Pages 223–231

[39] Lallave, M., Bedia, J., Ruiz-Rosas, R., Rodriguez-Mirasol, J., Cordero, T., Otero, J.C., marquez, M., Barrero, A., Loscertales, I.jG. Filled and Hollow Carbon Nanofibers by Coaxial Electrospinning of Alcell Lignin without Binder. Polymers, Volume 19, Issue 23, Article first published online: 29 NOV 2007

[40] Kadla, J.F., Kubo, s., Gilbert, R.D., Venditti, R.A., Compere, A.L., Griffith, W.L.Lignin-based carbon fibers for composite fiber applications, Carbon 40 (2002) 2913–2920

[41] Kubo, S. and Kadla, J. F. (2005), Kraft lignin/poly(ethylene oxide) blends: Effect of lignin structure on miscibility and hydrogen bonding. J. Appl. Polym. Sci., 98: 1437–1444.

[42] Satoshi Kubo and and John F. Kadla, Poly(Ethylene Oxide)/Organosolv Lignin Blends: Relationship between Thermal Properties, Chemical Structure, and Blend Behavior, Macromolecules 2004, 37, 6904-6911

[43] S. Kubo, J. F. Kadla Lignin-based Carbon Fibers: Effect of Synthetic Polymer Blending on Fiber Properties, Journal of Polymers and the Environment, Vol. 13, No. 2, April 2005

[44] Jian Lin, Satoshi Kubo, Tatsuhiko Yamada, Keiichi Koda, Yasumitsu Urak, Chemical Thermostabilization for the preparation of carbon fibers from softwood lignin, BioResources 7(4), 5634-5646

[45] Mariko Ago, Kunihiko Okajima, Joseph E. Jakes, Sunkyu Park, and Orlando J. Rojas, Lignin-Based Electrospun Nanofibers Reinforced with Cellulose Nanocrystals, Biomacromolecules 2012 13 (3), 918-926

[46] Seo, D.K., Jeun, J.P., Kim, H.B., Kang, P.H. Preparation and characterization of the carbon nanofibers mat produced from electrospun PAN/lignin precursors by electron beam irradiation. Rev Adv Mater Sci 2011;28:31-34.

[47] Xu, X., Zhou, J., Jiang, L, Lubineau, G., Payne, S.A., Gutschmidt, D. Lignin-based carbon fibers: Carbon nanotube decoration and superior thermal stability. Carbon 2014;80:91-102.

[48] Glasser, W.G., Davé, V., Frazier, C.E. (1993) Molecular Weight Distribution of (Semi-) Commercial Lignin Derivatives, J Wood Chem Technol 13 (4), 545-559.

[49] Norberg, I., Nordström, Y., Drougge, R., Gellerstedt, G., Sjöholm, E. A new method for stabilizing softwood Kraft lignin fibers for carbon fiber production. J Appl Polym Sci 2013: 38588

[50] X. Li, B. Bhushan (2002) A review of nanoindentation continuous stiffness measurement technique and its applications Mater. Character. 48, pp. 11–36

[51] W.C. Oliver and G.M. Pharr, An improved technique for determining hardness and elastic modulus using load and displacement sensing indentation experiments, Journal of Materials Research, Volume 7, Number 6, pp. 1564 – 1583, June 1992.

[52] J.L. Hay and G.M. Pharr, Instrumented indentation testing, ASM Handbook, Mechanical Testing and Evaluation, Volume 8, pp. 232-243, October 2000.

[53] Pan, X., Sano, Y. (2005) Fractionation of wheat straw by atmospheric acetic acid process. Bioresource Technol. 96 (11), 1256-1263

[54] Bledzki, A.K., Sperber, V.E., Faruk, O. (2002) Structure and Chemical Constituents of fibres, In: Natural and Wood Fibre Reinforcement in Polymers, Rapra Review Reports 13 (8), Rapra Technology Limited, Shawbury, United Kingdom, p. 12

[55] Buranov, A.U., Mazza, G. (2008) Lignin in straw of herbaceous crops. Ind. Crops Prod. 28, 237-259

[56] S. Manandhar, S. Vidhate, N. A. D'Souza, "Water soluble levan polysaccharide biopolymer electrospun fibers", Carbohydrate Polymers, 78, 794-798, 2009.

[57] Pierson, H. O., Handbook of carbon, graphite, diamond and fullerenes: properties, processing and applications, Noyes Publications (1993)

[58] Ruiz-Rosas, R., Bedia, J., Lallave, M., Loscertales, I. G., Barrero, A., Rodríguez-Mirasol, J., and Cordero, T. (2010). The production of submicron diameter carbon fibers by the electrospinning of lignin. Carbon, 48(3), 696-705.

[59] K. K. Kim, J. S. Park, S. J. Kim et al., “Dependence of Raman spectra G_ band intensity on metallicity of single-wall carbon nanotubes,” Physical Review B, vol. 76, no. 20, Article ID 205426, 2007.

[60] Ramani Venugopalan, D. Sathiyamoorthy, R. Acharya, A.K. Tyagi, Neutron irradiation studies on low density pan fiber based carbon/carbon composites, Journal of Nuclear Materials 404 (2010) 19–24.

[61] Zhiqiang Maa, Ekaterina Troussarda,b, Jeroen A. van Bokhovena, Controlling the selectivity to chemicals from lignin via catalytic fast pyrolysis, Applied Catalysis A: General 423– 424 (2012) 130– 136.

[62] Díez-Pascual, Ana M., Marián A. Gómez-Fatou, Fernando Ania, and Araceli Flores. 2015. Nanoindentation in polymer nanocomposites. Progress in Materials Science 67 (0) (1): 1-94.

[63] R. Longtin, C. Fauteux, E. Coronel, U. Wiklund, J. Pegna, M. Boman (2004), Nanoindentation of carbon microfibers deposited by laser-assisted chemical vapor deposition. Applied Physics A, Volume 79, Issue 3, pp 573-577

[64] R. Maurin, P. Davies, N. Baral, C. Baley, Transverse properties of carbon fibres by nano-indentation and micro-mechanics, Appl Comp Mater, 15 (2008), pp. 61–73

[65] Huson, Mickey G., Jeffrey S. Church, Abdullah A. Kafi, Andrea L. Woodhead, Jiyi Khoo, M. S. R. N. Kiran, Jodie E. Bradby, and Bronwyn L. Fox. 2014. Heterogeneity of carbon fibre. Carbon 68 (0) (3): 240-9.

[66] Gindl-Altmutter, Wolfgang, Christian Fürst, Arunjunai raj Mahendran, Michael Obersriebnig, Gerhard Emsenhuber, Marcel Kluge, Stefan Veigel, Jozef Keckes, and Falk Liebner. 2015. Electrically conductive Kraft lignin-based carbon filler for polymers. Carbon 89 (0) (8): 161-8.

[67] Fan, Zheqiong, Ruixuan Tan, Kejian He, Mingyu Zhang, Wangshu Peng, and Qizhong Huang. 2015. Preparation and mechanical properties of carbon fibers with isotropic pyrolytic carbon core by chemical vapor deposition. Chemical Engineering Journal 272 (0) (7/15): 12-6.

[68] Paiva, M. C., Bernardo, C. A., and Nardin, M. (2000). Mechanical, surface and interfacial characterisation of pitch and PAN-based carbon fibres. Carbon, 38(9), 1323-1337.

[69] Wang, J., Zhao, F., Hu, Y., Zhao, R., and Liu, R. (2006). Modification of activated carbon fiber by loading metals and their performance on SO2 removal. Chinese Journal of Chemical Engineering, 14(4), 478-485.

[70] Ida Brodin, Marie Ernstsson, Göran Gellerstedt, Elisabeth Sjöholm. Oxidative stabilisation of Kraft lignin for carbon fibre production. Holzforschung. Volume 66, Issue 2, Pages 141–147, DOI: 10.1515/HF.2011.133

[71] Dongxin HE,Chengguo WANG,Yujun BAI et al. Comparison of Structure and Properties among Various PAN Fibers for Carbon Fibers. J. Mater. Sci. Technol., 2005, 21(03): 376-380 .

[72] Termonia, Y. (2000). Chapter 11 - molecular modeling of the Stress/Strain behavior of spider dragline. Pergamon Materials Series, 4, 337-349. doi:http://dx.doi.org/10.1016/S1470-1804(00)80015-2

[73] Ma, X.; Yuan, C.; Liu, X. Mechanical, Microstructure and Surface Characterizations of Carbon Fibers Prepared from Cellulose after Liquefying and Curing. Materials 2014, 7, 75-84.

[74] Yang, X., Zhang, X., Ma, Y., Huang, Y., Wang, Y., and Chen, Y. (2009). Superparamagnetic graphene oxide-Fe3O4nanoparticles hybrid for controlled targeted drug carriers. J.Mater.Chem., 19(18), 2710-2714. doi:10.1039/B821416F

[75] Tang, X., Yu, B., Hansen, R. V., Chen, X., Hu, X., and Yang, J. (2015). Grafting low contents of branched polyethylenimine onto carbon fibers to effectively improve their interfacial shear strength with an epoxy matrix. Advanced Materials Interfaces, 2(12), n/a-n/a. doi:10.1002/admi.201500122

[76] Shen, J., Yan, B., Li, T., Long, Y., Li, N., and Ye, M. Mechanical, thermal and swelling properties of poly(acrylic acid)-graphene oxide composite hydrogels, The Royal Society of Chemistry.

CHAPTER 3

BLENDING CARBON PRECURSORS FOR CONDUCTIVE TEXTILES

3.1 Introduction

Carbon fiber has become an essential engineering material for design and manufacturing due to their high mechanical strength along with temperature tolerance, high strength to weight ratio and high fracture toughness [1-2]. Their applications include but are not limited to: carbon fiber reinforced composites for aerospace industry [3], lightweight structures for automotive industry [4], carbon fiber reinforced pressure vessels for marine applications [5], flame retardants carbon fiber composites [6], energy conversion and storage devices [7-9] and fabrication of enzymatic bioelectrodes for implantable sensors [10]. Currently, the main precursors used for manufacturing carbon fiber in the industry is a polyacrylonitrile (PAN) polymer and pitch derived from a petroleum source, which contributes to almost 50% of the price of carbon fiber production [11]. To cut down the cost of production due to petroleum-based precursors, alternate biological based sources include cellulose, having low carbon yield around 10-30% [12] and lignin, having an aromatic structure rich in carbon and gives carbon yield around 45-55% [13].

Lignin consists of a random network of phenylpropanoid units linked by different functional groups. [14] These polyaromatic polymer results from the copolymerization of three p-hydroxycinnamyl alcohol monomers (p-coumaryl, conferyl and sinapyl) known as monolignols [15]. These polymerize monomers couple in different percentages to broadly divide into three categories: softwood (gymnosperm), hardwood (angiosperm) and grass or annual plant (graminaceous) lignin [16]. Investigation of lignin, as an

alternative precursor, shows a signification reduction in cost as well as CO_2 emission during carbon fiber manufacturing [11]. However, electrospinning lignin by itself is complicated due to the heterogeneity of lignin quality, low molecular weight, and viscosity. Therefore, efforts are being made to blend it with high molecular weight polymers such as polyethylene oxide (PEO) [17], polylactic acid (PLA) [18] and PAN [19,20] to increase spinnability and viscosity of the blend. Lower mechanical properties of lignin-based carbon fibers limit its potential of being utilized fully. Therefore, efforts are being made to modify the structure of lignin to enhance the inter-fiber bonding [19] and to limit impurities such as ashes by using a high boiling solvent [20] to compensate for the degraded mechanical properties.

There is a need for more suitable lignin precursors which improve the lagging: fiber spinnability and mechanical properties. Chen et al [21- 23] discovered a new class of lignin made completely from caffeyl alcohol units found in the seed coat of *V. planifolia and* Brazilian cactus *Melocactus salvadorensis.* Thioaciolysis of the lignin monomer indicates that it's a linear polymer derived from caffeyl alcohol monomers linked head to tail into benzodioxane chains via the 'endwise' radical coupling reactions that typify lignification. The dominant β-aryl ether linkage unit found in hardwood and softwood lignins derived from coniferyl and sinapyl alcohols were missing, whereas benzodioxanes accounted for over 98% of the identifiable units. Figure 3-1 shows the chemical structure of caffeyl alcohol monomer and the resulting repeated benzodioxanes unit.

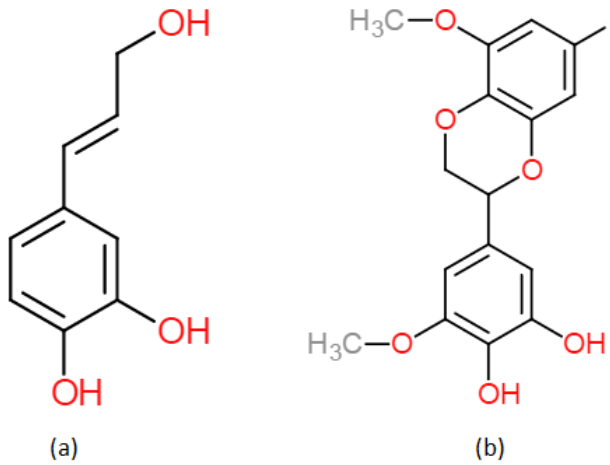

Figure 3-1. Chemical structure of (a) caffeyl alcohol monomer, (b) benzodioxanes unit.

Recently Nar et al. [24] showed carbon fiber manufactured from poly (caffely alcohol) lignin has better spinnability and mechanical properties compared to the Kraft lignin because of higher carbon content and distinct linear structure. In this paper, we examine the miscibility of PCFA with widely used precursor PAN and the structural change in the resulting carbon fibers. Thus by reducing the cost of carbon fibers while not lowering the mechanical properties of the fibers in the same percentage. We here test this hypothesis, comparing samples of PCFA/PAN blend with pure PAN precursor.

3.2 Experimental

3.2.1 Materials

PAN having average molecular weight of 150,000 and N, N-dimethylformamide (DMF) was obtained from Sigma Aldrich and was used without further purification. PCFA was extracted by grinding the seed coats of V. planifolia. To isolate PCFA, seeds were mixed with 1% NaoH in a liquid to solid ratio of 10. The mixture was heated and maintained at 120 ^{0}C for 1 h in an autoclave. The black liquid was separated from the

residue by filtration. PCFA was precipitated by adjusting the pH to 3.0 with concentrated HCl. The precipitated PCFA was separated by centrifugation, washed with water and freeze dried.

3.2.2 Electrospinning

A 10% solution of PAN, PCFA and PCFA/PAN (20:80, 40:60, 60:40) blend by weight was prepared in N, N-dimethylformamide solvent. The polymer was mixed at 50 °C for 4 h and then transferred to the syringe with an 18 gauge (0.84 mm), 1″ long stainless steel blunt needle having a Luer polypropylene hub for electrospinning at room temperature. The flow rate of the syringe pump (Model #R99-FM, Razel Scientific Instruments, St. Albans, VT) was adjusted to have a continuous flow i.e. any drop of solution wiped from the tip is immediately replaced by another. A voltage of 20-22kV was applied to the tip of the needle using a high voltage power supply (Model #ES30P-5W/DAM, Gamma High Voltage Research Inc., Ormond Beach, FL). A taylor's cone was observed at the tip of the needle that was attracted by the electrostatic force towards the grounded rotating collator at about 60 rpm. The distance between the needle and collector was kept at 20 cm to have a uniform stream from the tip.

3.2.3 Scanning Electron Microscopy (SEM)

The FEI Nova 200 NanoLab having an ultra-high resolution field emission scanning electron microscope (SEM) (FEI Company, Oregon, USA) was used to image the stabilized and carbonized electrospun PAN/PCFA fibers at an accelerating voltage

of 10 kV at 5 mm working distance. The samples were sputter coated with gold-palladium to make them conductive and make imaging possible.

3.2.4 Differential Scanning Calorimeter (DSC)

Thermal analysis was performed using a Perkin Elmer DSC6 differential scanning calorimeter, equipped with a chiller. Samples weighing 5-7 mg were placed in a nonvolatile aluminum pan. The samples were held at 30 ^{0}C for 2 minutes and then heated at a rate of 10 ^{0}C per minute from 30 ^{0}C to 400 ^{0}C. The glass transition temperature and enthalpy of fusion was calculated using the DSC data analysis software.

3.2.5 Dynamic Mechanical Analysis (DMA)

Elastic and viscous properties of the precursor fibers were examined using a dynamic mechanical analyzer RSA III (TA Instruments, New Castle, DE). The electrospun fibers meshes were cut in rectangular strips having dimensions of (15 mm × 12.5 mm) and a thickness of 0.05-0.1 mm. A dynamic temperature ramp test was performed in tensile mode from 30 ^{0}C to 150 ^{0}C to observe the glass transition and storage modulus over the temperature range. The scan was performed at a heating rate of 3 ^{0}C per min and a frequency of 1 Hz. To avoid plastic deformation a strain amplitude of 0.25% was set, which was determined by strain amplitude sweep test.

3.2.6 Fourier Transform Infrared Spectroscopy (FTIR)

FTIR spectra were obtained using a Nicolet 6700 spectrometer from Thermo Electron in ATR mode. The electrospun fibers were vacuum dried at 50 ^{0}C for 1 week.

Transmission spectra were collected from 400-4000 cm^{-1}. A minimum of 32 scans was averaged at a resolution of 4 cm^{-1}. A background reference was taken before each sample.

3.2.7 Carbonization

The thermal stabilization of the fiber mesh was performed from room temperature to 280 ^0C at a heating rate of 1 $^0C\ min^{-1}$ [24]. The fibers were held at that temperature for 60 min in an air force convection laboratory oven by cascade TEK. The stabilized fibers were then carbonized under a nitrogen flow at 0.5 standard cubic feet per hour (SCFH) in Carbolite HZS 12/600 horizontal tube furnace. The fibers were heated during the carbonization step at 5 $^0C\ min^{-1}$ to 900 ^0C at held at that temperature for 45 minutes.

3.2.8 Raman Spectroscopy

Structural order of PAN/PCFA based carbon fibers was examined using Raman spectroscopy. 532 nm intensity laser was used at 30% power with an aperture of 10 µm slit and an objective lens with a 10X zoom. The scan was done from 1000 to 2000 cm^{-1}. The exposure time was 15 s and background and sample exposure was performed 15 times. The background was subtracted from the results and a baseline correction was performed.

3.2.9 Electrical Conductivity

The conductivity of PAN/PCFA based carbon fibers was measured using a multimeter (Agilent 34401A) equipped with a two-point probe, as described in the

literature [25]. Samples of fiber mat having dimensions of 15 mm in length and 5 mm in width were used. Silver paint was applied at the end of the fiber mesh to have a uniform conductive contact. The electrical conductivity (κ) was calculated using equation 1.

$$\kappa\ (S\ cm^{-1}) = \frac{L}{wtR} \tag{1}$$

where L is the distance between the probes(cm), w is the width of the sample (cm), and t is the thickness of the sample (cm).

3.3 Results and Discussion

3.3.1 SEM

Scanning Electron Microscopy was used to observe the effect of concentration of PCFA on the morphology of precursor fibers. Image J was used to calculate the diameter of electrospun fibers. A total of 50 measurements were made for each sample. From Figure. 3-2 it can be seen that PAN fibers have the largest diameter which decreases as the concentration of PCFA is increase. The fiber diameter can be directly correlated with the viscosity of the electrospun solution, higher viscosity results in the fibers having a larger diameter. After carbonization of fibers there is on average about 35% reduction in the diameter of the fibers. Figure. 3-3 shows SEM image of stabilized and carbonized carbon fibers.

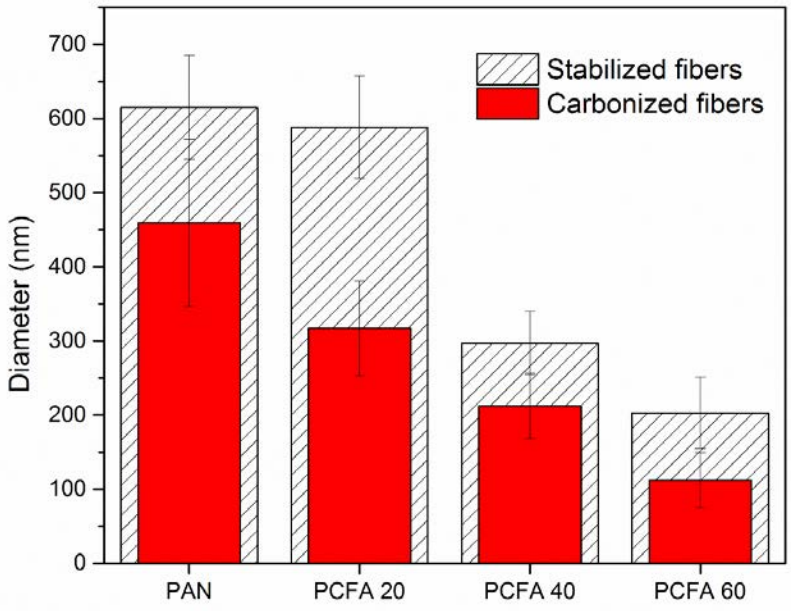

Figure 3-2. Average diameter of stabilized precursor fibers and carbonized fibers.

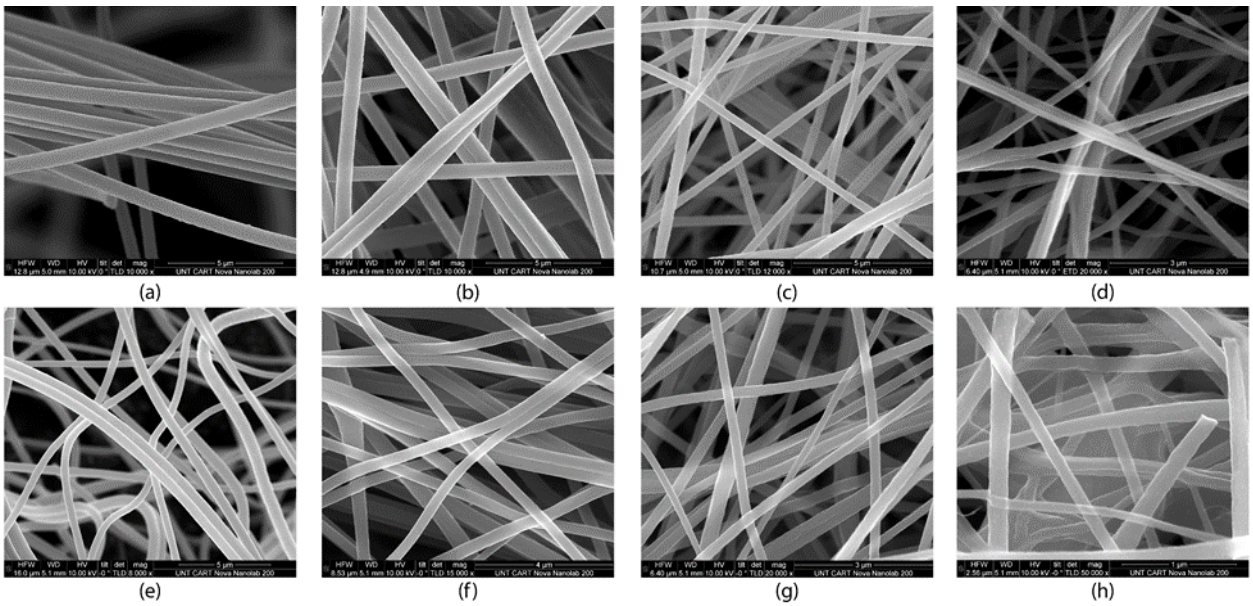

Figure 3-3. SEM images of stabilized precursor fibers (a) PAN (b) PCFA-20 (c) PCFA-40 (d) PCFA-60 and carbonized fibers (e) PAN CF (f) PCFA-20 CF (g) PCFA-40 CF (h) PCFA-60 CF.

3.3.2 Differential Scanning Calorimetry

Phase miscibility is an important parameter to consider when blending two or more materials for uniform and homogenous fibers. Measuring glass transition temperature (Tg) is an established method to identify phase homogeneity. Differential scanning calorimetry technique was used to observe the phase behavior of the blend. Glass transition temperature (Tg) was calculated using the derivative of heat flow with respect to temperature. Figure 3-4 shows heat scans of pure PCFA, PAN fibers, and their blends. Pure PAN fibers show a sharp glass transition at 101.5 ^{0}C which becomes broad for the blends. A single glass transition was observed, indicating the miscibility of the PCFA with PAN at higher loadings. For PCFA20, PCFA40 and PCFA 60 fibers the values lies in between 99 ^{0}C and 105 ^{0}C. Samples of powder PCFA show a glass transition around 115.6 ^{0}C. Figure 3-4b shows an endothermic peak for PAN and PAN/PCFA blended fibers, the enthalpy of melting reduces as the PCFA percentage is increase. Table 3-1 lists the peak temperature (Tm) and the heat of fusion (ΔHm) for the samples. The highest temperature at which the exothermic peak appeared is 316 ^{0}C for the pure PAN fibers which decreases as the lignin content is increased in the blend and becomes 310 ^{0}C for PCFA-60. This shift of Tm to lower temperature can be attributed to the increase in amorphous content (lignin) of the blend [26]. Simultaneously the shape of the endothermic peak as observed in Figure 3-4b transforms from narrow to broad. As the lignin content of the electrospun fiber increases, a decrease in the heat of fusion of the samples is also seen from -459 J/g for PAN fibers to -231 J/g for PCFA-60, i.e. a 50 percent decrease.

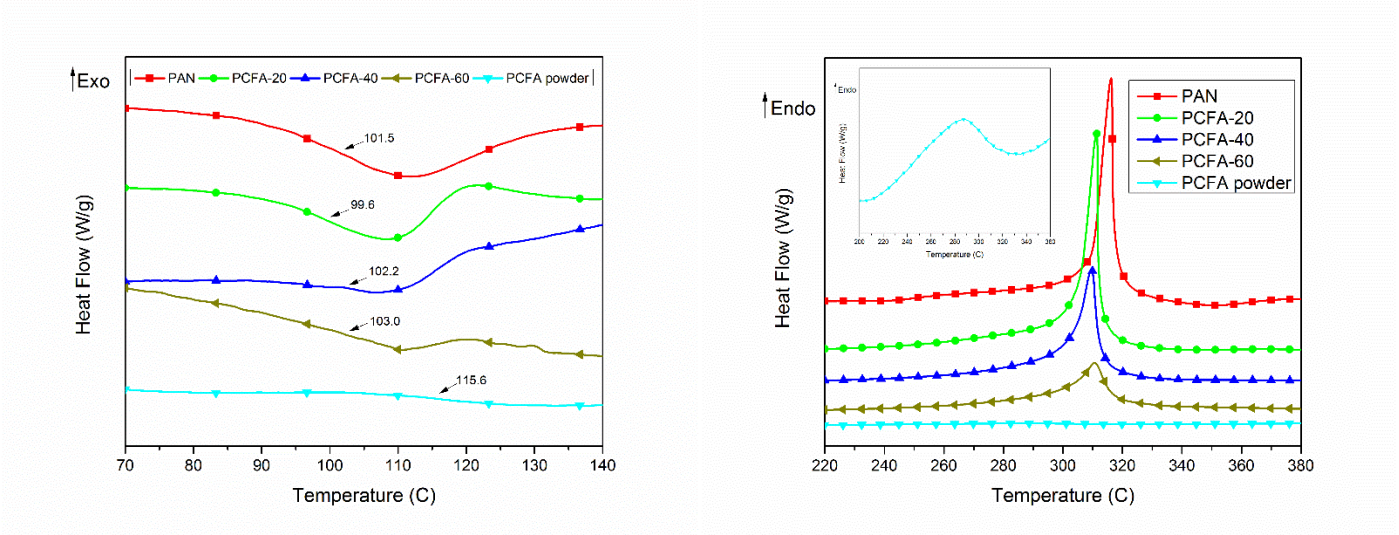

Figure 3-4. DSC scans of the precursor fibers and PCFA powder.

Table 3-1. Peak temperature (Tm) and heat of fusion (ΔHm) of PAN and PAN/PCFA fibers.

	PAN	PCFA-20	PCFA-40	PCFA-60	PCFA
T_m (^{0}C)	316	311	310	310	284
ΔH_m (J/g)	-459	-439	-404	-231	-17
T_g (^{0}C)	101.5	99.6	102.2	103	115.6

3.3.3 FTIR

FTIR analysis of electrospun PAN and PAN/PCFA fibers were performed to study the interaction of PAN with PCFA. Figure 3-5 shows the % transmittance peaks of PAN fiber, PCFA powder, and their blends. For PAN fibers, the characteristic band at 2240 cm^{-1} corresponds to the acrylonitrile unit due to stretching of –C≡N [27]. The absorption bands at 2929 cm^{-1} and 1452 cm^{-1} are associated with asymmetric stretching [28] and in-plane bending [26] of (C-H) in CH_2. The sharp band at 1664 cm^{-1} can be due to conjugated alkenyl (C=C) stretching [27]. The Figure shows the absorption bands of PCFA powder, O-H stretching band for hardwood and softwood lignin is around 3400

cm^{-1} [29] which is found around 3301 cm^{-1} for PCFA. The sharp bands at 2921 and 2852 are associated with the C-H stretching [30], band position at 1711 and 1649 is associated with the unconjugated and conjugated stretching of (C=O) respectively. Figure 3-5b shows spectra from 1650 to 700 cm^{-1}. From Figure 3-5 the distinctive 'fingerprint' bands of aromatic ring structures can be observed at 1602, 1511 and 815 cm^{-1} [31], band at 1031 corresponds to aromatic C-H in-plane deformation, absorption at 1267 and 1168 cm^{-1}, might be due to C-O and aromatic C-H in-plane deformation of the caffeyl alcohol derived ring analogous to the guaiacyl ring deformations [28]. Figure 3-5c shows the interaction of the PAN and PCFA fibers, we can observe the presence of the characteristic –C≡N stretching vibration at 2240 cm^{-1} and a sharp peak at 1452 cm^{-1} from C-H vibrations of PAN in the blend, while the intensities of the band correspond to the percentage of the blends. However, the position of these peaks did not change significantly indicative of the absence of chemical crosslinking between PAN and PCFA [32].

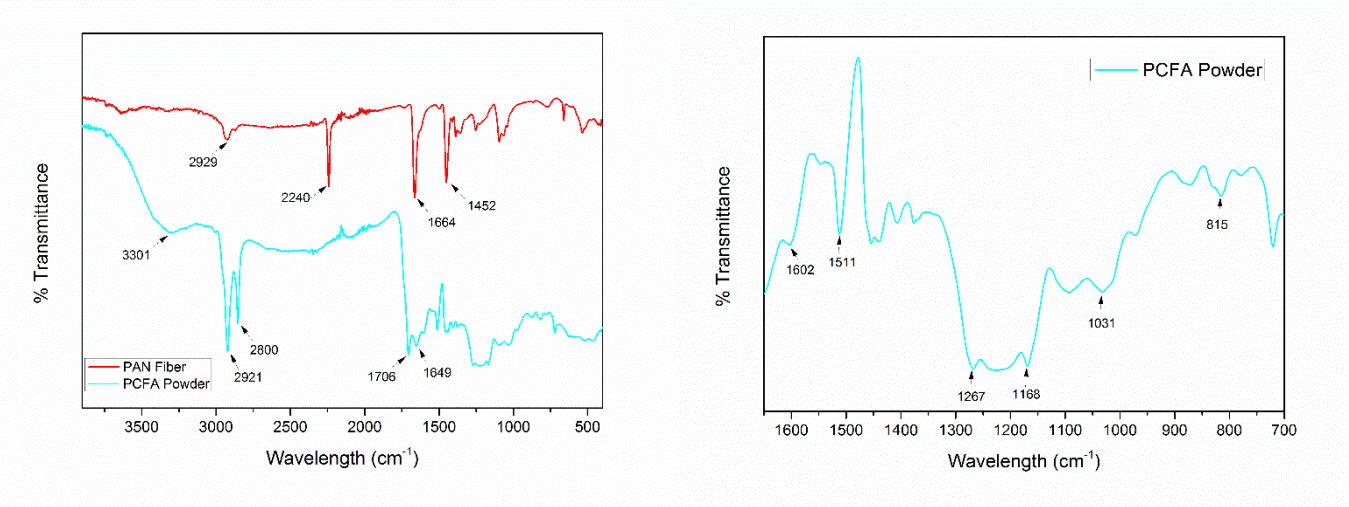

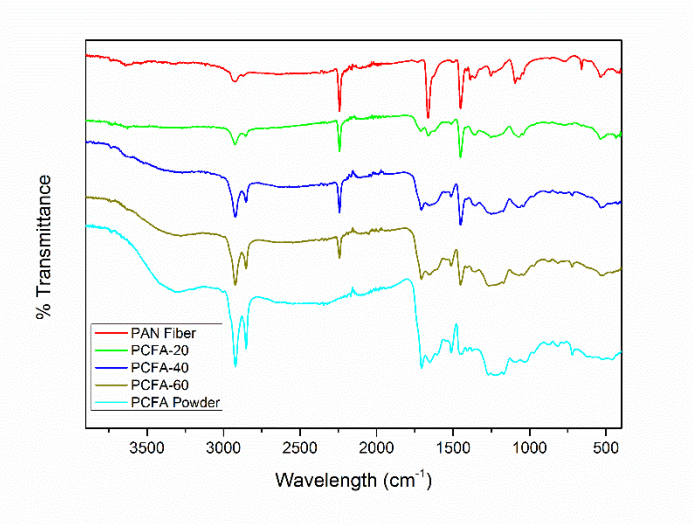

Figure 3-5. FTIR spectra of (a) PAN fibers and PCFA powder; (b) PCFA powder spectra from 1650 to 700 cm-1; (c) fiber blends with PAN & PCFA powder.

3.3.4 DMA

Dynamic mechanical analysis was performed to observe the mechanical properties of the fiber mesh over the range of temperature. Figure 3-6 shows the storage modulus and tan delta of the electrospun PAN and PAN/PCFA fibers with respect to temperature. PAN fibers exhibit the highest glassy modulus as shown in Table 3-2 which can be related to Young's modulus in static testing. PAN fibers had the highest value of modulus which tends to decrease slightly as the percentage of the lignin in the blend increases. The peak of tan δ plot is referred to the glass transition temperature that is related to the movement of the polymer chain in the paracrystalline region. [33] For PAN fibers the peak is around 95.2 ^{0}C. As the content of PCFA increases the glass transition peak is shifted to a higher temperature, indicating a decrease in the mobility of the polymer chains due to the presence of PCFA molecules. The magnitude of tan δ depicts the amount of energy consumed due to the motion in the amorphous region [34]. The decrease in magnitude and narrowing of the tan δ of

the PAN/PCFA blends indicates a tightly packed structure with a lesser movement of the chain. The higher intensity indicates more helical sequences [32] in the polymeric chain. Moreover, a single glass transition suggests a good compatibility of PAN and PCFA in the blend.

Table 3-2. Dynamic mechanical analysis of electrospun fiber meshes.

	Tg	Storage Modulus E' (MPa)			Loss Modulus (MPa)
	(^oC)	E'_{60^o}	E'_{Tg}	E'_{130^o}	E''_{peak}
PAN	95.2	254	71.9	45.7	110
PAN-20	99.6	152	47.5	21.5	21.5
PAN-40	98.2	100	31.8	17.6	13.8
PAN-60	99.6	48.7	17.8	9.56	6.75

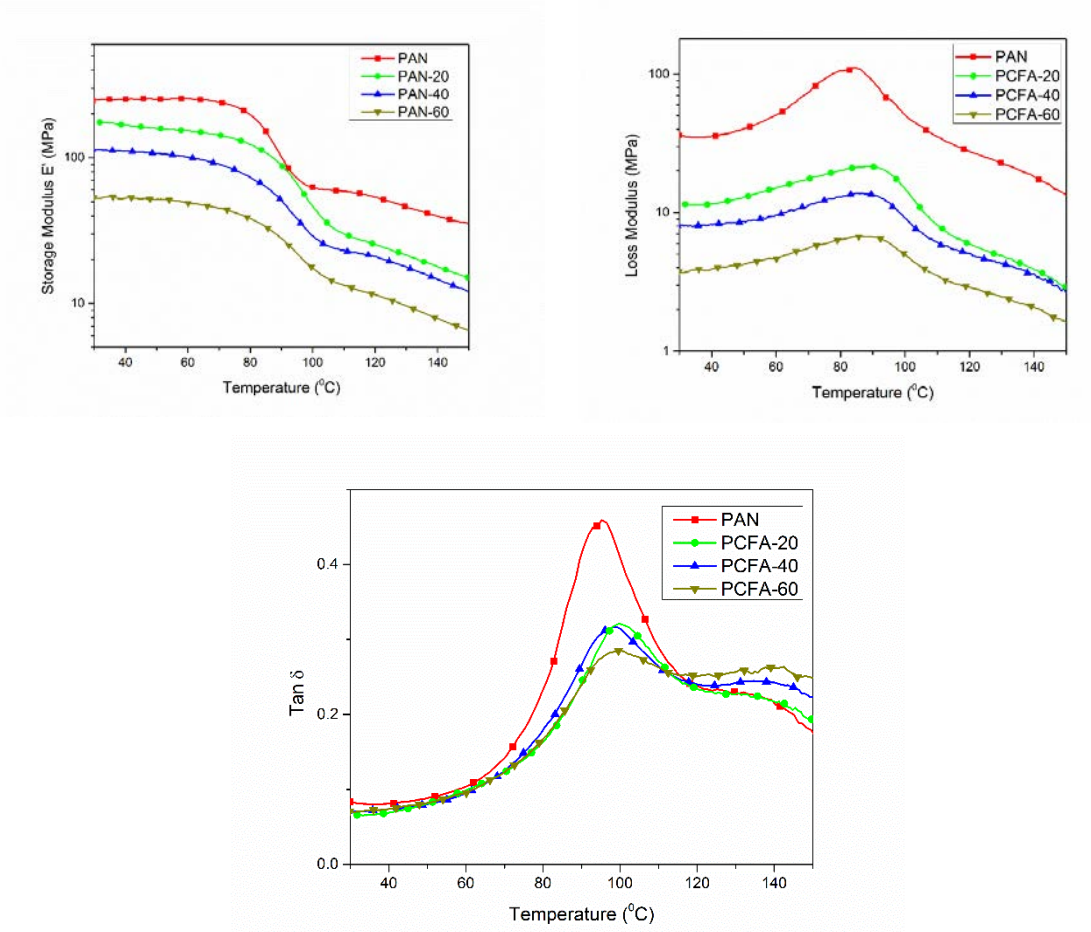

Figure 3-6. (a) Storage Modulus versus Temperature (b) Loss Modulus versus Temperature and (c) Tan Delta versus Temperature of electrospun precursor fibers.

After carbonization of the fibers we observed a constant storage modulus throughout the temperature range as shown in Figure 3-7. The PAN-60 carbon fibers shows the highest modulus due to the presence of higher crystalline structure.

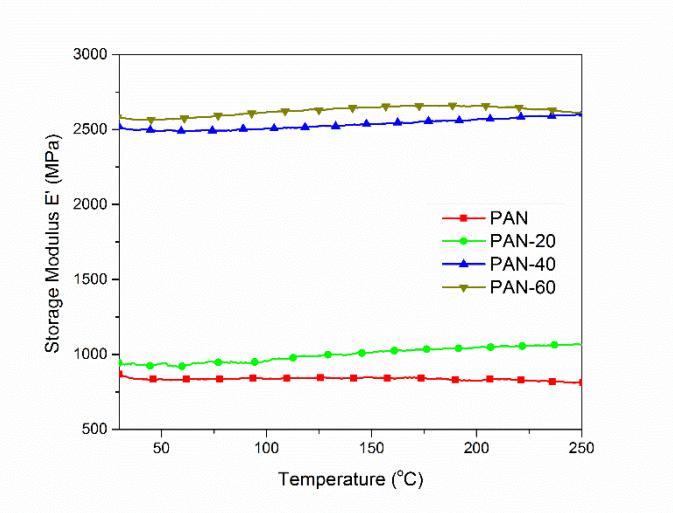

Figure 3-7. Storage Modulus versus Temperature after carbonization.

3.3.5 Raman Spectroscopy

Raman spectroscopy was performed to compare the structure of carbonized fibers obtained from different PAN/PCFA blends. First order Raman spectra of carbon fibers shown in Figure 3-8. The spectra were deconvoluted using four Gaussian bands. Two major peaks were observed at 1356 cm^{-1} and 1588 cm^{-1} corresponds to the characteristic D and G band respectively [35]. The D band represents the structural disorder which is due to breathing modes of the aromatic ring while G band is due to the in-plane stretching of sp^2 atoms representative of graphitic structure and aromatic compounds [36]. The ratio of intensities of these bands "I_G/I_D" is used to characterize the structural order of the carbon fiber. Greater the value of "I_G/I_D" higher the graphitization. The width of D (W_D) and G (W_G) are used to correlates with the disorder

of the material [37]. The peak at ~1477 cm^{-1} crosspond to the vibrations due to interstitial defects characteristic of amorphous carbon [38]. An additional peak was observed in carbon fibers having PCFA as a precursor, which may be due to the ionic impurities and/or oxygen superficial group due to incomplete volatilization during carbonization process [39].

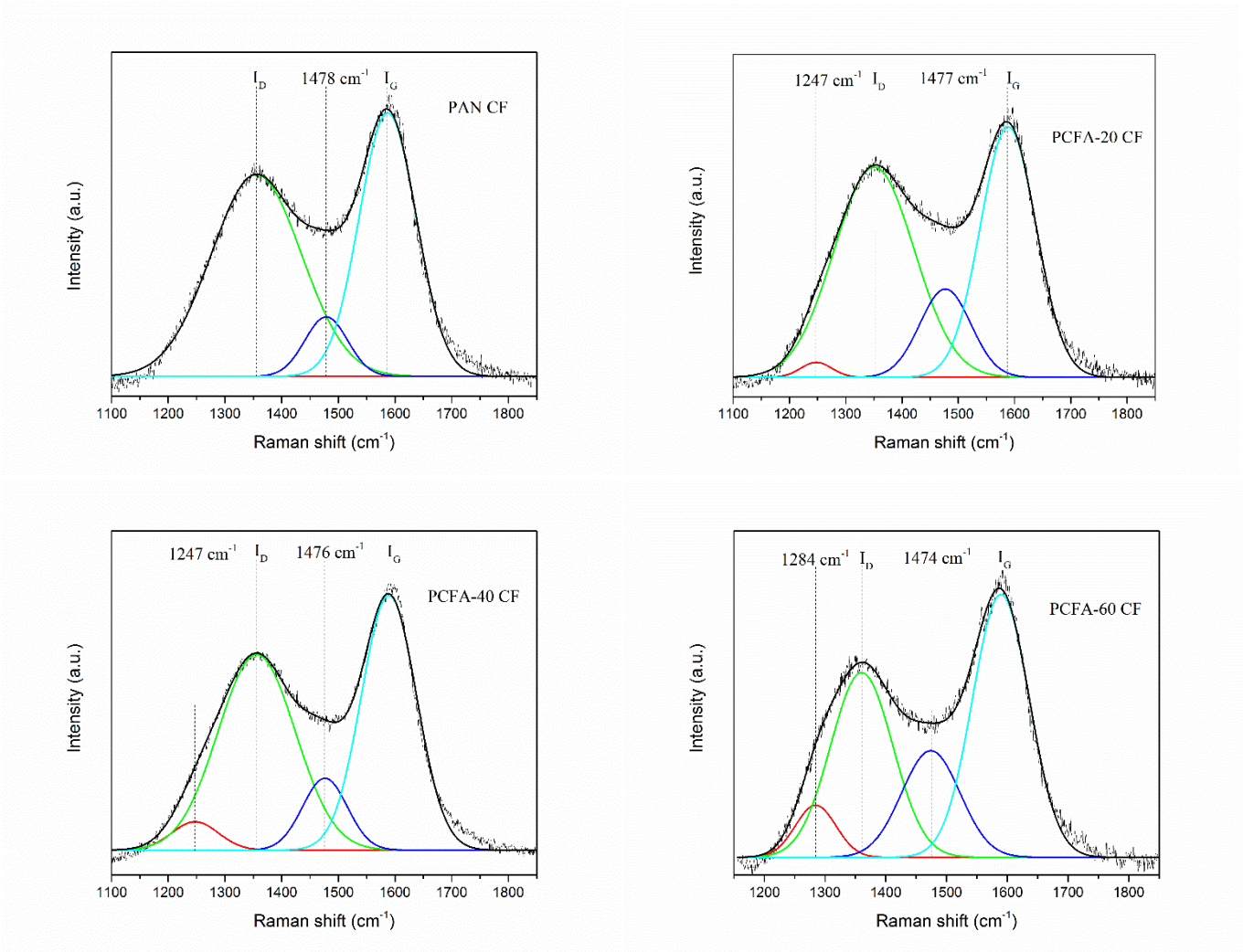

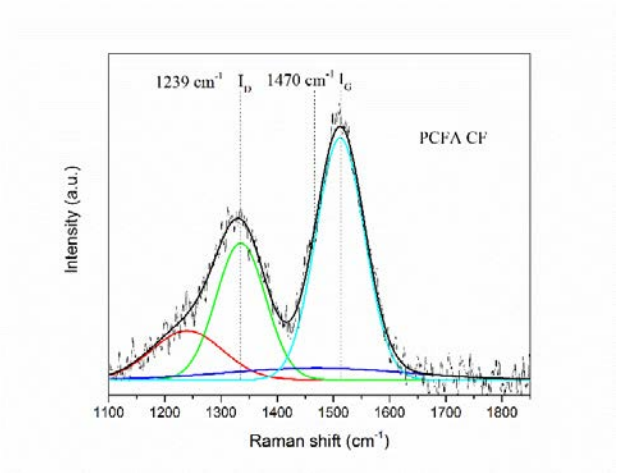

Figure 3-8. Raman deconvoluted spectra of carbonized fibers derived from PCFA/PAN blend.

As seen in Table 3-3, the percentage of G band with respect to total intensity (I_G/I_T) for all PAN based carbon fiber is around 41% with slight variation, which may be due to the experimental uncertainty. However for pure PCFA the relative intensity percentage of G band is around 49% indicating a more ordered graphitic structure as compared to PAN based carbon fibers. The ratio of intensities of G and D bands tends to increase with the percentage of the PCFA content in the precursor fiber as shown in Table 3-3. This signifies the reduction in the degree of disorder with the addition of PCFA. Moreover, FWHM of G and D band is used to show the degree of disorder in carbon based materials. Narrowing of these bands confirmed higher content of ordered graphitic structure with an increase in PCFA content of the fibers.

Table 3-3. Parameters obtained from deconvolution of Raman spectra of carbonized fibers.

	I_G/I_D	I_G/I_T (%)	W_D (cm^{-1}) FWHM	W_G (cm^{-1}) FWHM
PAN	0.82	41.8	187	118
PCFA-20	0.82	39.0	167	116
PCFA-40	0.93	41.7	160	114
PCFA-60	1.29	42.8	120	109
PCFA	1.73	48.8	103	101

3.3.6 Electrical Conductivity

Electrospun carbon nanofibers due to their higher surface area and conductivity make it strong candidates as an electrode in energy storage devices such as rechargeable batteries and supercapacitors [40-44]. Electrical conductivity of the electrospun fibers depends on the structure of nanofiber [45] inter-fiber bonding [46] as wells as the temperature at which carbonization is performed [25]. Table 3-4 shows the electrical conductivity of PAN and PCFA based fibers carbonized at 900 ^{o}C. PAN based carbon fibers have conductivity of 4.71 S cm^{-1}. The presence of PCFA causes an exponential increase in the conductivity of the carbon fiber as shown in Table 5-4. The conductivity values of PAN, PCFA 20, PCFA 40 and PCFA 60 is comparable to reported conductivity of electrospun carbon fibers derived from PAN carbonized at 800 °C (κ = 4.88 S cm−1) [47], phenolic resin carbonized at 900 °C (κ = 5.96 S cm−1) [48] and lignin-g-polyacrylonitrile copolymer carbonized at 1000 °C (κ = 7.10 S cm−1) [46]. The increase in conductivity can be due to the presence of ordered graphitic structure [49]. As observed from Raman spectroscopy, an increase in the (I_G/I_D) ratio with a higher concentration of PCFA indicates the presence of more ordered graphitic structure which enhanced the electrical conductivity of the carbon fibers. Figure 3-9 represents the prediction of conductivity based on rule of mixture of the blend as compared to the experimental values. From the Figure it can be observed that the contribution of PCFA in a blend is slightly lower as compared to the predicted value by the rule of mixture theory.

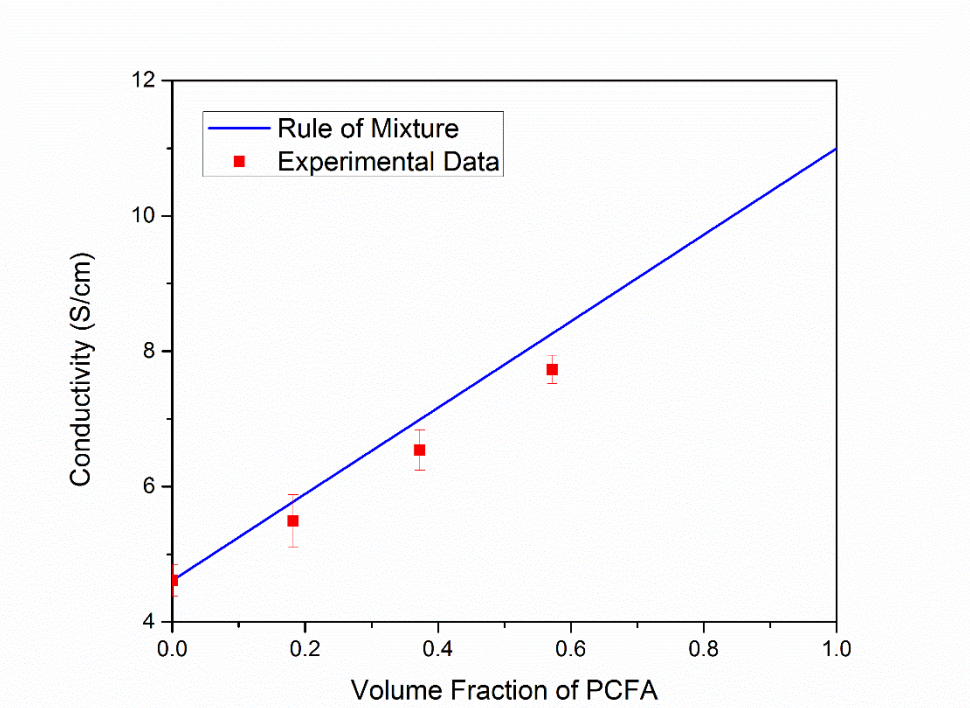

Figure 3-9. Comparison of conductivity of PCFA/PAN blend by rule of mixture and experimental data.

Table 3-4. Electrical conductivity of carbonized fibers.

	κ (S cm−1)
PAN	4.61 ± 0.23
PCFA-20	5.49 ± 0.29
PCFA-40	6.54 ± 0.30
PCFA-60	7.73 ± 0.21

3.3.7 TEM

The TEM image and selected area diffraction pattern for PCFA-60 is shown in Figure 3-10. Two distinct features can be observed in the fiber. We observed the diffuse rings due to the amorphous (non-crystalline) carbon as well as smaller crystallites which

enhanced the tensile strength [50] as shown in Figure 3-10a. Large crystals are also seen mostly in the center of the fiber having a diameter in range of 25 nm to 40 nm placed throughout the length of fiber. Micro-diffraction technique was used to get the diffraction pattern from the region of interest as shown in Figure 3-10b. The diffraction pattern corresponds to the single crystal structure, similar to the graphite structure found in a carbon mixture [51]. Similar graphitic structures were seen in electrospun lignin fibers carbonized at 1100 °C [52]. These single crystals enhance the stiffness, modulus and conductivity of the fibers. This correlates to the DMA and electrical conductivity results of PCFA-60 showing higher modulus and conductivity.

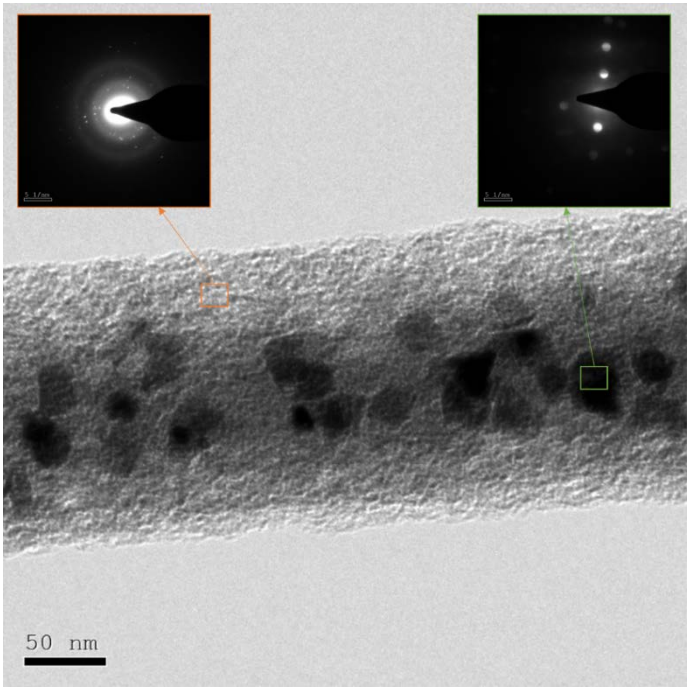

Figure 3-10. TEM and electronic diffraction pattern for PCFA-60 carbon fiber.

3.4 Conclusions

A linear lignin PCFA and PAN were combined in DMF solvent to make electrospun fibers which were then converted to carbon fibers through pyrolysis. The

effect of blend composition on the morphology of fibers was examined with an increase in the content of PCFA the diameter of as-spun fibers decreases due to lower viscosity. Smooth and bead-free fibers were obtained for up to 60 % of lignin composition. Single and broad glass transition temperature observed from thermal analysis and DMA indicates good miscibility of the two polymers. FTIR results show the presence of characteristics peak of PAN and PCFA in the blends, however the position of the peaks did not shift significantly indicating no chemical crosslinking between PCFA and PAN during the electrospinning process. Carbonization at 900 °C results in an increase in graphitic properties to the PCFA based carbon fiber than to the PAN, as seen from G/D ratios of 0.82 for PAN fibers increases to 1.29 for PCFA-60. Electrical conductivity increases exponentially with the PCFA content which can be related to the graphitic content of the fibers. On the basis of our results, blending linear lignin with PAN provides a miscible precursor fiber for low-cost carbon fiber.

3.5 References

[1] Feih, S., & Mouritz, A. P. (2012). Tensile properties of carbon fibres and carbon fibre–polymer composites in fire. Composites Part A: Applied Science and Manufacturing, 43(5), 765-772.

[2] Wang, C., Ji, X., Roy, A., Silberschmidt, V. V., & Chen, Z. (2015). Shear strength and fracture toughness of carbon fibre/epoxy interface: Effect of surface treatment. Materials & Design, 85, 800-807.

[3] Giurgiutiu, V. (2016). Chapter 2 - fundamentals of aerospace composite materials. In V. Giurgiutiu (Ed.), Structural health monitoring of aerospace composites (pp. 25-65). Oxford: Academic Press.

[4] Baskin, D. M. (2016). 4 - the automotive body lightweighting design philosophy. In J. Njuguna (Ed.), Lightweight composite structures in transport (pp. 75-90) Woodhead Publishing.

[5] Shao, Y., Betti, A., Carvelli, V., Fujii, T., Okubo, K., Shibata, O., et al. (2016). High pressure strength of carbon fibre reinforced vinylester and epoxy vessels. Composite Structures, 140, 147-156.

[6] Toldy, A., Szlancsik, Á., & Szolnoki, B. (2016). Reactive flame retardancy of cyanate ester/epoxy resin blends and their carbon fibre reinforced composites. Polymer Degradation and Stability, 128, 29-38.

[7] Peng, S., Li, L., Kong Yoong Lee, J., Tian, L., Srinivasan, M., Adams, S., et al. (2016). Electrospun carbon nanofibers and their hybrid composites as advanced materials for energy conversion and storage. Nano Energy, 22, 361-395.

[8] Zhang, B., Kang, F., Tarascon, J., & Kim, J. (2016). Recent advances in electrospun carbon nanofibers and their application in electrochemical energy storage. Progress in Materials Science, 76, 319-380.

[9] Zhao, M., Wang, J., Chong, C., Yu, X., Wang, L., & Shi, Z. An electrospun lignin/polyacrylonitrile nonwoven composite separator with high porosity and thermal stability for lithium-ion batteries - The Royal Society of Chemistry.

[10] Pereira, A. R., de Souza, J. C. P., Iost, R. M., Sales, F. C. P. F., & Crespilho, F. N. Application of carbon fibers to flexible enzyme electrodes. Journal of Electroanalytical Chemistry.

[11] Mainka, H., Täger, O., Körner, E., Hilfert, L., Busse, S., Edelmann, F. T., et al. (2015). Lignin – an alternative precursor for sustainable and cost-effective automotive carbon fiber. Journal of Materials Research and Technology, 4(3), 283-296.

[12] Ma, X.; Yuan, C.; Liu, X. Mechanical, Microstructure and Surface Characterizations of Carbon Fibers Prepared from Cellulose after Liquefying and Curing. Materials 2014, 7, 75-84.

[13] Baker, D. A., & Rials, T. G. (2013). Recent advances in low-cost carbon fiber manufacture from lignin. Journal of Applied Polymer Science, 130(2), 713-728.

[14] Sjöström, E. Wood Chemistry: Fundamentals and Application. Academic Press: Orlando. 293 pp. (1993).

[15] Boerjan, W.; Ralph, J.; Baucher, M. Lignin biosynthesis. Annual review of plant biology 2003, 54, 519–46.

[16] Pearl, I.W. The Chemistry of Lignin. Marcel Dekker, Inc.: New York. 339 pp. (1967).

[17] Understanding the impact of poly(ethylene oxide) on the assembly of lignin in solution toward improved carbon fiber production - American Chemical Society.

[18] Wang, S., Li, Y., Xiang, H., Zhou, Z., Chang, T., & Zhu, M. (2015). Low cost carbon fibers from bio-renewable Lignin/Poly(lactic acid) (PLA) blends. Composites Science and Technology, 119, 20-25.

[19] Ding, R., Wu, H., Thunga, M., Bowler, N., & Kessler, M. R. (2016). Processing and characterization of low-cost electrospun carbon fibers from organosolv lignin/polyacrylonitrile blends. Carbon, 100, 126-136.

[20] Lignin/Polyacrylonitrile composite hollow fibers prepared by wet-spinning method - American Chemical Society. doi:- 10.1021/acssuschemeng.6b00351

[21] Chen, F., Tobimatsu, Y., Havkin-Frenkel, D., Dixon, R.A., and Ralph, J. (2012). A polymer of caffeyl alcohol in plant seeds Proceedings of the National Academy of Sciences USA 109, 1772-1777.

[22] Chen, F., Tobimatsu, Y., Jackson, L., Ralph, J., and Dixon, R.A. (2013). Novel seed coat lignins in the Cactaceae: structure, distribution and implications for the evolution of lignin diversity. . Plant Journal 73, 201-211.

[23] Tobimatsu, Y., Chen, F., Nakashima, J., Jackson, L.A., Dixon, R.A., and Ralph, J. (2013). Coexistence but independent biosynthesis of catechyl and guaiacyl/syringyl lignins in plant seeds. Plant Cell 25, 2587-2600.

[24] Nar, M., Rizvi, H. R., Dixon, R. A., Chen, F., Kovalcik, A., & D'Souza, N. (2016). Superior plant based carbon fibers from electrospun poly-(caffeyl alcohol) lignin. Carbon, 103, 372-383.

[25] Youe, W., Lee, S., Lee, S., Lee, S., & Kim, Y. S. (2016). Characterization of carbon nanofiber mats produced from electrospun lignin-g-polyacrylonitrile copolymer. International Journal of Biological Macromolecules, 82, 497-504.

[26] Sallem-Idrissi, N., Sclavons, M., Debecker, D. P., & Devaux, J. (2016). Miscible raw lignin/nylon 6 blends: Thermal and mechanical performances. Journal of Applied Polymer Science, 133(6).

[27] Ouyang, Q., Cheng, L., Wang, H., & Li, K. (2008). Mechanism and kinetics of the stabilization reactions of itaconic acid-modified polyacrylonitrile. Polymer Degradation and Stability, 93(8), 1415-1421.

[28] Kim, M., Nam, D., Park, H., Kwon, C., Eom, K., Yoo, S., et al. Cobalt-carbon nanofibers as an efficient support-free catalyst for oxygen reduction reaction with a systematic study of active site formation - The Royal Society of Chemistry.

[29] Poletto, Matheus, & Zattera, Ademir J.. (2013). Materials produced from plant biomass: part III: degradation kinetics and hydrogen bonding in lignin. Materials Research, 16(5), 1065-1070. Epub July 16, 2013.

[30] Pandey, K. K. (1999), A study of chemical structure of soft and hardwood and wood polymers by FTIR spectroscopy. J. Appl. Polym. Sci., 71: 1969–1975.

[31] Barsberg, S., Rasmussen, H. N., & Kodahl, N. (2013). Composition of cypripedium calceolus (orchidaceae) seeds analyzed by attenuated total reflectance IR spectroscopy: In search of understanding longevity in the ground. American Journal of Botany, 100(10), 2066-2073.

[32] Dong, X., Lu, C., Zhou, P., Zhang, S., Wang, L., & Li, D. Polyacrylonitrile/lignin sulfonate blend fiber for low-cost carbon fiber - The Royal Society of Chemistry.

[33] Sawai, D., Kanamoto, T., Yamazaki, H., & Hisatani, K. (2004). Dynamic mechanical relaxations in poly(acrylonitrile) with different stereoregularities. Macromolecules, 37(8), 2839-2846. doi:10.1021/ma0352330

[34] Chang, J., He, M., Niu, H., Sui, G., & Wu, D. (2016). Structures and properties of polyimide/polyacrylonitrile blend fibers during stabilization process. Polymer, 89, 102-111.

[35] H.O. Pierson, Handbook of Carbon, Graphite, Diamond and Fullerenes: Properties, Processing and Applications, Noyes Publications, 1993.

[36] Ferrari, A. C., & Robertson, J. (2000). Interpretation of raman spectra of disordered and amorphous carbon. Phys.Rev.B, 61(20), 14095-14107.

[37] Cuesta, A., Dhamelincourt, P., Laureyns, J., Martínez-Alonso, A., & Tascón, J. M. D. (1994). Raman microprobe studies on carbon materials. Carbon, 32(8), 1523-1532.

[38] Ess, M. N., Ferry, D., Kireeva, E. D., Niessner, R., Ouf, F., & Ivleva, N. P. (2016). In situ raman microspectroscopic analysis of soot samples with different organic carbon content: Structural changes during heating. Carbon, 105, 572-585.

[39] Ruiz-Rosas, R., Bedia, J., Lallave, M., Loscertales, I. G., Barrero, A., Rodríguez-Mirasol, J., et al. (2010). The production of submicron diameter carbon fibers by the electrospinning of lignin. Carbon, 48(3), 696-705.

[40] Li, X., Chen, Y., Huang, H., Mai, Y., & Zhou, L. (2016). Electrospun carbon-based nanostructured electrodes for advanced energy storage – A review. Energy Storage Materials, 5, 58-92.

[41] Ma, X., Kolla, P., Zhao, Y., Smirnova, A. L., & Fong, H. (2016). Electrospun lignin-derived carbon nanofiber mats surface-decorated with MnO2 nanowhiskers as binder-free supercapacitor electrodes with high performance. Journal of Power Sources, 325, 541-548.

[42] Salinas-Torres, D., Ruiz-Rosas, R., Valero-Romero, M. J., Rodríguez- Mirasol, J., Cordero, T., Morallón, E., et al. (2016). Asymmetric capacitors using lignin-based hierarchical porous carbons. Journal of Power Sources, 326, 641-651.

[43] He, Y., Wang, L., & Jia, D. (2016). Coal/PAN interconnected carbon nanofibers with excellent energy storage performance and electrical conductivity. Electrochimica Acta, 194, 239-245.

[44] Wang, G., Dong, Q., Wu, T., Zhan, F., Zhou, M., & Qiu, J. (2016). Ultrasound-assisted preparation of electrospun carbon fiber/graphene electrodes for capacitive deionization: Importance and unique role of electrical conductivity. Carbon, 103, 311-317.

[45] Shilpa, Das, S. K., Afzal, M. A. F., Srivastava, S., Patil, S., & Sharma, A. (2016). Enhanced electrical conductivity of suspended carbon nanofibers: Effect of hollow structure and improved graphitization. Carbon, 108, 135-145.

[46] Dallmeyer, I., Lin, L. T., Li, Y., Ko, F., & Kadla, J. F. (2014). Preparation and characterization of interconnected, kraft lignin-based carbon fibrous materials by electrospinning. Macromolecular Materials and Engineering, 299(5), 540-551.

[47] Wang, Y., Serrano, S. & Santiago-Aviles, J.J. Journal of Materials Science Letters (2002) 21: 1055. doi:10.1023/A:1016081212346

[48] Imaizumi, S., Matsumoto, H., Suzuki, K., Minagawa, M., Kimura, M., & Tanioka, A. (2009). Phenolic resin-based carbon thin fibers prepared by electrospinning: Additive effects of poly(vinyl butyral) and electrolytes. Polymer Journal, 41(12), 1124-1128.

[49] Cremar, L. D., Acosta-Martinez, J., Villarreal, A., Salinas, A., & Lozano, K. (2016). Mechanical and electrical characterization of carbon nanofibers produced from water soluble precursors. Materials Today Communications, 7, 134-139.

[50] Dongxin HE,Chengguo WANG,Yujun BAI et al. Comparison of Structure and Properties among Various PAN Fibers for Carbon Fibers. J. Mater. Sci. Technol., 2005, 21(03): 376-380 .

[51] Bokhonov, Boris B., Dina V. Dudina, Arina V. Ukhina, Michail A. Korchagin, Natalia V. Bulina, Vyacheslav I. Mali, and Alexander G. Anisimov. 2015. Formation of self-supporting porous graphite structures by spark plasma sintering of nickel–amorphous carbon mixtures. Journal of Physics and Chemistry of Solids 76 (1): 192-202.

[52] Poursorkhabi, Vida, Amar K. Mohanty, and Manjusri Misra. 2016. Statistical analysis of the effects of carbonization parameters on the structure of carbonized electrospun organosolv lignin fibers. Journal of Applied Polymer Science 133 (45).

CHAPTER 4

POROUS CARBON THROUGH PCFA/PEO BASED CARBON FIBERS USING GREEN SOLVENT

4.1 Introduction

The use of carbon based materials in a battery system is linked to their high electrical conductivity and good corrosion resistance in different electrolytes [1]. Various techniques had been employed to manufacture carbon nanofibers with diameters under 200 nm to achieved higher electrical conductivity that can act as an electrode or as supporting material for electrode [2] and utilized for EMI and RFI shielding applications [3]. Moreover, the Nano porous structure of carbon fibers helps for energy storage applications [4]. However, the cost and high carbon footprint during the manufacturing of the carbon fibers are the source of major concern for industry and environmental governing bodies [5]. Significant effects have been made to lower the cost of the carbon fibers by using alternative biological precursors (lignin) [6]. Due to heterogeneity of lignin quality and lower molecular weight, it's widely used by blending it with high molecular weight polymer to improve spinning capability [7]. Poly(ethylene oxide) (PEO) is one such high molecular synthetic polymer. Incorporation of low concentration of PEO in hardwood Kraft lignin has been shown to enhance spinning capability and fiber handling during processing [8]. Thermal analysis showed a single glass transition for a Kraft lignin/PEO blend indicating the miscibility of the two [9]. Strong hydrogen bonding also aids in spinning of fibers and resulted in miscible blending of Organosolv lignin/PEO [10]. Addition of PEO in kraft lignin solution results in an ordered and directed assembly that inhibits formation of defects during the carbon fiber

manufacturing [11]. In this chapter, low concentrations of PEO and Poly caffeyl-alcohol (PCFA) lignin were electrospun into precursor carbon fiber, which was followed by a thermal stabilization step. Thermally stabilized fibers were carbonized at different parameters. The amount of energy used during the carbonization step is a major source of concern due to the high temperature process in carbon fiber manufacturing. Statistical analysis using design of experiment (DOE) approach was used for the optimization of carbonization step.

We use the design of mixture approach which was first introduced in 1935 by Ronald A. Fisher [12]. This signifies the effect of different variables individually as well as their collaborative effect on the performance of the product [13]. The benefits related to the DOE approach are widely recognized as they remove the ‘confounding of effects’. Confounding of effects means a single effect is associated with multiple causes, which makes it difficult to separate among various factors. DOE identifies the significant variables that need to be controlled, as well as finds insignificant variables [14]. These characteristics have made DOE a major contributor to the multiple quality assurance strategies, such as Six Sigma, lean manufacturing, ISO 9000 [15,16].

The statistical principle behind DOE is based on the concept of a process model similar to the `black box' type, where several discrete or continuous input (factors) that can be controlled goes in to the black box, it processes the information and gives one or more measured output (responses). The output (responses) are assumed continuous. These inputs and outputs are linked by an empirical (approximation) models based on the experimental data. These empirical model can be on linear or quadratic form. A

generic linear model, where the dependent variable y is to be related to more than one independent variable, say, X1, X2, . . . , Xn can be written as:

$$\boldsymbol{Y} = \beta 0 + \sum_{i=1}^{n} \beta \mathrm{i} \mathrm{X} \mathrm{i} \sum_{i=1}^{n} . \sum_{j=1}^{n} \beta \mathrm{ij} \mathrm{X} \mathrm{i} \mathrm{X} \mathrm{j} \sum_{i=1}^{n} . \sum_{j=1}^{n} . \sum_{k=1}^{n} \beta \mathrm{ijk} \mathrm{X} \mathrm{i} \mathrm{X} \mathrm{j} \mathrm{X} \mathrm{k} + \cdots + \text{experimental error}$$

Where:

β_0 = the overall mean response,

β_i = the main effect for factor (i = 1, 2, ... , n),

β_{ij} = the two-way interaction between the ith and jth factors, and

β_{ijk} = the three-way interaction between the ith, jth, and kth factors.

The DOE approach can be applied for comparison, characterizing, modeling or optimization of an experiment. In this study we use the design of experiment technique to observe the effect of carbonization parameters i.e. carbonization temperature, isothermal time and ramp rate on the electrical conductivity and physical morphology of the PCFA/PEO based carbon fibers. This statistical based DOE technique will result in determining the effect of processing variables on the physical morphology and electrical conductivity of the fiber mesh.

4.2 Experimental

4.2.1 Materials

PEO having average molecular weight of 400,000 and 50% NaOH solution was obtained from Sigma Aldrich and was used without further purification. PCFA was extracted by grounding the seed coats of V. planifolia. To isolate PCFA, seeds were mixed with 1% NaOH in a liquid to solid ratio of 10. The mixture was heated and maintained at 120 ^{0}C for 1 h in an autoclave. The black liquid was separated from residue by filtration. PCFA was precipitated by adjusting the pH to 3.0 with concentrated

HCl. The precipitated PCFA was separated by centrifugation, washed with water and freeze dried.

4.2.2 Electrospinning

Two separate solutions of 10 wt% of PEO in deionized water and 10% wt% of PCFA in 0.5M NaOH solvents were mixed using magnetic stirrer at 50 °C for 4h. During the initial investigation PCFA/PEO were mixed in three different concentrations 97/3, 95/5 and 90/10 by weight for electrospinning. However 97/3 PCFA/PEO solution results in spraying rather than spinning. This can be due to no entanglement of the polymer chains required for electrospinning. The 95/5 and 90/10 PCFA/PEO solutions gave uniform fibers. Higher PEO content in 90/10 samples results in fusing of fibers during the stabilization process [17]. Therefore, 95/5 PCFA/PEO fibers were selected to study the effect of carbonization parameters on the performance of the carbon fibers. The solutions were spun at room temperature. Flow rate was adjusted to have a continuous flow i.e. any drop of solution wiped from the tip is immediately replaced by another. A voltage of 20kV was applied to the tip of the needle using a high voltage power supply (Model #ES30P-5W/DAM, Gamma High Voltage Research Inc., Ormond Beach, FL). A Taylor's cone was observed at the tip of the needle that was attracted by the electrostatic force towards the grounded collector. The distance between the needle and collector was around 20 cm to have a uniform stream from the tip.

4.2.3 Carbonization

The thermal stabilization of the fiber mesh was performed from room temperature to 260 ^{0}C at a heating rate of 0.5 ^{0}C min^{-1}. The fibers were held at that temperature for 60 min in an air force convection laboratory oven by cascade TEK. The stabilized fibers were then carbonized under a nitrogen flow at 0.5 standard cubic feet per hour (SCFH) in Carbolite HZS 12/600 horizontal tube furnace.

4.2.4 Design of Experiment

A two-level factorial design of experiments was applied using NIST data analysis software system: dataplot [18]. Three major carbonization parameters were included i.e. carbonization temperature, isothermal time and the heating rate [19] at two different levels (low and high) for the design of experiments as presented in Table 4-1.

Table 4-1. Two level of factors studied by design of experiments.

Factor	**Symbol**	**Low Level**	**High Level**
Carbonization Temperature	X1	800°C	1000 °C
Isothermal Time	X2	45min	2 h
Heating Rate	X3	5°C/min	10 °C/min

Selection of factors were made in accordance with the principles of DOE i.e. to include all important factors, selecting low and high levels based on industrial rationale, attest the factors for impractical combinations and the response of test not to be used as an input to subsequent test [20,21]. Table 4-2 represent design of experiments having standard layout of high level represented by +1 and low level represented by -1 for each factor and their corresponding values. Carbonization temperature levels were

selected as 800 ^{0}C and 1000 ^{0}C, the lower limit was selected based on the minimum temperature limit to carbonized the lignin, while the higher limit was selected at 1000 ^{0}C [22], moreover, as the carbonization temperature reaches 1100 ^{0}C the graphitization starts. Isothermal time and heating rate range was selected based on lower and higher limit of mostly reported literature values [23].

Table 4-2. Description of an experiment using 8 trials conducted with each factor set to two levels.

	Factors					
	Coded Values			Real Values		
Test	Heating Rate (X1)	Isothermal Time (X2)	Carbonization Temperature (X3)	Heating Rate (°C/min)	Isothermal Time(h)	Carbonization Temperature (°C)
1	-1	-1	-1	5	0.75	800
2	+1	-1	-1	10	0.75	800
3	-1	+1	-1	5	2	800
4	+1	+1	-1	10	2	800
5	-1	-1	+1	5	0.75	1000
6	+1	-1	+1	10	0.75	1000
7	-1	+1	+1	5	2	1000
8	+1	+1	+1	10	2	1000

4.2.5 Scanning Electron Microscopy (SEM)

The FEI Nova 200 NanoLab having an ultra-high resolution field emission scanning electron microscope (SEM) (FEI Company, Oregon, USA) was used to image the stabilized and carbonized electrospun PAN/PCFA fibers at an accelerating voltage of 15 kV at 5 mm working distance. The samples were sputter coated with gold-palladium to make them conductive and make imaging possible.

4.2.6 Electrical Conductivity

The conductivity of PCFA and PEO blended carbon fibers was measured using a multimeter (Agilent 34401A) equipped with a two-point probe, as described in the

literature [24]. Samples of fiber mat having dimensions of 15 mm in length and 5 mm in width were used. Silver paint was applied at the end of the fiber mesh to have a uniform conductive contact. The electrical conductivity (κ) was calculated using equation 1.

$$\kappa\ (S\ cm^{-1}) = \frac{L}{wtR} \qquad (1)$$

where L is the distance between the probes(cm), w is the width of the sample (cm), and t is the thickness of the sample (cm).

4.3 Results

4.3.1 SEM

SEM images of carbonized PCFA/PEO fibers manufactured at different processing parameters are shown in Figure 4-1. Numbering of the images corresponds to the description of parameters mentioned in Table 4-2. Average diameters for the eight carbonized samples was between 161 ± 21 nm for sample 7 and 232 ± 67 nm for sample 6. It's been reported that fiber diameters spun from aqueous solutions have large diameters as compared to organic solvents [25], However we are able to get fibers in between 160 to 230 nm. This can be due to linear nature of the PCFA lignin. We observed fusion of fibers and also the largest diameters for Sample 6 and 8, which led us to conclude that fusion of fibers occurred when we had both high carbonization temperature and high heating rate. Apart from these two, all samples preserved their structure without major fusion. From Figure 4-1, we can see that a sample carbonized at 800 ^{0}C (1, 2, 3 and 4) had a rough surface as compared to the ones carbonized at higher temperature. This can be due to the impurities and inorganic material from the sodium hydroxide solvent. Porosity was developed in the fibers during the

carbonization, without any additional activation step, which can be due to high oxygen content in lignin [4]. These porous structure helps in diffusion and accessibility of ions advantageous for energy storage applications [26]. Successful formation which were observed for samples having high heating rate and high carbonization temperature.

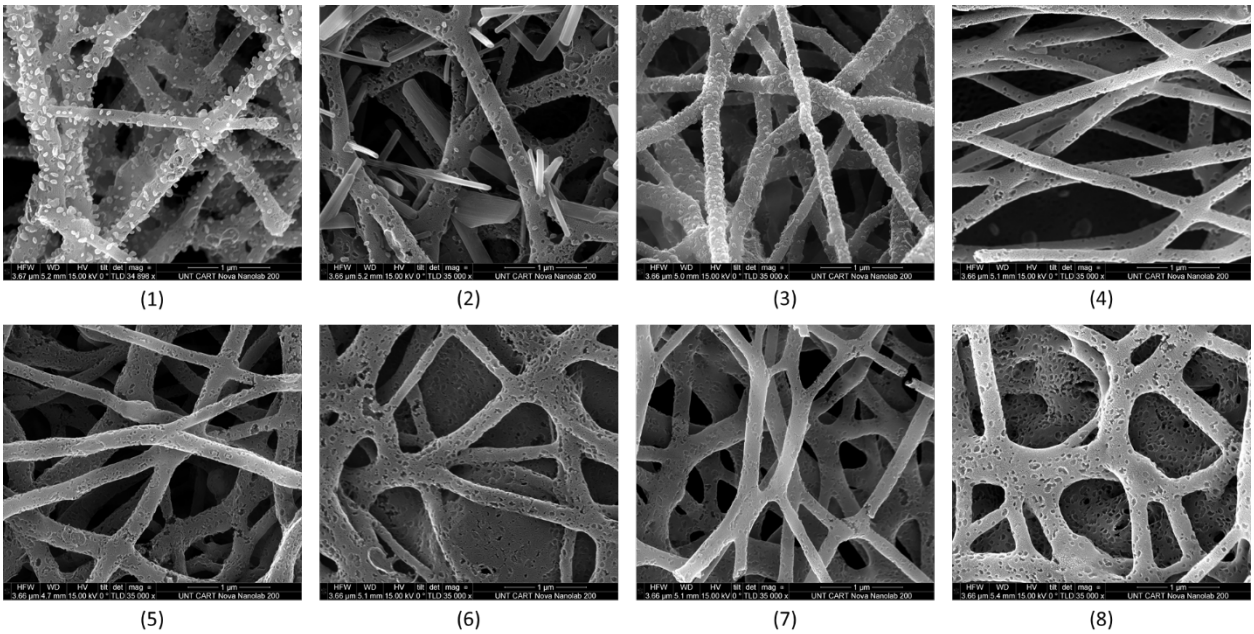

Figure 4-1. SEM images shows the varying morphology of carbonized fibers at different conditions. Numbers corresponds to the sample number mentioned in Table 4-2.

Effect of heating rate, isothermal time and carbonization temperature on the diameter of the fibers were analysed based on two factorial design of experiment approach using NIST statistical software data plots. Figure 4-2 shows the effect of individual factors on the diameter of the carbonized fibers. Heating rate had the most significant (direct) effect on the diameter of the fiber i.e. the diameter of the fibers increases with the heating rate. The next major variable that affect the diameter is isothermal time. It is inversely related to the diameter of the fibers, while carbonization temperature is a nonsignificant factor.

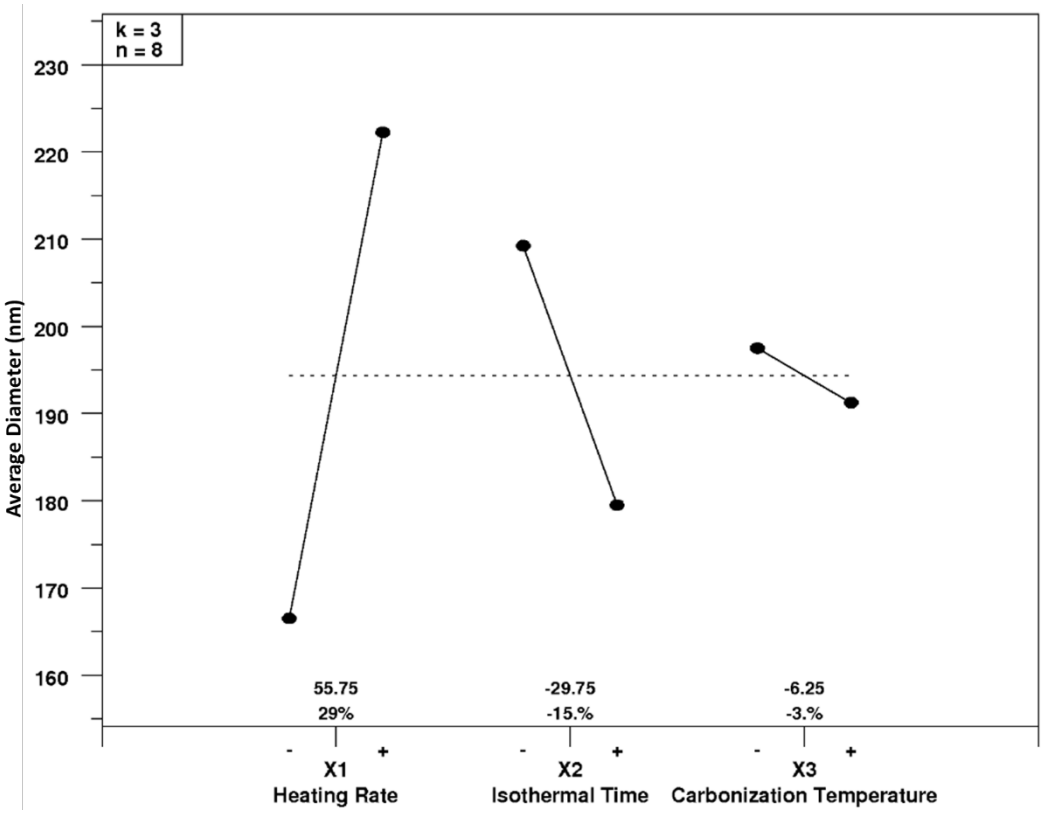

Figure 4-2. Factors effecting the diameter of carbonized fibers.

Figure 4-3 shows the interaction effect of the factors on the diameter of the carbonized fiber. It can be observed that even though heating rate has a direct relation i.e. the diameter increase with the increases in the rate, when it is combined with the isothermal time the diameter decreases significantly and time and heating rate have the highest interaction between the parameters.

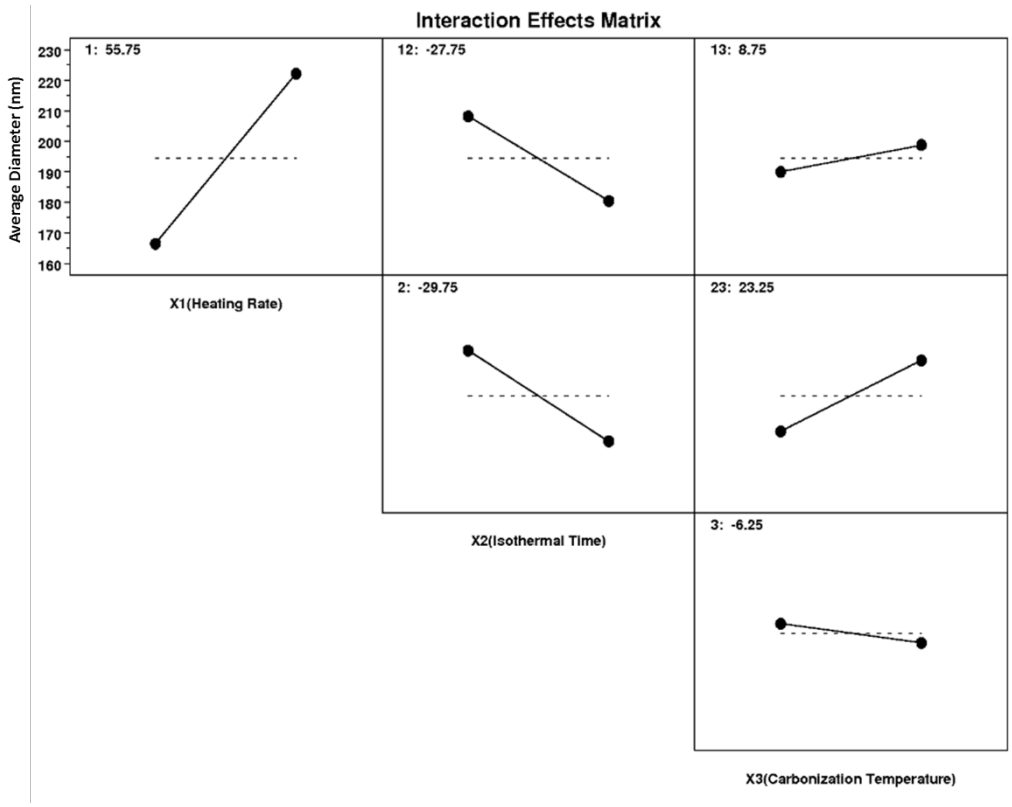

Figure 4-3. Interaction effect of factors on the diameter of carbonized fibers.

4.3.2 Electrical Conductivity

Electrospun carbon nanofibers due to their high surface area, porous structure and conductive behavior become a strong contender as an electrode in energy storage devices such as rechargeable batteries and supercapacitors [27-31]. Physical morphology of the nanofiber [32], inter-fiber bonding [33] as wells as the carbonization parameters [34] affect the conductivity of the electrospun mesh. Table 6-3 lists the conductivity values for samples at various processing conditions using the design of experiment approach as shown in Table 4-3.

Table 4-3. Electrical conductivity of carbonized fibers.

Sample	κ (S cm^{-1})
1	3.52 ± 0.01
2	3.15 ± 0.01
3	3.78 ± 0.01
4	3.32 ± 0.01
5	6.17 ± 0.14
6	4.40 ± 0.02
7	7.21 ± 0.01
8	6.59 ± 0.01

The conductivity of PCFA and PEO blend is comparable to the reported conductivity of electrospun carbon fibers derived from polyacrylonitrile (PAN) carbonized at 800 °C ($\kappa = 4.88$ S cm−1) [35], and at higher temperature to lignin-g-polyacrylonitrile copolymer carbonized at 1000 °C ($\kappa = 7.10$ S cm−1) [31]. The increase in conductivity at higher temperature can be due to the presence of more ordered graphitic structure [36].

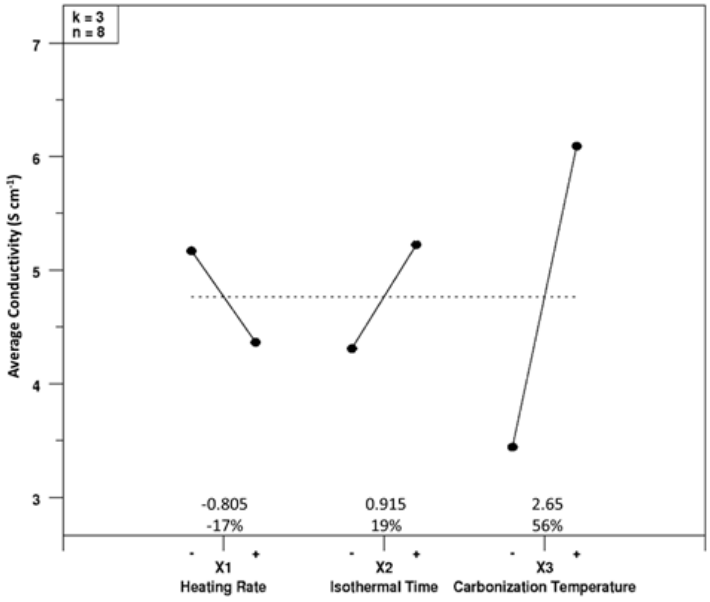

Figure 4-4. Factors effecting the electrical conductivity of carbonized fiber mesh.

Two level factorial design of experiment of the carbonization parameters was performed to find the significant factor affecting the conductivity. Statistical analysis shows the conductivity is mainly influenced by the carbonization temperature. Figure 4-4 shows the effect of individual factors, the positive slope for isothermal time and carbonization temperature shows a directly proportional relation to the conductivity. The height of the bar indicates the degree of influence. As seen from Figure 4-4, carbonization temperature had a higher influence than other factors. For heating rate a negative slope shows an inverse relation meaning with the increase of heating rate the conductivity of mesh decreases.

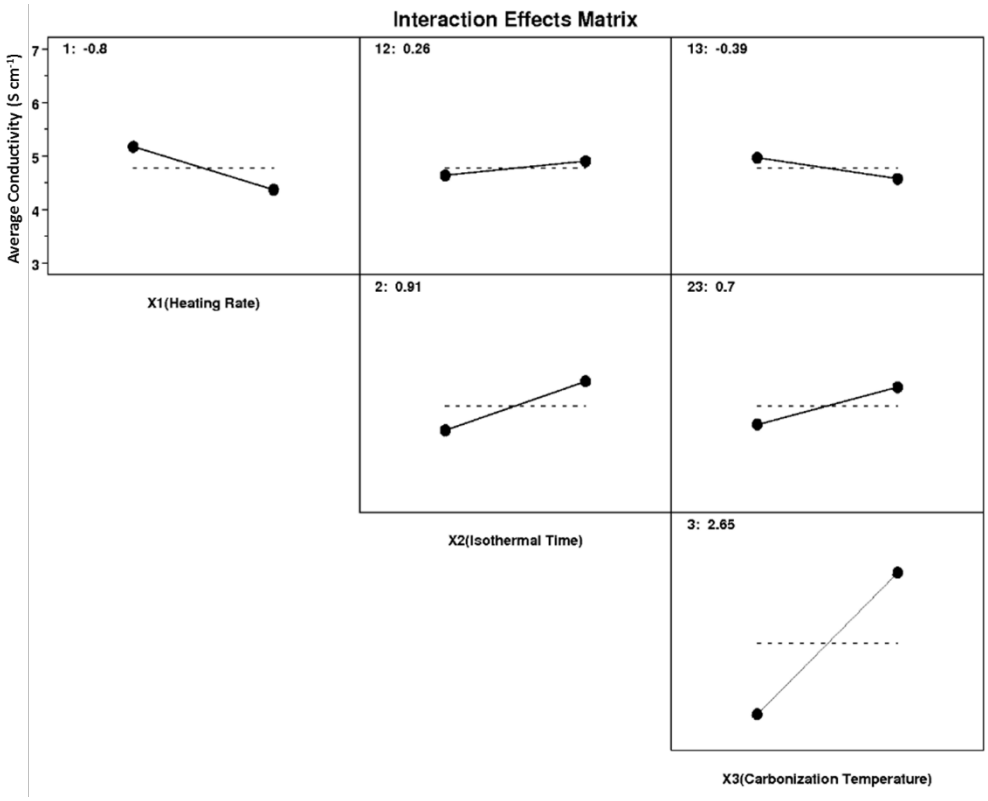

Figure 4-5. Interaction effect of factors on the conductivity of the carbonized fiber mesh.

Figure 4-5 shows the interaction effect matrix for the carbonization parameter on the conductivity of the fiber mesh. All of the interaction factors are close to horizontal

line response meaning the interaction has no significant effect on the conductivity and carbonization temperature alone is the significant factor.

4.4 Conclusions:

Poly caffeyl alcohol (PCFA) lignin blend with 5% weight ratio Poly ethylene oxide (PEO) where successfully electrospun in a mixture of aqueous sodium hydroxide solution. Low molecular weight and linear structure of lignin results in carbonized fibers having diameter in between 160 to 230 nm. Porosity was achieved in fibers without the activation step due to high content of oxygen, which helps in diffusion and accessibility of ions advantageous for energy storage applications. Effect of carbonization parameters (heating rate, isothermal time and carbonization temperature) on fiber morphology and conductivity of carbonized mesh were statistically analyzed by two-level factorial design of experiments. Results showed that the heating rate is the most significant factor and is inversely related to the diameter of the fiber, whereas the conductivity of the fiber mesh is significantly controlled by the carbonization temperature.

4.5 References

[1] Endo, M., Kim, Y. A., Hayashi, T., Nishimura, K., Matusita, T., Miyashita, K., et al. (2001). Vapor-grown carbon fibers (VGCFs): Basic properties and their battery applications. *Carbon, 39*(9), 1287-1297.

[2] Tibbetts, G. G., Lake, M. L., Strong, K. L., & Rice, B. P. (2007). A review of the fabrication and properties of vapor-grown carbon nanofiber/polymer composites. *Composites Science and Technology, 67*(7–8), 1709-1718.

[3] Al-Saleh, M. H., & Sundararaj, U. (2009). A review of vapor grown carbon nanofiber/polymer conductive composites. *Carbon, 47*(1), 2-22.

[4] Berenguer, R., Garcia-Mateos, F., Ruiz-Rosas, R., Cazorla-Amoros, D., Morallon, E., Rodriguez-Mirasol, J., et al. (2016). Biomass-derived binderless fibrous carbon electrodes for ultrafast energy storage. *Green Chemistry, 18*(6), 1506-1515.

[5] S. M. Batouli , Y. Zhu, M. Nar and N. A. D'Souza, Environmental Performance of Kenaf-fiber Reinforced Polyurethane: a Life Cycle Assessment Approach, Building and Environment, Journal of Cleaner Production 66 (2014) 164-173

[6] Mainka, H., Täger, O., Körner, E., Hilfert, L., Busse, S., Edelmann, F. T., et al. (2015). Lignin – an alternative precursor for sustainable and cost-effective automotive carbon fiber. Journal of Materials Research and Technology, 4(3), 283-296.

[7] Kadla, J.F., Kubo, s., Gilbert, R.D., Venditti, R.A., Compere, A.L., Griffith, W.L.Lignin-based carbon fibers for composite fiber applications, Carbon 40 (2002) 2913–2920

[8] Kubo, S. and Kadla, J. F. (2005), Kraft lignin/poly(ethylene oxide) blends: Effect of lignin structure on miscibility and hydrogen bonding. J. Appl. Polym. Sci., 98: 1437–1444.

[9] Kadla, J. F.; Kubo, S.; Venditti, R.; Gilbert, R. Lignin-Based Carbon Fibers for Composite Fiber Applications. Carbon 2002, 40, 2913−2920.

[10] Satoshi Kubo and and John F. Kadla, Poly(Ethylene Oxide)/Organosolv Lignin Blends: Relationship between Thermal Properties, Chemical Structure, and Blend Behavior, Macromolecules 2004, 37, 6904-6911.

[11] Imel, A. E., Naskar, A. K., & Dadmun, M. D. (2016). Understanding the impact of poly(ethylene oxide) on the assembly of lignin in solution toward improved carbon fiber production. *ACS Applied Materials & Interfaces, 8*(5), 3200-3207.

[12] S. R. A. Fisher, R. A. Fisher, S. Genetiker, "The design of experiments," Oliver and Boyd ltd,(Vol. 12, No. 6). Edinburgh, 1960.

[13] Langsrud, Øyvind. 2001. Identifying significant effects in fractional factorial multiresponse experiments. *Technometrics* 43 (4): 415-24.

[14] G. E. Box, W. G. Hunter and J. S. Hunter, "Statistics for Experimenters," 1st Edition, Canada, John Wiley and Sons, Inc., p. 291–334, 1978.

[15] Genichi, Taguchi, "Introduction to Quality Engineering - Designing Quality into Products," Asian Productivity Organization, 1986.

[16] D. C. Montgomery, "Design and analysis of experiments," 8th edition, USA, John Wiley & Sons, 2012.

[17] Oroumei, A., Fox, B., & Naebe, M. (2015). Thermal and rheological characteristics of biobased carbon fiber precursor derived from low molecular weight organosolv lignin. *ACS Sustainable Chemistry & Engineering, 3*(4), 758-769.

[18] J. J. Filliben, "Dataplot - an interactive high-level language for graphics, non-linear fitting, data analysis, and mathematics," in ACM SIGGRAPH Computer Graphics, pp. 199-213, Aug. 1981

[19] Poursorkhabi, V., Mohanty, A. K., & Misra, M. (2016). Statistical analysis of the effects of carbonization parameters on the structure of carbonized electrospun organosolv lignin fibers. *Journal of Applied Polymer Science, 133*(45).

[20] T. Lundstedt, E. Seifert, L. Abramo, B. Thelin, Å. Nyström, J. Pettersen and R. Bergman, "Experimental design and optimization," Chemometrics and intelligent laboratory systems, vol. 42, no. 1, pp. 3-40, Aug. 1998.

[21] P. W. Araujo and R.G. Brereton, "Experimental design II. Optimization," TrAC Trends in Analytical Chemistry, vol. 15, no. 2, pp. 63-70, Feb.1996.

[22] Dallmeyer, I., Lin, L. T., Li, Y., Ko, F., & Kadla, J. F. (2014). Preparation and characterization of interconnected, kraft lignin-based carbon fibrous materials by electrospinning. *Macromolecular Materials and Engineering, 299*(5), 540-551.

[23] Berenguer, R., Garcia-Mateos, F., Ruiz-Rosas, R., Cazorla-Amoros, D., Morallon, E., Rodriguez-Mirasol, J., et al. (2016). Biomass-derived binderless fibrous carbon electrodes for ultrafast energy storage. *Green Chemistry, 18*(6), 1506-1515.

[24] Youe, W., Lee, S., Lee, S., Lee, S., & Kim, Y. S. (2016). Characterization of carbon nanofiber mats produced from electrospun lignin-g-polyacrylonitrile copolymer. International Journal of Biological Macromolecules, 82, 497-504.

[25] Poursorkhabi, V., Mohanty, A. K., & Misra, M. (2015). Electrospinning of aqueous lignin/poly(ethylene oxide) complexes. *Journal of Applied Polymer Science, 132*(2).

[26] A. Linares-Solano and D. Cazorla-Amorós, Activated Carbon Fibers, in Handbook of Advanced Ceramics, ed. S. Somiya, Academic Press, Elsevier Inc., 2013, p. 155.

[27] Li, X., Chen, Y., Huang, H., Mai, Y., & Zhou, L. (2016). Electrospun carbon-based nanostructured electrodes for advanced energy storage – A review. Energy Storage Materials, 5, 58-92.

[28] Ma, X., Kolla, P., Zhao, Y., Smirnova, A. L., & Fong, H. (2016). Electrospun lignin-derived carbon nanofiber mats surface-decorated with MnO2 nanowhiskers

as binder-free supercapacitor electrodes with high performance. Journal of Power Sources, 325, 541-548.

[29] Salinas-Torres, D., Ruiz-Rosas, R., Valero-Romero, M. J., Rodríguez- Mirasol, J., Cordero, T., Morallón, E., et al. (2016). Asymmetric capacitors using lignin-based hierarchical porous carbons. Journal of Power Sources, 326, 641-651.

[30] He, Y., Wang, L., & Jia, D. (2016). Coal/PAN interconnected carbon nanofibers with excellent energy storage performance and electrical conductivity. Electrochimica Acta, 194, 239-245.

[31] Wang, G., Dong, Q., Wu, T., Zhan, F., Zhou, M., & Qiu, J. (2016). Ultrasound-assisted preparation of electrospun carbon fiber/graphene electrodes for capacitive deionization: Importance and unique role of electrical conductivity. Carbon, 103, 311-317.

[32] Shilpa, Das, S. K., Afzal, M. A. F., Srivastava, S., Patil, S., & Sharma, A. (2016). Enhanced electrical conductivity of suspended carbon nanofibers: Effect of hollow structure and improved graphitization. Carbon, 108, 135-145.

[33] Dallmeyer, I., Lin, L. T., Li, Y., Ko, F., & Kadla, J. F. (2014). Preparation and characterization of interconnected, kraft lignin-based carbon fibrous materials by electrospinning. Macromolecular Materials and Engineering, 299(5), 540-551.

[34] Youe, W., Lee, S., Lee, S., Lee, S., & Kim, Y. S. (2016). Characterization of carbon nanofiber mats produced from electrospun lignin-g-polyacrylonitrile copolymer. International Journal of Biological Macromolecules, 82, 497-504.

[35] Wang, Y., Serrano, S. & Santiago-Aviles, J.J. Journal of Materials Science Letters (2002) 21: 1055.

[36] Cremar, L. D., Acosta-Martinez, J., Villarreal, A., Salinas, A., & Lozano, K. (2016). Mechanical and electrical characterization of carbon nanofibers produced from water soluble precursors. Materials Today Communications, 7, 134-139.

CHAPTER 5

FABRICATION OF BIOINSPIRED CELLULAR SHEATH-CORE ELECTROSPUN NON-WOVEN MESH[2]

5.1 Introduction:

We have examined the architecture and chemical constituents in plant fibers from the growth to the dried (retted state) [1]. The results show that porosity in the core is intrinsic to plant fibers due to the vascular system for transporting nutrients [2]. The core and surface porosity introduced through processing from harvested to dried state impacts composite and fiber performance [3,4]. The results provide a new landscape for fiber and mesh design that utilizes surface (sheath) and core porosity to engineer new properties. Applications of textiles are widespread with an increasing value for sensing, environmental decontamination, biomedical drug delivery and tissue scaffolds.

Fibers generated from coaxial electrospinning is a cost-effective and efficient method to generate high surface area, three-dimensional meshes of fibers having core-sheath architecture. This gives them the ability to isolate and separate nanoparticles in unfriendly environments and to enhance the mechanical properties of the composite. For example in biomedical application, ability to encapsulate proteins, antibodies and various drugs protecting them from the natural immune system of the body is enabled. This makes them preferable drug delivery vehicles for prolonged and controlled release. Different combinations of core-shell fibers have been studied such as PEO/PSU, PCL/Gelatin, PP/PLLA, PVP/PLA [5,6] to create a scaffold for the growth of biological

[2] This entire chapter is reproduced from Hussain R Rizvi, Nandika D'Souza "Fabrication of Bioinspired Cellular Sheath-Core Electrospun Non-Woven Mesh" ASME Journal of Micro- and Nano-Manufacturing 2017, Manuscript under review.

cells on one polymer while the other polymer provides mechanical stability to the structure can be envisioned [7]. However, the fiber cross-sectional architecture has been an underexplored variable. Porosity helps a fiber to increase surface area with a small footprint. Surface porosity has positive impact on cell adhesion, proliferation and differentiation in biomedical scaffolds. Core porosity also benefits in mass transport [8].

The electrospinning method works on the principle of electrostatic charge difference between the tip of a needle and a collector resulting in the polymer solution being subjected to high voltage which induced a polarity causing it to attracted to the opposite polarity charge. Fiber morphology is controlled by the voltage difference [9], type of solvent [10], relative humidity [11], flow rate & surface tension and viscosity of the solution [12].

In order to utilize the benefits of cellular structure such as high strength to weight ratio [13] and transport of fluids, various methods have been used to achieve porosity of fibers including subcritical CO_2 foaming of PCL electrospun fibers [14], or by directly spinning into the CO_2 environment for PVP and PVDF polymers [15]. However, there are still challenges in trying to maintain the physical morphology of fibers. In this chapter, we discuss the manufacturing and characterization of the electrospun coaxial fibers, with the ability to introduce porosity using a solvent free physical foaming technique in either the sheath or core of the coaxial electrospun fibers.

5.2 Nomenclature

Foamed PCL(PBAT)	CO_2 foamed coaxial fiber having PBAT as a core and PCL as sheath.
PCL(PBAT)	Coaxial fiber having PBAT as a core and PCL as sheath.
Foamed PBAT(PCL)	CO_2 foamed coaxial fiber having PCL as a core and PBAT as sheath.
PBAT(PCL)	Coaxial fiber having PCL as a core and PBAT as sheath.

5.3 Experimental

5.3.1 Materials

Poly(butyrate adipate terephthalate)(PBAT) Ecoflex® F BX 7011 (MW 40kDa, BASF Germany) and Poly (ε-caprolactone) (PCL) (MW 50 kDa, Union Carbide Corporation) were used as received. Chloroform containing amylenes as a stabilizer, ACS reagent with 99.8% purity and acetone purchased from Sigma-Aldrich were used as a solvent for the electrospinning process. All chemicals were used without further purification.

5.3.2 Preparation of Electrospun Fibers

Two separate solutions were prepared by dissolving 10% by wt. of PBAT and 30% by wt. of PCL in chloroform at 40 ^{0}C for one hour. After the solution was prepared 10% by vol. acetone was added to increase the electrical conductivity of the solution. To get coaxial fiber meshes, a customized T- shaped needle having an outer diameter of 0.038 inches and an inner diameter of 0.019 inches from VITA Needle Company was used. The flow rate was maintained at 0.03ml min^{-1} with the help of a syringe pump by New era Pump Systems, Inc. to have a continuous flow of polymer solution. The electrical voltage was increased gradually to a critical value of 9 kV to have a uniform stream of solution from the tip of the needle using a DC Voltage supply (Gamma High Voltage Research). Further increase in voltage cause the separation of the stream into two resulting in separate fibers for PCL and PBAT. Voltage lower than 9 kV results in dripping of the solution. Fibers were collected at a mandrel collector at a distance of 15 cm from the tip of the needle. The collector was grounded to create the voltage

difference between the needle and the collector. Figure 5-1 shows the schematic of fabrication setup.

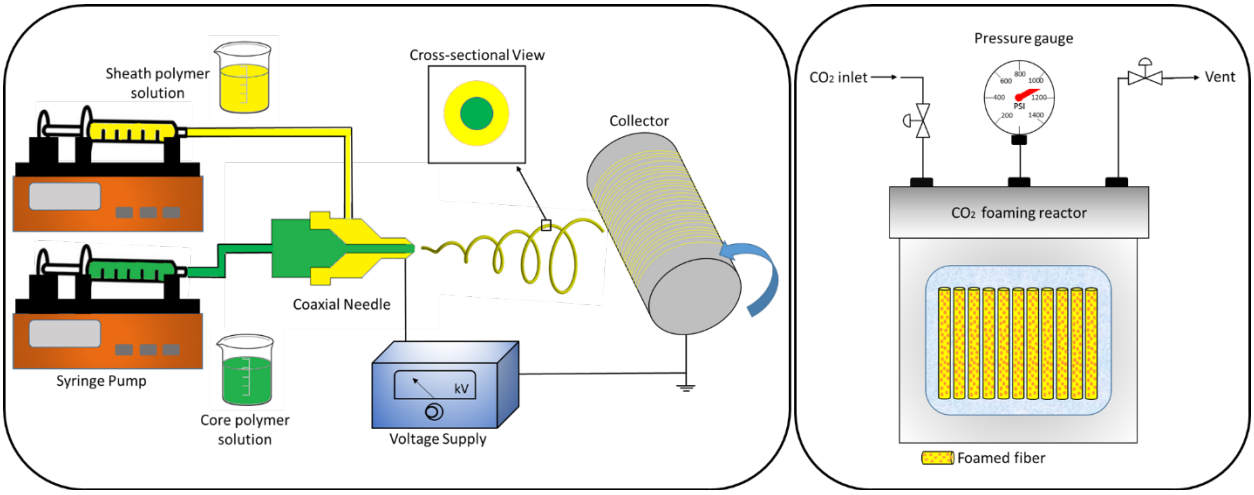

Figure 5-1. Schematic of coaxial electrospining and CO2 foaming rector used for fabrication of porous fibers.

5.3.3 CO_2 Foaming of the Fiber Mesh

The as-spun fiber mesh was exposed to supercritical CO_2 in a customized foaming setup with a controlled temperature chamber. The pressure maintained in the chamber was 1100 psi at the temperature of 32 ^oC. The soaking time for the carbon dioxide to infuse into a CO_2 miscible polymer (PCL) placed in the core and the sheath of the fibers was 30 min. Afterward, the chamber was depressurized rapidly within 10 sec causing the release of CO_2 from the fibers resulting in a porous structure. Higher foaming time causes an increase in the pore diameter which results in braking of fibers.

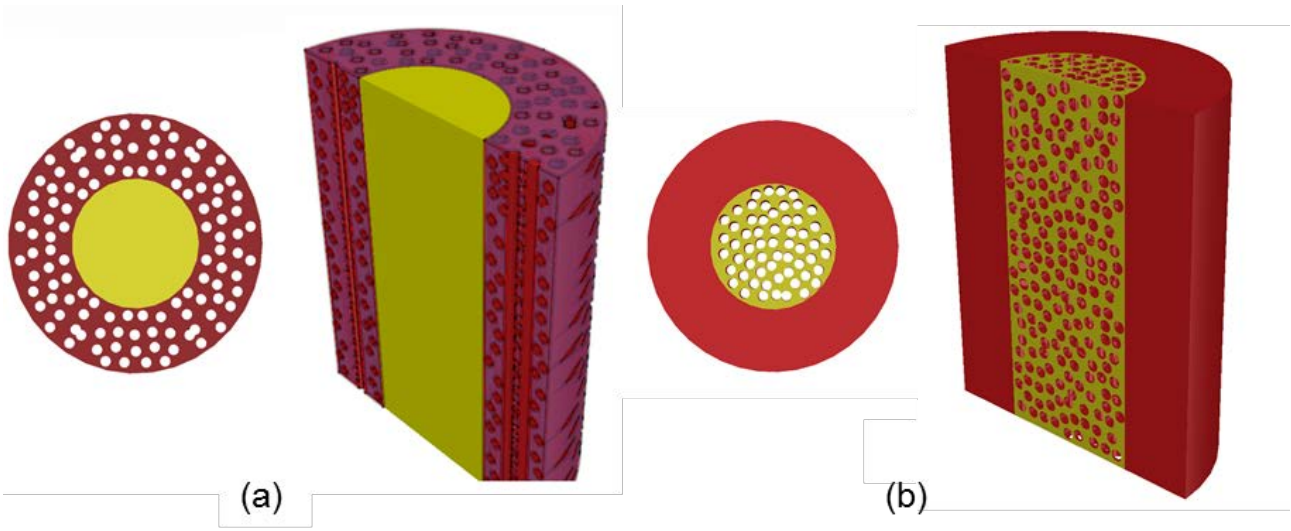

Figure 5-2. Pictorial description of (a) foamed PCL(PBAT) and (b) foamed PBAT(PCL) coaxial fiber.

5.3.4 Characterization of Electrospun Fibers

Surface morphology of fiber mesh and foamed coaxial fibers was observed via SEM system (FEI Nova NanoSEM 230). All of the samples were sputter coated with carbon particles to make them resistive to irradiation by reducing the charge developed on the surface. The coated samples were analyzed at an accelerating voltage of 15 kV at a spot size of 6. The working distance of 5mm was used to capture the images.

5.3.5 Tensile Testing

The tensile properties of aligned fiber mesh and foamed samples were determined using RSA III (TA Instrument, New Castle, DE) in a transient mode using standard extension mode test as reported by Pu et al. [16] The uniaxial fixture was used for the samples cut in a rectangular shape with the dimensions of 15 mm × 10 mm, having a thickness in the range of 0.075 $\pm$ 0.025mm were used. All the samples were tested at a strain rate of 5mm min^{-1}.

5.3.6 Dynamic Mechanical Analysis (DMA)

To measure the viscoelastic properties of the electrospun fibers and foamed sample, DMA was performed using RSA III. Rectangular shaped samples having dimensions of 15 mm × 10 mm with a thickness of 0.075 $\pm$ 0.025mm were used. Initially, the strain amplitude sweep test was performed at 1 Hz to determine the linear viscoelastic region. Next, the samples were scanned using dynamic temperature ramp test from -80 ^{o}C to 40 ^{o}C at the heating rate of 5 ^{o}C min^{-1}. Parameters used were a frequency of 1 Hz and strain amplitude calculated from strain sweep test was set to 0.12%.

5.3.7 Differential Scanning Calorimeter (DSC)

Thermal properties of the electrospun fibers and CO_2 foamed samples were studied using Perkin Elmer DSC6 differential scanning calorimeter, equipped with a Chiller by Perkin-Elmer. Heating scans were performed from 20 ^{o}C to 200 ^{o}C at the rate of 10 ^{o}C per minute to calculate the melting temperature and heat of enthalpy. The samples were held at 200 ^{o}C for 1 minute to stabilize. Next, they were cooled down from 200 ^{o}C to 20 ^{o}C at the rate of 10 ^{o}C to calculate the recrystallization temperature and enthalpy of crystallization. The degree of crystallization of each sample was calculated using enthalpy of heating and the theoretical value of 100% crystalline enthalpy of heating for PCL and PBAT polymer. This result is important as the crystallinity of the fibers hinders degradation and enhances stiffness and tensile strength. This affects the performance of the fiber mesh being used for drug delivery and tissue scaffolding [17].

5.4 Results and Discussion

5.4.1 Scanning Electron Microscope (SEM)

SEM was used to characterize the surface morphology and cross-sectional structure of the CO_2 foamed coaxial fibers. Samples were sputter coated with carbon particles under vacuum before the SEM observation. Figure 5-3 (a) and (b) shows the surface and cross section of the foamed PCL(PBAT) coaxial fiber respectively, as the CO_2 miscible polymer (PCL) was at the skin of coaxial fiber, we observe porous structure at the surface while a solid CO_2 immiscible polymer (PBAT) surrounded by porous structure can be observed from the cross-sectional view as shown in Figure 5-3(b). Figure 5-3(c) and (d) shows the surface and cross section of foamed PBAT(PCL) fibers. As the CO_2 immiscible polymer (PBAT) was at the sheath of the fibers we didn't see any sign of porosity at the surface, whereas the core shows uniform porosity throughout the cross-section (Figure 5-3(d)). Moreover, no physical detachment of the two polymer surface was observed after CO_2 exposure indicating a successful amalgamation of polymers at the boundary of core and sheath.

SEM images were further examined using image processing software ImageJ for pore size (D), cell density (N_0) and linear cell density, using the method described by Kumar et al. [18]. Table 3-1 lists these parameters. Results indicate similar pore (cell) diameter of 0.37 micron irrespective either the pores are in the core or the sheath of the coaxial fibers. However, we observe almost three folds increase in the pore (cell) density for the foamed PCL(PBAT) sample. This increase in the pore (cell) density may be due to the higher expose area resulting in an ease in the release of CO_2 during depressurization.

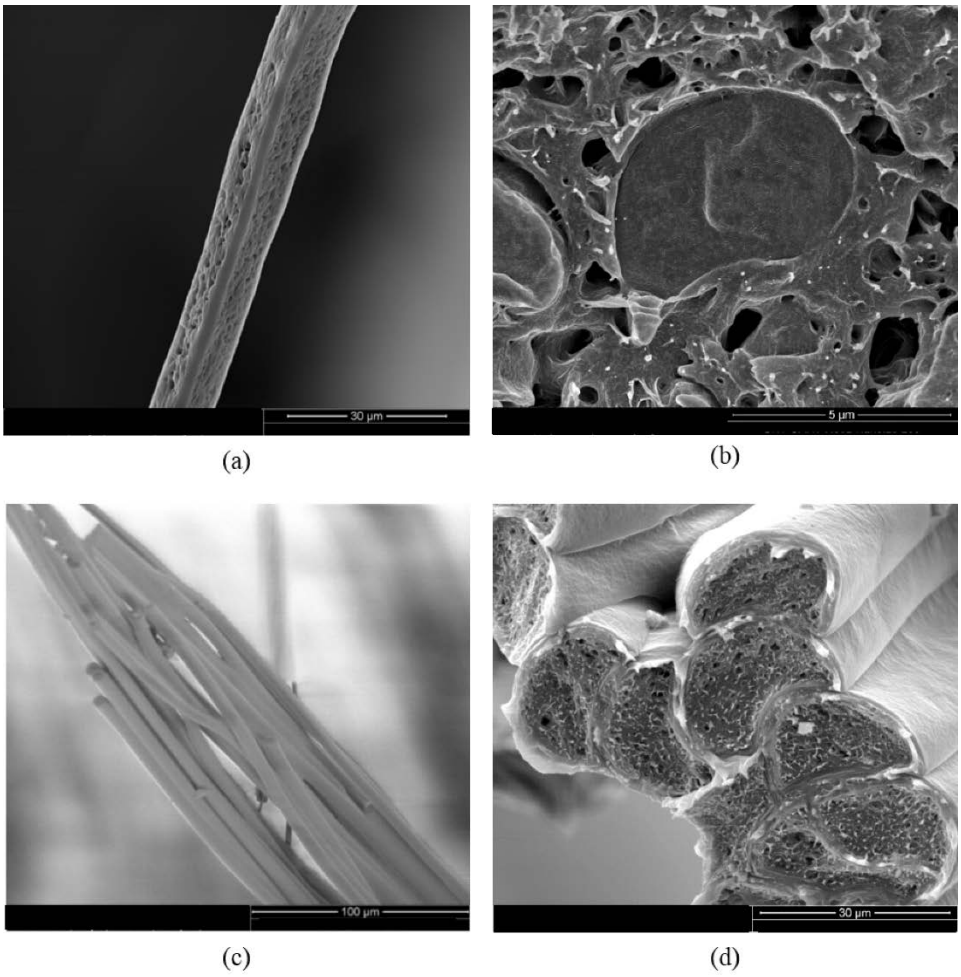

Figure 5-3. SEM images of (a) foamed PCL(PBAT) (b) cross-sectional view of foamed PCL(PBAT) (c) foamed PBAT(PCL) and (d) cross-sectional view of foamed PBAT(PCL) electrospun fibers.

Table 5-1. Pore (cell) density and average cell diameter of the foamed fibers.

	Cell density (N_0) (cells/cm^3)	Linear cell density (cells/cm^2)	Cell diameter (D) (µm)
Foamed PCL(PBAT)	8.57 x 10^{11}	9483 ± 595	0.377 ± 0.24
Foamed PBAT(PCL)	2.68 x 10^{11}	6414 ± 519	0.374 ± 0.20

5.4.2 Tensile Testing

The mechanical properties of the electrospun fibers depend on a number of factors including the fiber diameter, porosity and the alignment of the fibrous mesh [19-21]. Mechanical properties such as Young's modulus and tensile strength of the electrospun coaxial fiber mesh before and after CO_2 foaming were calculated from the stress-strain curve as shown in Figure 5-4(a) and 5-4(b) for PCL(PBAT) and PBAT(PCL) samples respectively. Young's modulus, that signifies the stiffness of the material, increases from 53 MPa for PCL(PBAT) to 71 MPa for the foamed PCL(PBAT) sample i.e. an increase of 34%. There was a reduction in the yield strain due to foaming for PCL(PBAT) from 5.45% to 3.34 % i.e. a reduction of 38%. This increase in stiffness can be due to fusing of the porous structure with adjacent fibers during CO_2 foaming process resulting in an increased stiffness of the fibrous mesh. However, there was no significant change observed in the tensile strength of the PCL(PBAT) and foamed PCL(PBAT) samples. Figure 5-4(b) shows the stress-strain response of the PBAT(PCL) and foamed PBAT(PCL) fiber mesh. The modulus of the foamed PBAT(PCL) drops from 61 MPa to 33 MPa i.e. a decrease of 45 %. This decrease in the bulk mechanical properties is due to the porous structure of the core of the fiber. Due to CO_2 foaming, the material is depleted in the core, additionally the solid skin of the coaxial fiber limits the fusing of the porous structure from the adjacent fibers in the mesh resulting in lower modulus value.

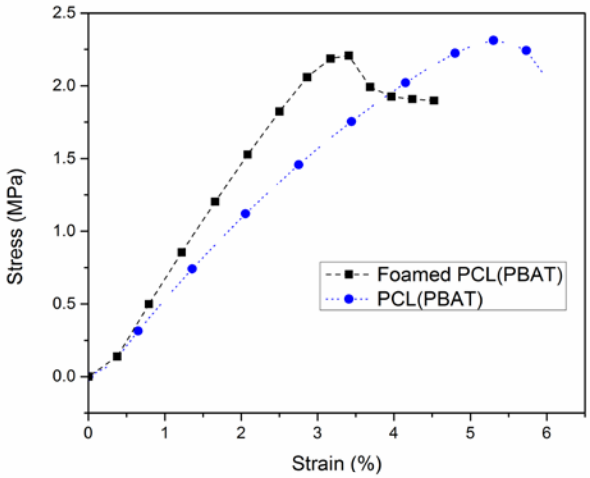

(a)

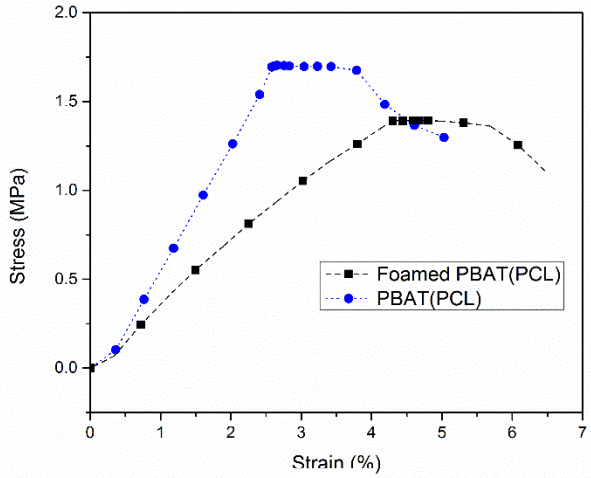

(b)

Figure 5-4. Stress–strain curves of (a) foamed PCL(PBAT) and PCL(PBAT) fibers (b) Foamed PBAT(PCL) and PBAT(PCL) fibers.

Table 5-2 lists the mechanical properties of the coaxial fiber mesh and their foamed samples. Due to the non-uniform nature of porous samples, the difference in Young's Modulus, tensile strength and yield strain of coaxial fiber mesh and their foamed samples were analyzed using statistical methods. The results of t-test analysis with a significant level of 5% showed that there is a significant difference between Young's Modulus and yield strain of PCL(PBAT) and foamed PCL(PBAT) sample. However, there was no significant difference in tensile strength of the samples. Similarly, the t-test analysis with a significant level of 5% for PBAT(PCL) and foamed PBAT(PCL) showed a significant difference in Young's Modulus and yield strain. ANOVA test was also performed, which confirmed the mean value of modulus and yield strain are significantly different.

Table 5-2. Mechanical properties of the coaxial fiber mesh and foamed samples.

	Young Modulus E (MPa)	Tensile Strength σy(MPa)	Yield Strain εy(%)
PCL(PBAT)	53.02 ± 8.54	2.33 ± 0.34	5.45 ± 0.42
Foamed PCL(PBAT)	70.95 ± 10.30	2.23 ± 0.24	3.34 ± 0.41
PBAT(PCL)	61.65 ± 6.03	1.70 ± 0.11	2.85 ± 0.37
Foamed PBAT(PCL)	33.21 ± 4.38	1.22 ± 0.24	4.12 ± 0.38

5.4.3 Dynamic Mechanical Analysis (DMA)

The effect of supercritical CO_2 foaming on the viscoelastic response of the electrospun fiber mesh was observed using DMA. Figure 5-5(a) shows the storage modulus versus temperature plot for the PCL(PBAT) and foamed PCL(PBAT). Storage modulus (E') characterizes the in phase response of the viscoelastic material i.e. the elastic response of the material. It signifies the stiffness of the material and the energy stored in the material when a load is applied. It can be observed from Figure 5-5(a) that the stiffness of the fibers increases for the foamed PCL(PBAT) sample throughout the temperature profile. In the glassy region, there is an increase of 13.5% in the storage modulus of the foamed sample signifying an increase in the elastic response of the sample. While for PBAT(PCL) system there is a reduction of about 50% in the glassy region of the polymer for foamed sample as seen in Figure 5-5(b).

DMA results show a similar trend as observed from the tensile test, i.e. the foaming causes an increase in the elastic response of the PCL(PBAT) fibers resulting in an increase in Young's modulus and storage modulus, while a decrease in Young's

modulus and storage modulus for PBAT(PCL) fibers. However, we observe the much higher value of storage modulus as compared to Young's modulus. The difference in the values is due to the distinct attribute of each technique. The tensile test gives quasi-static time independent response. The transient loading conditions and higher strain rates make it distinct to the DMA response, which is normally performed at much lower strain rate and gives dynamic time-dependent response for the loading. For materials with insignificant damping, Young's modulus is equivalent to storage modulus [22]. However, the difference in magnitude of both observed is due to the viscoelastic nature of the fibers having a high damping property.

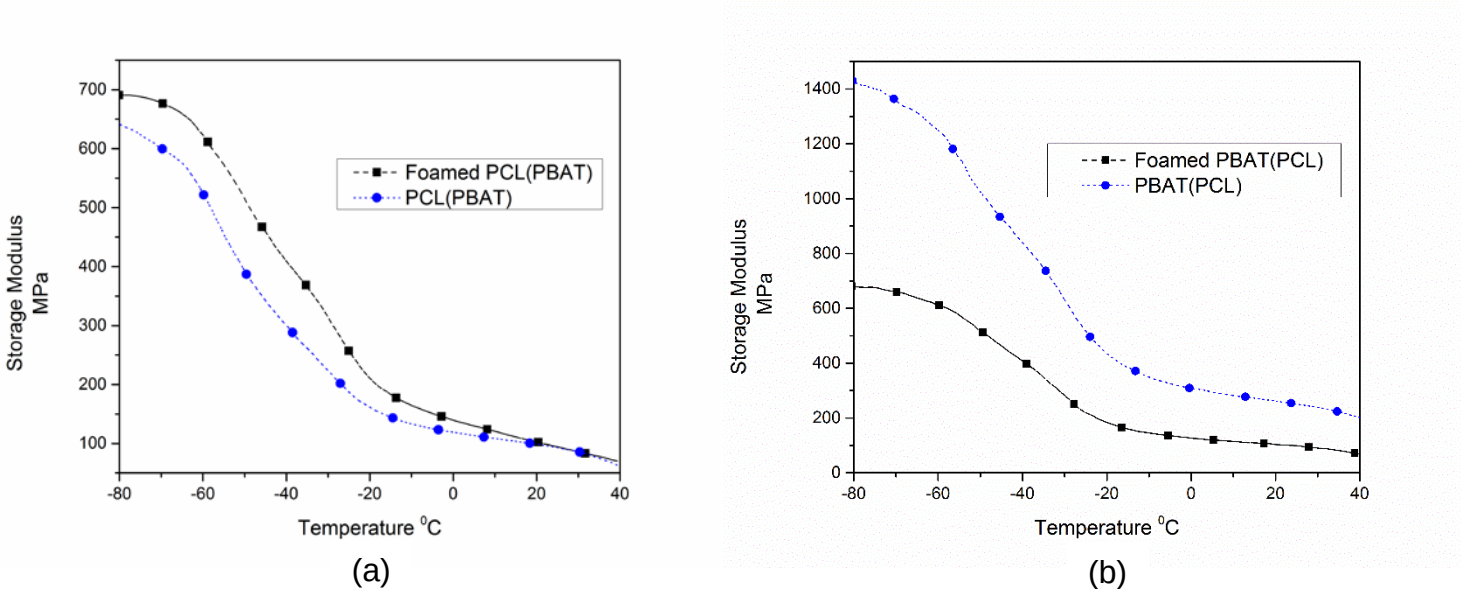

(a) (b)

Figure 5-5. Storage Modulus vs Temperature of (a) foamed PCL(PBAT) and PCL(PBAT) fibers (b) Foamed PBAT(PCL) and PBAT(PCL) fibers.

Figure 5-6(a) and 5-6(b) shows the tan delta versus temperature plot for PCL(PBAT) and PBAT(PCL) system respectively. Two distinct features were observed in both 5-6(a) and 5-6(b), a shoulder around -45 °C indicating the glass transition temperature of PCL and a peak at -25 °C indicating the glass transition temperature

PBAT polymer. Separate glass transition peaks indicate an immiscibility of the polymers. This immiscibility of the polymers helps in separating the phases when exposed to CO_2 resulting in a distinct porous sheath and solid core structure. Since tan delta is defined as the ratio of loss modulus to the storage modulus i.e. the ratio between the viscous response to elastic response of the material. It gives the ratio of energy recovered during the relaxation to energy stored during the loading cycle. From Figure 5-6(a) it can be observed that the CO_2 foaming causes a reduction in the magnitude of tan delta peak. Hence, a porous structure on the surface of fiber results in higher elastic response than the viscous response. However, in Figure 5-6(b), the CO_2 foaming causes an increase in the tan delta peak signifying the porous structure on the core of fiber results in higher damping response.

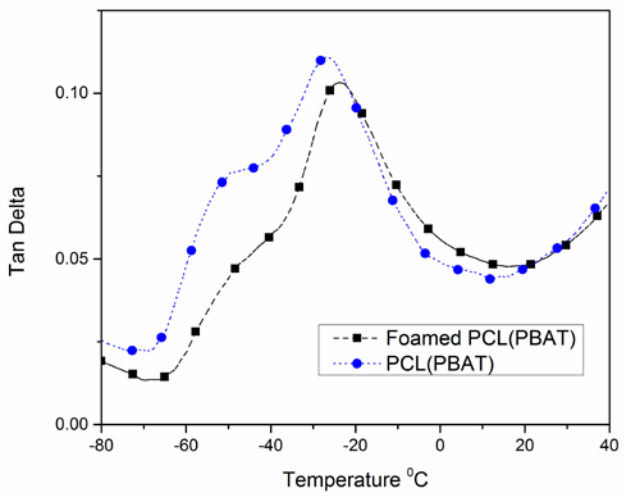

(a)

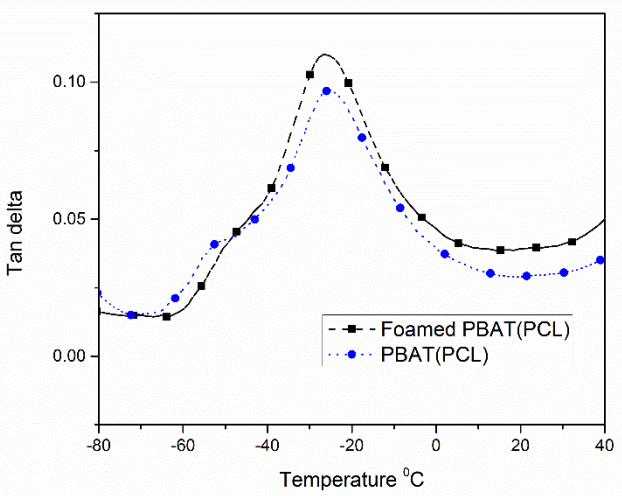

(b)

Figure 5-6. Tan delta vs temperature plot of (a) foamed PCL(PBAT) and PCL(PBAT) fibers (b) Foamed PBAT(PCL) and PBAT(PCL) fibers.

5.4.4 Differential Scanning Calorimeter (DSC)

Differential scanning calorimeter analysis was used to investigate the thermal behavior of the fibers. The enthalpy of melting (ΔHm) and the enthalpy of crystallization (ΔHc) was calculated based on the areas under the solid–liquid phase change peaks of electrospun fibers using the thermal analysis software affiliated with the equipment. From Table 5-3 it can be observed that the heat of fusion and heat of recrystallization reduces for the foamed samples. Two peaks were observed during the heating cycle of each sample (Figure 5-7). First, a sharp endothermic peak around ~60 ^{o}C showing the melting temperature of PCL, while second a broad peak around ~125 ^{o}C was observed indicating the melting point of PBAT polymer.

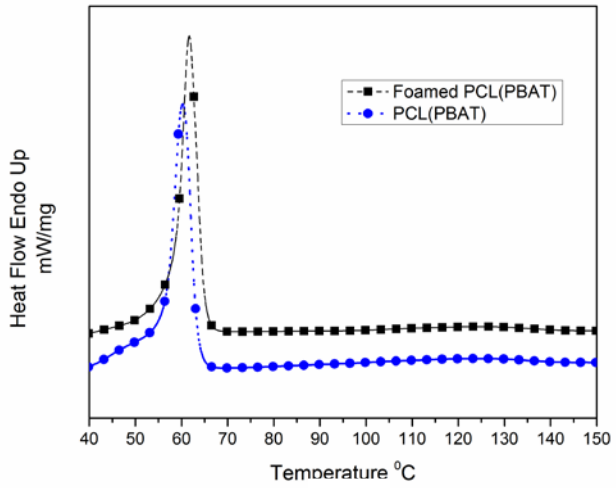

(a)

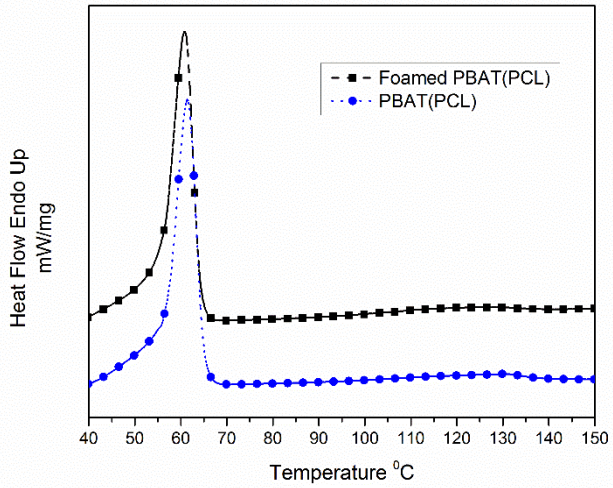

(b)

Figure 5-7. Heating Scan of (a) foamed PCL(PBAT) and PCL(PBAT) fibers (b) Foamed PBAT(PCL) and PBAT(PCL) fibers.

The recrystallization temperature was observed during the cooling cycle. Figure 5-8 shows two exothermic peaks for both PBAT(PCL) and PCL(PBAT) system indicating the recrystallization temperature of PBAT and PCL.

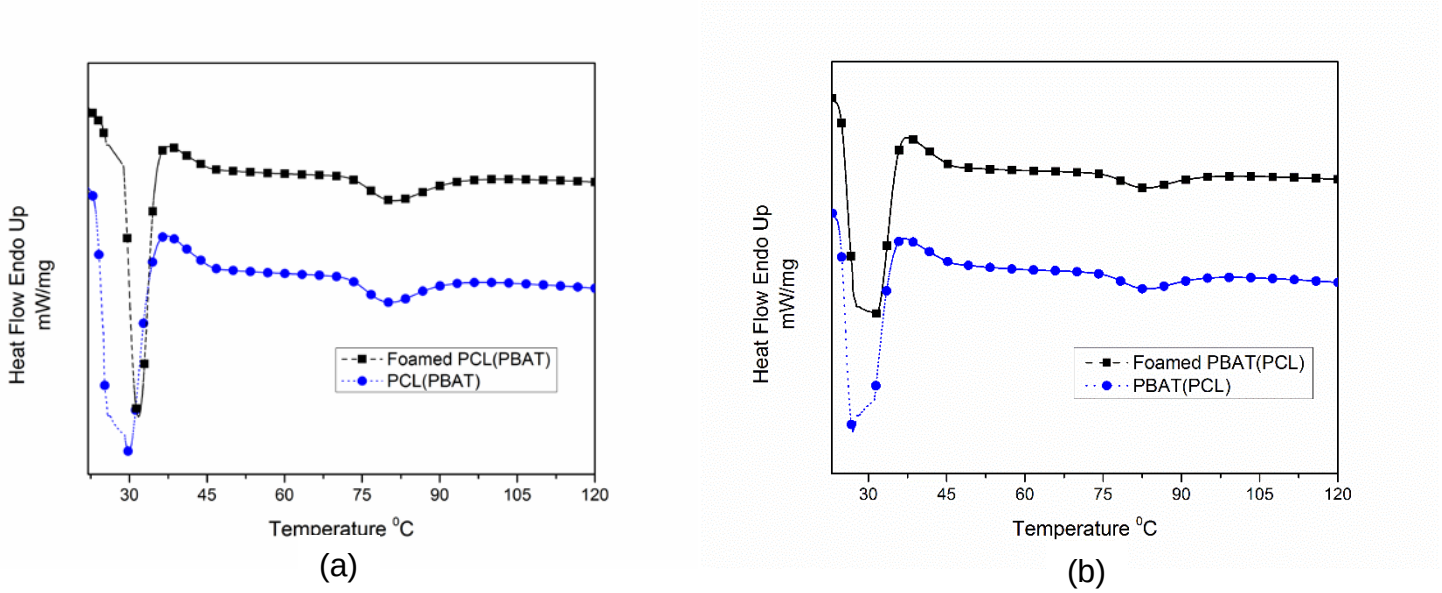

Figure 5-8. Cooling scan of (a) foamed PCL(PBAT) and PCL(PBAT) fibers (b) Foamed PBAT(PCL) and PBAT(PCL) fibers.

The effect of CO_2 foaming on the degree of crystallization of PCL and PBAT were calculated for the fibers using following relations.

$$\chi_{PCL}(\%) = \frac{\Delta H_{m,PCL}}{\Delta H^{0}_{m,PCL}(1-x)} \times 100\% \qquad (1)$$

$$\chi_{PBAT}(\%) = \frac{\Delta H_{m,PBAT}}{\Delta H^{0}_{m,PBAT}(x)} \times 100\% \qquad (2)$$

where $\boldsymbol{\Delta H_{m,PCL}}$ and $\boldsymbol{\Delta H_{m,PBAT}}$ are the enthalpy of melting, $\boldsymbol{\Delta H^{0}_{m,PCL}}$ and $\boldsymbol{\Delta H^{0}_{m,PBAT}}$ are the enthalpy of melting of 100% crystalline PCL taken as 139 J/g [23] and 100% crystalline PBAT taken as 114 J/g [24] respectively, and $\boldsymbol{x}$ is the weight percent of PBAT in the blend equals to 0.234. Due to the exposure of PCL(PBAT) coaxial fibers to supercritical CO_2, the degree of crystallization of PCL decreases from 67.6% to 60.1%, whereas for PBAT it remains almost same around 1.8%. Similarly, for PBAT(PCL)

system the degree of crystallization of PCL remains similar before and after foaming around 42%, whereas for PBAT it decreases from 10.7% to 7.1%.

$$\chi_{total} = (1 - x)(\chi_{PCL}) + (x)(\chi_{PBAT}) \qquad (3)$$

The overall degree of crystallization was calculated using equation 3 which show a decrease from 52.1% for PCL(PBAT) coaxial fibers to 46.5% for the foamed samples. Similarly, for PBAT(PCL) system there is a decrease from 36.1% to 33.4%. By examining the values heat of fusion (ΔH_m) and heat of crystallization (ΔH_c) in Table 5-3 it can be observed that the heat generated for the polymer reduce significantly if they are present in the core of the coaxial fiber.

Table 5-3. Thermal Characteristic of the coaxial fiber mesh and foamed samples.

	Tm (^{0}C)		**Tc (^{0}C)**		**ΔHm (J/g)**		**ΔHc (J/g)**	
	PCL	PBAT	PCL	PBAT	PCL	PBAT	PCL	PBAT
PCL(PBAT)	57.8	117	32.6	87.1	72.0	0.45	46.8	0.39
Foamed PCL(PBAT)	59.1	123	34.4	88.5	64.0	0.55	42.1	0.62
PBAT(PCL)	61.4	129	27.1	82.6	46.8	2.88	28.6	1.7
Foamed PBAT(PCL)	60.8	121	31.4	82.8	44.2	1.91	36.4	2.1

5.5 Conclusions

In this chapter, we have reported a technique to generate porous coaxial fibers using supercritical carbon dioxide foaming. Notable to our approach is that the porosity was successfully introduced in the core as well as sheath while maintaining the structural integrity of the fiber. Cross-sectional image of coaxial fiber shows promising results indicating an optimal coaxial spinning. The uniform pore (cell) diameter was observed at

the cross-section while the pore (cell) density increases 3 fold for the sheath as compared to the core of the coaxial fiber. The average cell diameter of 0.37 μm was observed and cell density (Na) was calculated in the order of 10^{11} cells/cm^3. Properties of the porous structure were compared with the non-porous fibers. Tensile tests showed an increase of 34% in the stiffness of foamed PCL(PBAT) fibers, while a decrease of 45% for foamed PBAT(PCL) fibers. DMA results also showed a similar trend of increased elastic response for foamed PCL(PBAT) and increase viscous response for foamed PBAT(PCL). Two distinct glass transition peaks indicated an immiscibility of the polymers. However, the glass transition temperature of the foamed PCL(PBAT) sample shows a shift towards higher temperature. DSC results showed a decrease in the degree of crystallization of the foamed sample. The results show depending on the CO_2 miscibility to the polymer we can successfully manipulate the architecture of the cross-section of the electrospun fiber and can tailor to the required application.

5.6 References

[1] D. Ramesh, B. G. Ayre, N. D'Souza, C. L. Webber III, 2015, "Dynamic mechanical analysis, surface chemistry and morphology of alkali and enzymatic retted kenaf fibers," Textile Research Journal, 85, 2059-2070.

[2] B. G. Ayre, K. Stevens, K. D. Chapman, C. L. Webber III, K. L. Dagnon, N. A. D'Souza, 2009, "Viscoelastic Properties of Kenaf Bast Fiber in Relation to Morphology of Development", Textile Research Journal, 79, 973–980.

[3] S. M. Ogbomo, B. Ayre , C. L. Webber III and N. A. D'Souza, 2014, "Effect of Kenaf Fiber Age on PLLA composite properties, Polymer Composites, 35, 915-924.

[4] N. A. D'Souza, M. S. Allen, K. Stevens, B. Ayre, D. K. Visi, S. Vidhate, I. Ghamarian, and C. L. Webber III, (2011) "Biocomposites: The Natural Fiber Contribution from Bast and Woody Plants". In: C.L. Webber III and A. Liu (Eds.). Plant Fibers as Renewable Feedstocks for Biofuel and Bio-based Products. CCG International Inc (2011).

[5] Arvidson, Sara A, Wong, Ka C., Gorga, Russell E., Khan, Saad A., 2012, “Structure, molecular orientation, and resultant mechanical properties in core/ sheath poly(lactic acid)/polypropylene composites,” Polymer, Vol. 53(3), pp. 791.

[6] Yanzhong Zhang, Zheng-Ming Huang, Xiaojing Xu, Chwee Teck Lim, and Seeram Ramakrishna, 2004, “Preparation of Core−Shell structured PCL-r-gelatin bi-component nanofibers by coaxial electrospinning,” Chem. Mater., Vol. 16(18), pp. 3406-3409.

[7] Md. Fazley Elahi, Wang Lu, Guan Guoping and Farzana Khan, 2013, “Core-shell fibers for biomedical applications-A review,” Journal of Bioengineering & Biomedical Science, Vol. 3(1), pp. 121.

[8] Wang, X., Ding, B., and Li, B., 2013, “Biomimetic electrospun nanofibrous structures for tissue engineering,” Materials Today, Vol. 16(6), pp. 229-241.

[9] Deitzel, J. M., J. Kleinmeyer, D. Harris, and N. C. Beck Tan., 2001, “The effect of processing variables on the morphology of electrospun nanofibers and textiles,” Polymer, Vol. 42(1), pp. 261-72.

[10] Qin, Xiaohong, and Dequn Wu., 2012, “Effect of different solvents on poly(caprolactone) (PCL) electrospun nonwoven membranes,” Journal of Thermal Analysis and Calorimetry, Vol. 107(3), pp. 1007-13.

[11] Peresin, Maria S., Youssef Habibi, Arja-Helena Vesterinen, Orlando J. Rojas, Joel J. Pawlak, and Jukka V. Seppälä, 2010, “Effect of moisture on electrospun nanofiber composites of poly(vinyl alcohol) and cellulose nanocrystals,” Biomacromolecules, Vol. 11(9), pp. 2471-7.

[12] Roya M. Nezarati, Michelle B. Eifert, and Elizabeth Cosgriff-Hernandez, 2013, “Effects of humidity and solution viscosity on electrospun fiber morphology,” Tissue Engineering Part C: Methods, Vol. 19(10), pp. 810-819.

[13] Richards, Esther, Reza Rizvi, Andrew Chow, and Hani Naguib, 2008, “Biodegradable composite foams of PLA and PHBV using subcritical CO2,” Journal of Polymers and the Environment, Vol. 16(4), pp. 258-66.

[14] Ayodeji, Olukemi, Emily Graham, Douglas Kniss, John Lannutti, and David Tomasko, 2007, “Carbon dioxide impregnation of electrospun polycaprolactone fibers,” The Journal of Supercritical Fluids, Vol. 41(1), pp. 173-8.

[15] Liu, Jun, Zhihao Shen, Sang-Ho Lee, Manuel Marquez, and Mark A. McHugh, 2010, “Electrospinning in compressed carbon dioxide: Hollow or open-cell fiber formation with a single nozzle configuration,” The Journal of Supercritical Fluids, Vol. 53(1–3), pp. 142-50.

[16] Pu, J., & Komvopoulos, K. (2014). Mechanical properties of electrospun bilayer fibrous membranes as potential scaffolds for tissue engineering. Acta Biomaterialia, 10(6), 2718-2726.

[17] Ero-Phillips O, Jenkins M, Stamboulis A. Tailoring Crystallinity of Electrospun Plla Fibres by Control of Electrospinning Parameters. Polymers. 2012; 4(3):1331-1348.

[18] Vipin Kumar and Nam P. Suh, 1990, “A process for making microcellular thermoplastic parts” Polym. Eng. Sci., Vol. 30(20), pp. 1323-29.

[19] Forouhardshad M, Saligheh O, Arasteh R, Farsani R E., 2010, “Manufacture and Characterization of Poly (butylene terephthalate) Nanofibers by Electrospinning,” Journal of Macromolecular Science, Vol. 49, pp. 833.

[20] Croisier, F., A. -S Duwez, C. Jérôme, A. F. Léonard, K. O. van der Werf, P. J. Dijkstra, & M. L. Bennink, 2012, “Mechanical testing of electrospun PCL fibers,” Acta Biomaterialia, Vol. 8(1), pp. 218-24.

[21] Kim Y H, Min Y K, Lee B T., 2012, “Fabrication and material properties of fibrous PHBV scaffolds depending on the cross-ply angle for tissue engineering,” J Biomat. App., Vol. 27(4), pp. 457-468.

[22] Hay, J., Herbert, E., 2013, “Measuring the complex modulus of polymers by instrumented indentation testing,” Exp. Tech., Vol. 37, pp. 55-61

[23] Hatakeyama, T., Izuta, Y., Hirose, S., & Hatakeyama, H., 2002, “Phase transitions of lignin-based polycaprolactones and their polyurethane derivatives,” Polymer, Vol. 43(4), pp. 1177-1182.

[24] Madera-Santana, T. J., Misra, M., Drzal, L. T., Robledo, D., and Freile-Pelegrin, Y., 2009, “Preparation and characterization of biodegradable agar/poly(butylene adipate-co-terephatalate) composites,” Polymer Engineering & Science, Vol. 49(6), pp. 1117-1126.

CHAPTER 6

FUNCTIONAL PERFORMANCE IN FIBERS BY DESIGN

6.1 Introduction

The versatile properties of the natural fibers is enabled by the architecture of its cross-section. These fibers are engineered in a hierarchical design, which gives functionality at the nanoscale as well as structural properties at the macroscale. A porous core and solid sheath provides the stiffness as well as the damping characteristic to the structure. This unique characteristic of natural fibers have created interest in bioinspired materials design.

The ability to create uniform fibers having diameters up to a few nanometers has made electrospinning a valuable approach for many ranging from applications of tissue engineering [1], water filtration [2] and energy harvesting [3]. Electrospinning works on the principle of electrostatic charge difference between the tip of the ejecting needle and the collector, the polymer solution is subjected to high voltage which induced a polarity to the solution causing it to attracted to the opposite polarity charge. The orientation of the fibers can be can be altered based on the grounded collector. The macro mechanical performance of the fiber mesh depends on the fiber orientation and diameter [4]. Aligned fibers can be achieved by collecting fibers on a rotating mandrel [5].

In this chapter, prediction of the mechanical properties of coaxial electrospun fibers having solid and porous core were investigated. The tensile test was performed to evaluate the stiffness and elongation of the fiber mesh. A hyperelastic and viscoelastic material model was developed to study the effect of porosity and interaction between

the electrospun fibers. Finite element analysis was performed and compared with the experimental results.

6.2 Experimental

6.2.1 SEM Analysis

Scanning electron microscopy was used to investigate the surface and cross-section of the porous core and solid sheath coaxial fibers. The porosity was induced by supercritical carbon dioxide. Samples were sputter coated with gold particles under vacuum before the SEM observation. Image J software was used to measure the diameter of the fibers, which averaged 15 µm. Figure 6-1 shows the surface and cross section of the coaxial fibers. CO_2 immiscible polymer (PBAT) was at the sheath of the fibers, no porosity or dimensional change in PBAT was observed after CO_2 exposure. However, the core made up of PCL showed uniform porosity throughout the cross-section. Moreover, no physical detachment of the two polymer surfaces was observed indicating a successful amalgamation of polymers at the boundary of core and sheath.

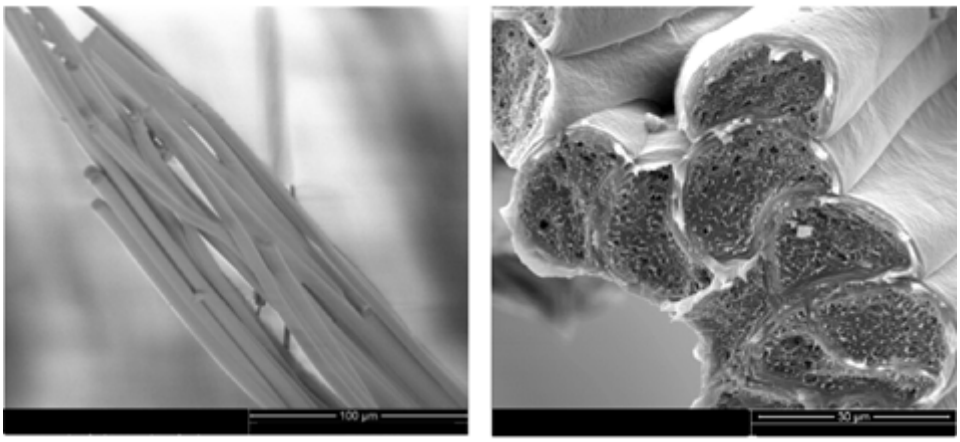

Figure 6-1. Foamed PBAT(PCL) and cross-sectional view of foamed PBAT(PCL) electrospun fibers.

6.2.2 Mechanical Properties

Mechanical properties such as Young's modulus and tensile strength of the electrospun coaxial fiber mesh before and after CO_2 foaming were calculated from the stress-strain curve as shown in Figure 6-2 for PBAT(PCL) sample. Young's modulus, that signifies the stiffness of the material, decreases from 61 MPa to 33 MPa i.e. a decrease of 45 %. This decrease in the bulk mechanical properties is due to the porous structure of the core of the fiber. CO_2 foaming causes the depletion of material in the core. Additionally, the solid skin of the coaxial fiber limits the fusing of the porous structure from the adjacent fibers in the mesh resulting in a lower modulus value.

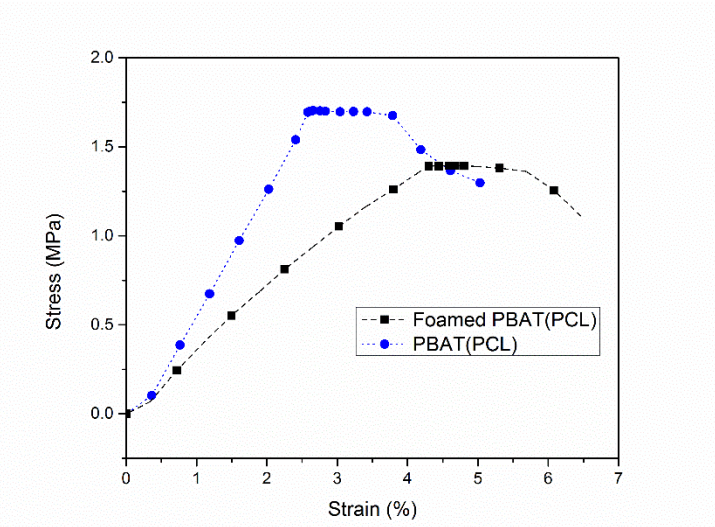

Figure 6-2. Stress–strain curves of Foamed PBAT(PCL) and PBAT(PCL) fibers.

As observed from scanning electron microscopy, only PCL was affected by CO_2 foaming, resulting in a porous structure and decrease in modulus. To eliminate the effect of sheath polymer (PBAT), viscoelastic properties of PCL before and after foaming was investigated. Complex Modulus of PCL before and after foaming was measured with respect to time. Mathematically given by the following relation:

$$E(t) = E_\infty \frac{1 - \sum_{i=1}^{N} g_i (1 - e^{\frac{-t}{\tau_i}})}{1 - \sum_{i=1}^{N} g_i} \ldots\ldots\ldots (1)$$

Laplace transformation of the complex modulus converts time domain to frequency domain, resulting in the frequency dependence of the preceding modulus, which separates the real and imaginary parts.

$$E(\omega) = E_\infty \frac{1 - \sum_{i=1}^{N} \frac{g_i}{1 + \tau_i^2 \omega^2} + j \sum_{i=1}^{N} \frac{g_i \tau_i \omega}{1 + \tau_i^2 \omega^2}}{1 - \sum_{i=1}^{N} g_i} \ldots\ldots\ldots (2)$$

The real part gives the storage modulus while the imaginary part gives the loss modulus of the above equation. Storage modulus (E') characterizes the in phase response of the viscoelastic material i.e. the elastic response of the material. It signifies the stiffness of the material. Figure 6-3 shows that the elastic response drops significantly for the foamed PCL due to the material lost.

$$\text{Storage Modulus: } E'(\omega) = E_\infty \frac{1 - \sum_{i=1}^{N} \frac{g_i}{1 + \tau_i^2 \omega^2}}{1 - \sum_{i=1}^{N} g_i} \ldots\ldots\ldots (3)$$

$$\text{Loss Modulus: } E''(\omega) = E_\infty \frac{\sum_{i=1}^{N} \frac{g_i \tau_i \omega}{1 + \tau_i^2 \omega^2}}{1 - \sum_{i=1}^{N} g_i} \ldots\ldots\ldots (4)$$

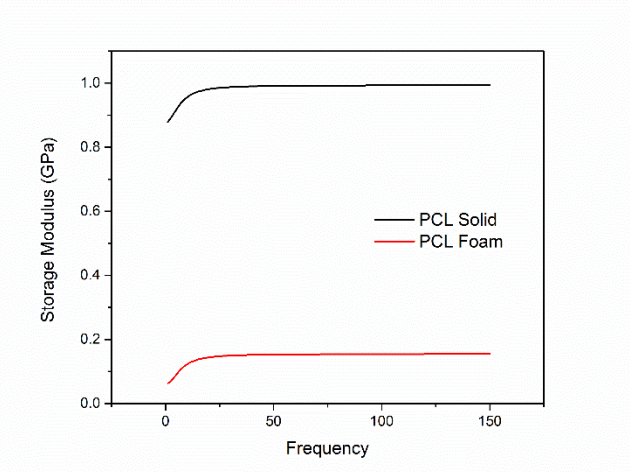

Figure 6-3. Storage modulus versus frequency of the PCL before and after CO_2 foaming.

where tan δ is the ratio of loss modulus to the storage modulus. It measures the energy dissipation of a material i.e. how good a material is at absorbing energy. PCL after CO_2 foaming showed a significant increase in dissipation (Figure 6-4).

$$\tan \delta = \frac{E'}{E''} \dots\dots\dots (5)$$

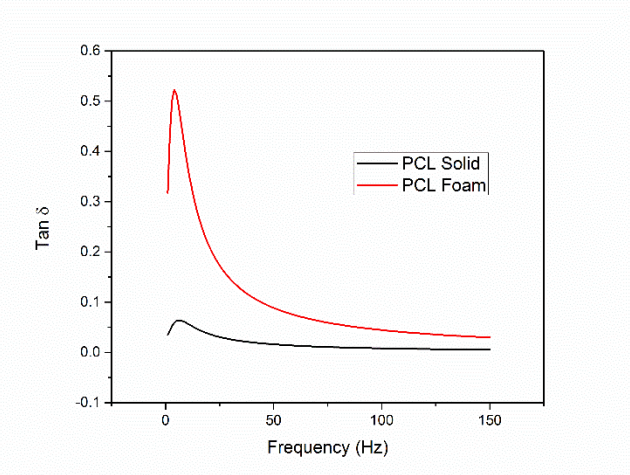

Figure 6-4. Tan δ versus frequency of PCL before and after foaming.

6.3 Finite Element Analysis

6.3.1 Material Model

Quasi-static uniaxial test and shear relaxation test of PCL before and after CO_2 foaming and PBAT was performed to create the material models. Two types of models were investigated to capture the mechanical response of the PCL and PBAT based on hyperelastic and viscoelastic theory. The hyper-elastic model was used to represent the nonlinear elasticity of the polymers, however, it lacks the time dependence of the material. To capture the time dependence response of the polymers, a linear viscoelastic model was used.

6.3.2 Hyperelastic Model Calibration

For a hyperelastic material there exists an elastic potential function W which is scalar function of one of the strain or deformation tensors, whose derivative with respect to a strain component determines the corresponding stress component. This is represented by the following relation:

$$S_{ij} = \frac{\partial W}{\partial E_{ij}} = 2\frac{\partial W}{\partial C_{ij}}$$

where:

S_{ij}= components of the second Piola-Kirchhoff stress tensor

W= strain-energy function per unit undeformed volume

E_{ij}= components of the Lagrangian strain tensor

C_{ij}= components of the right Cauchy-Green deformation tensor

The Lagrangian strain is expressed as follow:

$$E_{ij} = \frac{1}{2}(C_{ij} - \delta_{ij})$$

where:

δ_{ij}= Kronecker delta (δ_{ij}= 1, i=j; δ_{ij}=0, i ≠ j)

The deformation tensor C_{ij} is comprised of the products of the deformation gradients F_{ij}.

$C_{ij} = F_{ki}F_{kj}$= component of the Cauchy-Green deformation tensor.

where:

F_{ij}= components of the deformation gradient tensor.

X_i= undeformed position of a point in direction i

$x_i = X_i + u_i$= deformed position of a point in direction i

u_i= displacement of a point in direction i

The Kirchhoff stress is given as:

$$\tau_{ij} = F_{ik}S_{kl}F_{jl}$$

whereas, the Cauchy stress is obtained by:

$$\sigma_{ij} = \frac{1}{J}\tau_{ij} = \frac{1}{J}F_{ik}S_{kl}F_{jl}$$

The principal stretch ratios (eignenvalues) of C_{ij} are λ_1^2, λ_2^2, and λ_3^2, and exists only if:

$$det\left[C_{ij} - \lambda_p^2\delta_{ij}\right] = 0$$

which can be re-expressed as:

$$\lambda_p^6 - I_1\lambda_p^4 + I_2\lambda_p^2 - I_3 = 0$$

where:

$$I_1 = \lambda_1^2 + \lambda_2^2 + \lambda_3^2$$
$$I_2 = \lambda_1^2\lambda_2^2 + \lambda_2^2\lambda_3^2 + \lambda_3^2\lambda_1^2$$
$$I_3 = \lambda_1^2\lambda_2^2\lambda_3^2 = J^2$$

and $J = det\left[F_{ij}\right]$, J is also the ratio of the deformed elastic volume over the undeformed volume of the material.

The uniaxial tension quasi-static test data was used to calibrate the hyperelastic model for PBAT, PCL before and after CO_2 foaming. Different hyperelastic models were tested to effectively model the response of polymers. Polynomial model (N=2) was used to predict the non-linear elastic behavior of PBAT, whereas Ogden Potential model was used to model the PCL polymer. Figure 6-5 shows the correlation of the experimental and simulation results. The strain energy density function of the polynomial model is given by:

$$W = \sum_{i+j=1}^{N} C_{ij}(\overline{I_1} - 3)^i(\overline{I_2} - 3)^j + \sum_{K=1}^{N}\frac{1}{d_k}(J-1)^{2k} \ldots\ldots\ldots (6)$$

where N, C_{ij}, d_k are material constants.

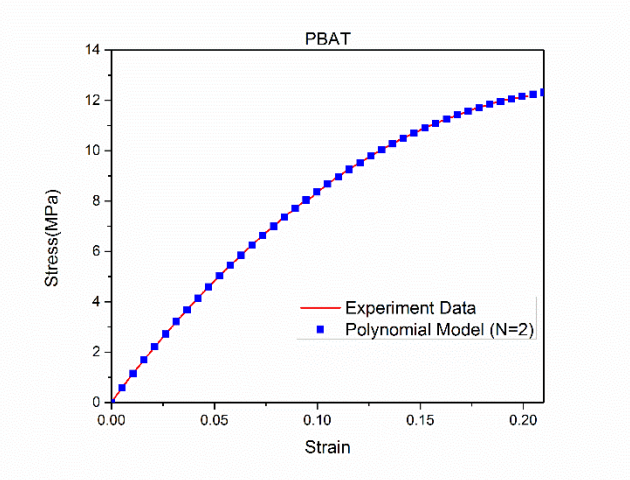

Figure 6-5. Correlation of uniaxial tensile and simulation result for PBAT.

Ogden model was used to fit the stress strain behavior of PCL before and after CO_2 foaming. This hyperelastic model describes the material response by strain energy density function which is expressed in terms of principle stretches of left-Cauchy strain tensor, which has the form:

$$W(\lambda_1, \lambda_2, \lambda_3) = \sum_{p=1}^{N} \frac{\mu_p}{\alpha_p}\left(\lambda_1^{\alpha_p} + \lambda_2^{\alpha_p} + \lambda_3^{\alpha_p} - 3\right) + \sum_{k=1}^{N} \frac{1}{d_k}(J-1)^{2k} \dots\dots\dots (7)$$

where N, μ_p, d_k and α_p are material constants. Similar to the polynomial form there is no limitation on N. A higher value of N will give a better fit, but increase the numerical complexity. Hence a value of N greater than 3 is not recommended. The initial shear modulus, μ, is given as:

$$\mu = \frac{1}{2}\sum_{i=1}^{N} \alpha_i \mu_i$$

whereas the initial bulk modulus is given as:

$$K = \frac{2}{d_1}$$

Figure 6-6 shows the correlation of calibrated Ogden potential coefficient with experimental test data.

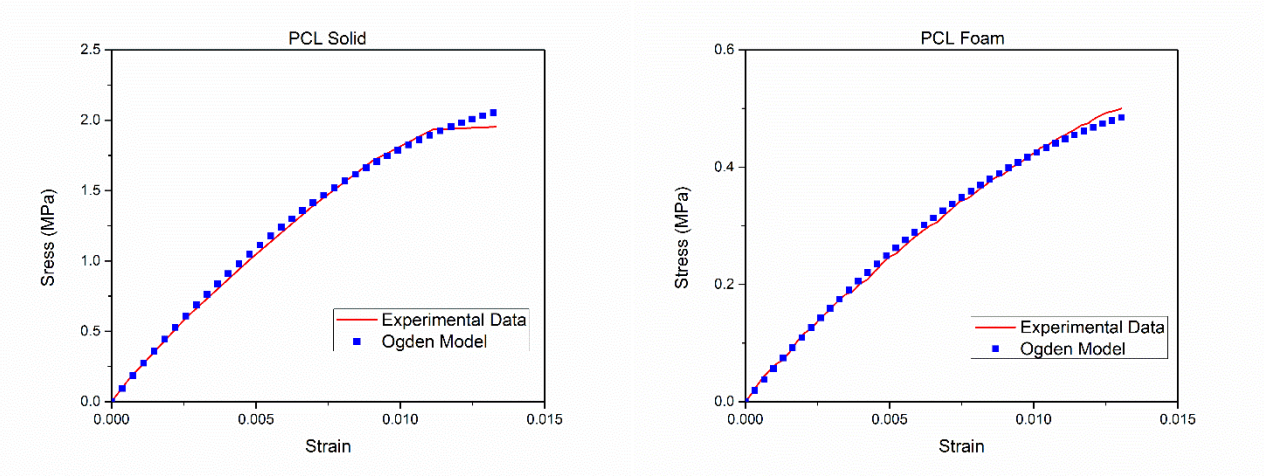

Figure 6-6. Correlation of uniaxial tensile and simulation result for (a) PCL solid and (b) PCL foam.

The above mentioned hyperelastic material models predict the nonlinear elastic response from the quasi-static testing. However, when the material is loaded at higher strain rate, it behaves differently depending on the strain rate. To incorporate time dependence effect, a viscoelastic part was added to the model. The combination of the hyperelastic and viscoelastic material model was used to represent the nonlinear elastic and strain-rate dependent behavior of the material.

6.3.3 Viscoelastic Model Calibration

Viscoelastic materials contains both the elastic and viscous part. When the load is applied we observed an instantaneous elastic response, whereas the viscous part occurs over a period of time. The constitutive equation for an isotropic viscoelastic material is given as follow, which can recover the elastic behavior through rate dependence of (slow and fast loading).

$$\sigma = \int_0^t 2G(t-\tau)\frac{de}{d\tau} + I\int_0^t K(t-\tau)\frac{d\,\Delta}{d\tau}d\tau$$

where:

σ= Cauchy stress

e= deviatoric part of strain

Δ= volumetric part of the strain

G(t)= shear relaxation kernel function

K(t)= bulk relaxation kernel function

t= current time

τ= past time

I= unit tensor

The kernel functions are represented in terms of prony series, which assumes that:

$$G = G_\infty + \sum_{i=1}^{n_G} G_i \exp\left[\frac{-t}{\tau_i^G}\right]$$

$$K = K_\infty + \sum_{i=1}^{n_K} K_i \exp\left[\frac{-t}{\tau_i^K}\right]$$

where:

G_∞, G_i= shear elastic moduli

K_∞, K_i= bulk elastic moduli

τ_i^G, τ_i^K= relaxation times for each Prony component

Relative moduli is given as

$$\alpha_i^G = \frac{G_i}{G_0}$$

$$\alpha_i^K = \frac{K_i}{K_0}$$

where:

$$G_0 = G_\infty + \sum_{i=1}^{n_G} G_i$$

$$K_0 = K_\infty + \sum_{i=1}^{n_K} K_i$$

Hence, the kernel functions can be equivalently expressed as:

$$G = G_0 \left[\alpha_\infty^G + \sum_{i=1}^{n_G} \alpha_i^G exp\left(-\frac{t}{\tau_i^G} \right) \right]$$

$$K = K_0 \left[\alpha_\infty^K + \sum_{i=1}^{n_K} \alpha_i^K exp\left(-\frac{t}{\tau_i^K} \right) \right]$$

Here the G_0 and K_0 are the shear and bulk modulus are the instantaneous moduli i.e. at the fast load limit. Whereas, G_∞ and K_∞ are the moduli at the slow limit. The Prony representation corresponds to the solution of the parallel Maxwell model of viscoelasticity.

Stress relaxation test was performed to create the viscoelastic part of the material model. In which, the material is subjected to an instantaneous strain which is kept constant, while the varying stress is calculated over the period of time. The instantaneous modulus is due to the elastic response of the material, while for viscoelastic material the stress relaxes with time causing a decrease in the modulus [6]. The RSA III Dynamic mechanical analyzer was used in a transient mode to perform the test. The material was instantly strained to 50% of the yield value while measuring the stress value for a period of 600 sec. The linear viscoelastic model known as generalized Maxwell model or Prony series was used to fit the normalized shear modulus data using the following expression:

$$G(t) = G_\infty + \sum_{i=1}^{N} G_i e^{\frac{-t}{\tau_i}} \dots\dots\dots (8)$$

where G_∞ is the modulus of material when it is fully relaxed and τ_i are the relaxation time.

Table 6-1. Prony series coefficient of PBAT and PCL before and after CO_2 foaming.

	PCL(Solid)		PCL(Foam)		PBAT	
i	**g(i)**	**τ(i)**	**g(i)**	**τ(i)**	**g(i)**	**τ(i)**
1	0.11565	0.14399	0.6195	0.14047	0.0710356	1.1357
2	0.0757988	5.1551	0.1315	2.5524	0.0599107	114.079
3	0.0505466	180.16	-	-	0.0734537	203.78

A built-in curve fitting tool in ANSYS was used to calculate the Prony series coefficient. The total error value was set to 0.01 which resulted in three and two-term prony series. Table 6-1 lists the prony coefficient for PBAT and PCL before and after CO_2 foaming. Figure 6-7 shows the prony coefficients accurately capture the viscoelastic response of the polymers.

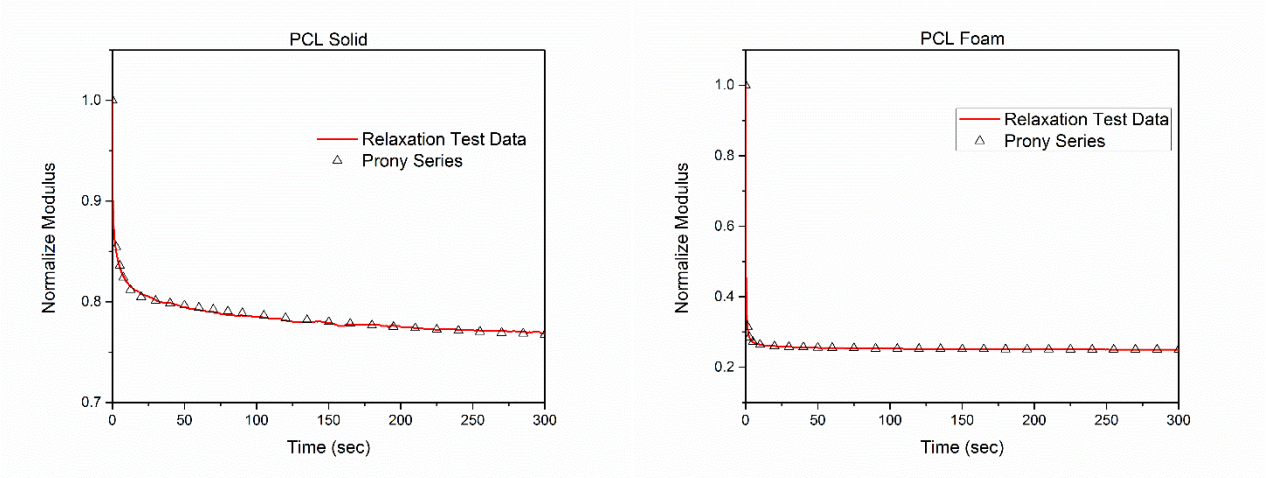

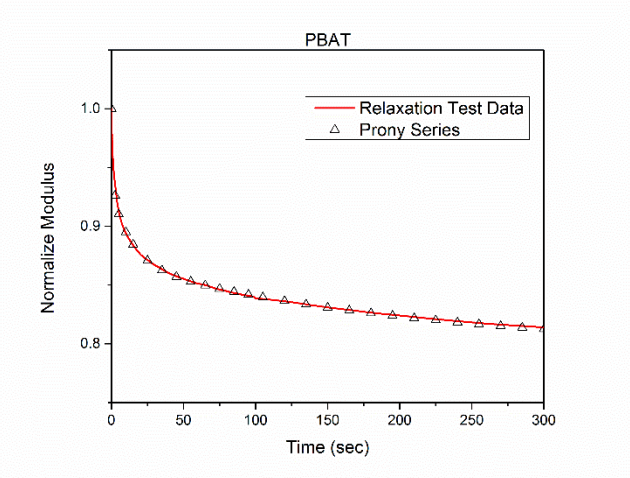

Figure 6-7. Comparison of Prony series function to the test data.

6.3.4 Fiber Mesh Geometry

Autodesk Inventor was used to creating 8 individual coaxial fibers join together to form a unit cell representation of electrospun mesh. The geometry was then exported to ANSYS workbench for meshing and analysis. A three-dimensional fiber mesh was created using the dimensional parameters obtained from the SEM investigation. Each coaxial fiber was modeled having 15 µm outer diameter and 13 µm core diameter. The following assumptions were made for analysis [7]: The fibers are aligned and oriented in the same plane. The fiber diameter is uniform throughout the length of fibers. Fiber interactions were incorporated in the model, the contact between the core and sheath polymer was considered bonded while the contact surface between the individual fibers was taken as rough.

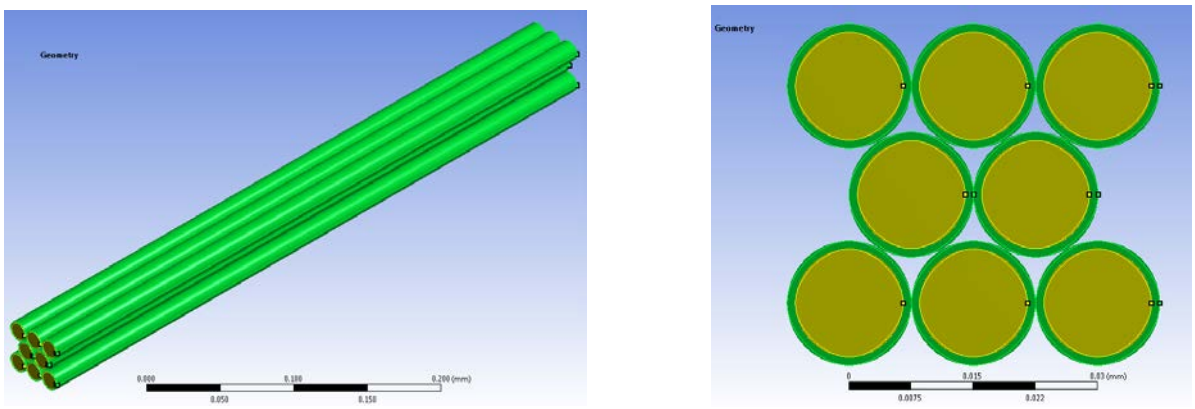

Figure 6-8. Unit cell representation of coaxial electrospun mesh.

6.3.5 Comparison between Experiment and Model Results

The tensile behavior of electrospun coaxial PBAT and PCL fiber mesh was compared with the finite element model. The results indicates that the tensile properties of fibrous meshes are sensitive to the architecture of micro structure. Figure 6-9 compare the tensile stress-strain curve of modeled coaxial fibers and experimental data. The proposed model successfully predicts the strain response at lower strain values for the solid coaxial fibers however at higher strain rate it deviated from the experimental results. The modulus computed for solid PBAT(PCL) was 60.1 MPa as compared to 61 MPa from the experimental results. For foamed PBAT(PCL) sample, it gives a similar non-elastic response as experiment (Figure 6-9(b)), however it over predicts the modulus to 36 MPa as compared to 33 MPa from the experiment.

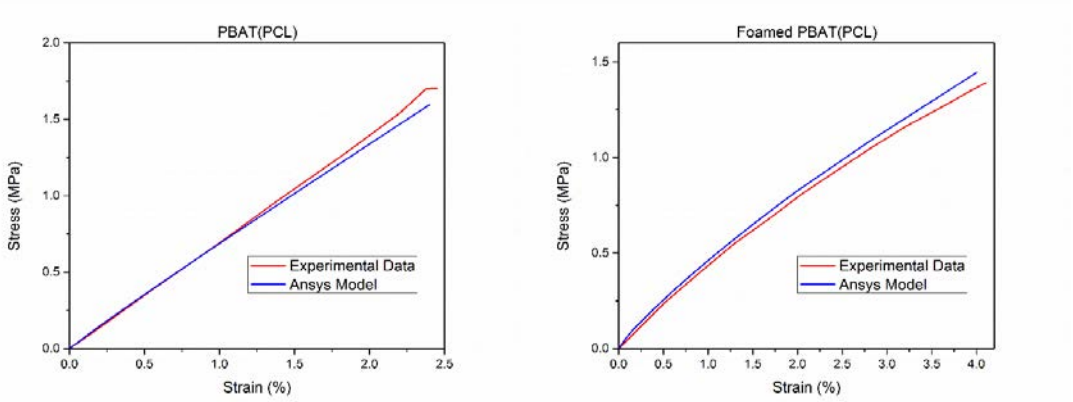

Figure 6-9. Comparison of stress strain curve between the proposed model and experimental data.

6.3.6 Design of Coaxial Fibers

Coaxial fibers designed for mechanical properties by changing the skin and core polymers and varying the diameter for the core polymers. Three diameters of 5 microns, 7.5 microns, and 13 microns were considered. Figure 6-10 shows the effect of a change in polymer content on the stress-strain curves. PBAT fibers having low stiffness and high flexibility, while PCL fibers having high stiffness and lower flexibility were joined at different ratios to engineer mechanical modulus in between 23 MPa to 165 MPa as shown in Table 6-2.

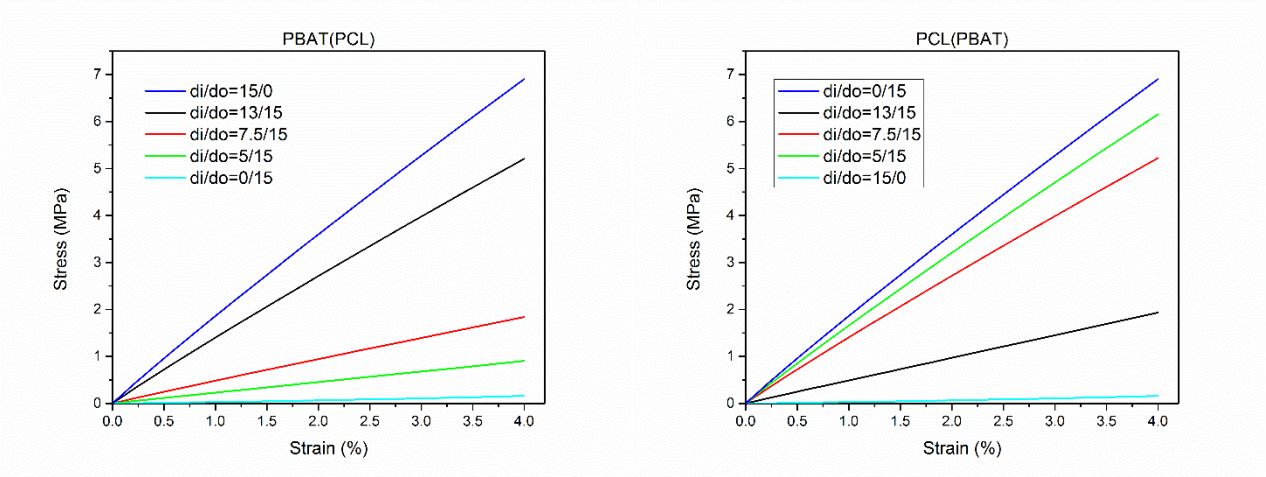

Figure 6-10. Stress strain curve of solid coaxial fibers at different diameter ratios.

Figure 6-11 shows a comparison between the modulus predicted using the rule of mixtures, ANSYS model, and experimental results. Both FEA model and rules of mixture over predicted the modulus value as compared to the experimental results, this can be due to interaction of individual polymers in the coaxial fibers that limits the mechanical potential of polymers.

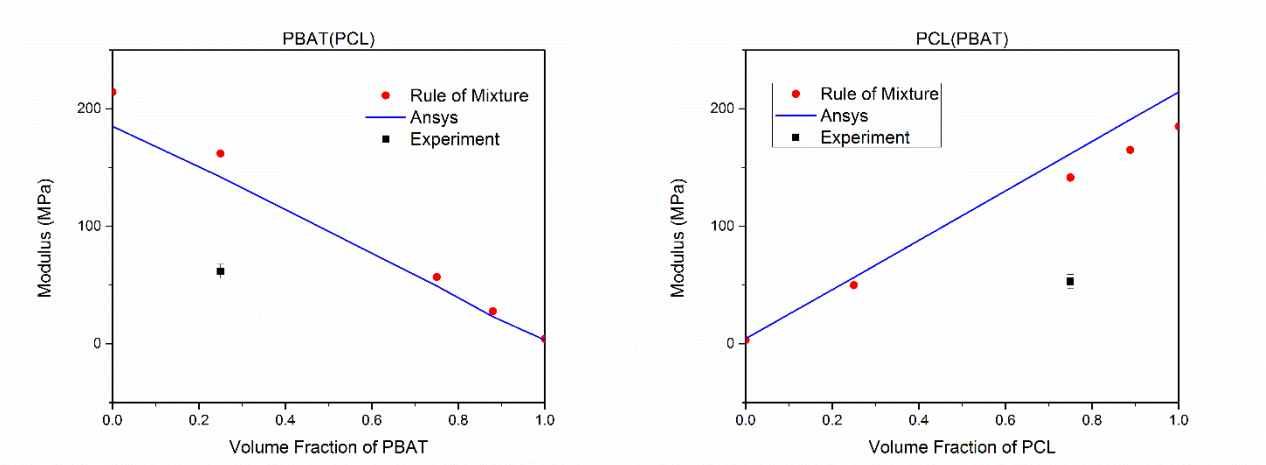

Figure 6-11. Comparison between the modulus values predicted by the rule of mixtures, ANSYS model and experimental values of solid coaxial fibers.

Figure 6-12 shows the effect of the position of polymer either in core or skin of fibers on the modulus of the fabric. It can be observed that PCL has a higher effect on the skin as compared to the core of the fiber. Figure 6-13 shows the effect of location and diameter of porous fibers on the mechanical properties of the fabrics. The mechanical modulus varies from 5.5 MPa to 29 MPa based on the location and diameter as shown in Table 6-2.

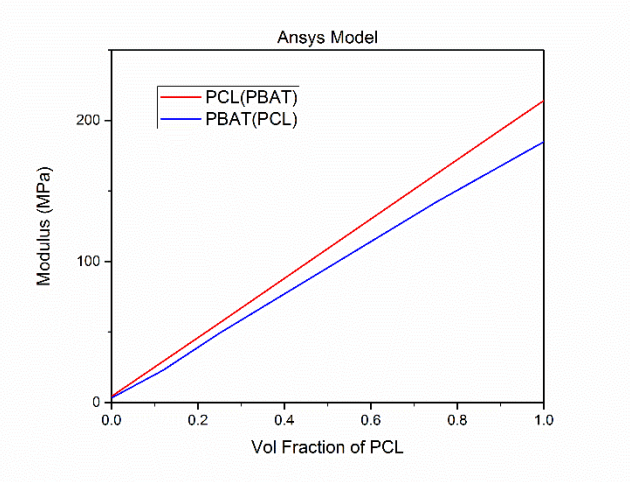

Figure 6-12. ANSYS model for solid coaxial fibers.

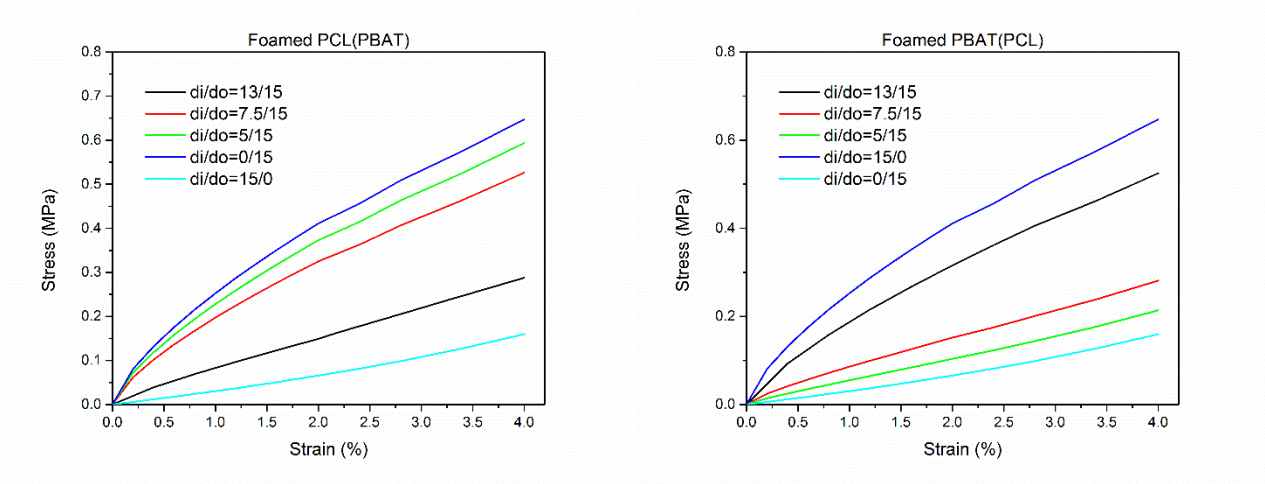

Figure 6-13. Stress strain curve of porous coaxial fibers at different diameter ratios.

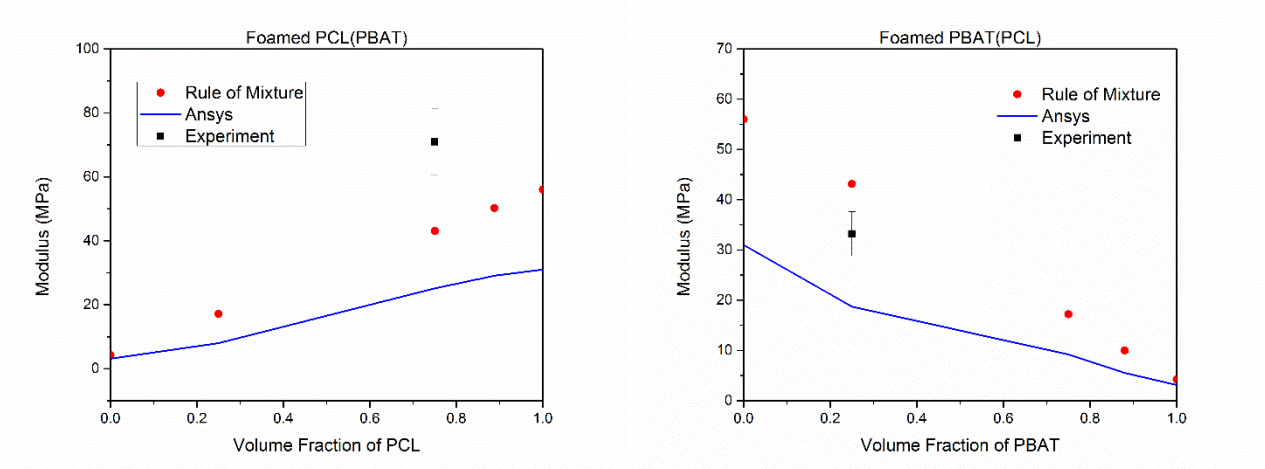

Figure 6-14. Comparison between the modulus values predicted by the rule of mixtures, ANSYS model and experimental values of porous coaxial fibers.

Figure 6-14 shows a comparison between the modulus predicted using rule of mixtures, ANSYS and experimental results for porous coaxial fibers. Both the FEA model and rule of the mixtures under predicted the modulus value as compared to the experimental results for foamed PCL (PBAT) samples, this shows the porous PCL have higher effect when it is attached to the PBAT i.e. the PBAT enhance the mechanical properties of the foamed PCL.

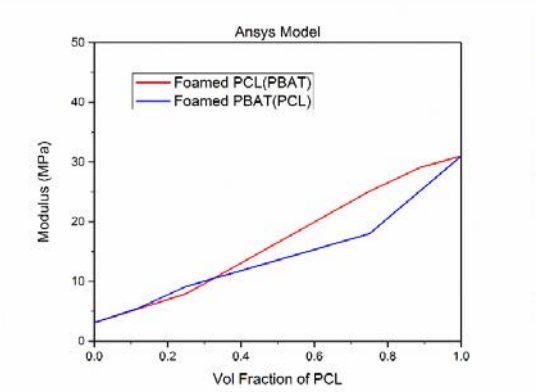

Figure 6-15. ANSYS model for sporous coaxial fibers.

Figure 6-15 shows the effect of the position of porous polymer either in core or skin of fibers on the modulus of the fabric. It can be observed that similar to the solid PCL, porous PCL also has a higher effect once it is on the skin as compare to the core of the fiber.

Table 6-2. Comparison between porous core and porous sheath coaxial fibers.

	Young's Modulus		
	$di/do = 0.866$	$di/do = 0.5$	$di/do = 0.333$
PBAT(PCL)	142 MPa	49.2 MPa	23 MPa
PCL(PBAT)	49.8 MPa	141.4 MPa	165 MPa
Foamed PBAT(PCL)	18.7 MPa	9.2 MPa	5.54 MPa
Foamed PCL(PBAT)	7.97 MPa	25 MPa	29 MPa

6.4 Conclusions

In this chapter, a model based on the tensile properties of the coaxial electrospun fibers was developed using finite element method. The effect of porosity on the mechanical properties of the fiber mesh created due to carbon dioxide foaming was successfully modeled based on hyperelastic and viscoelastic theory. Quasi-static uniaxial and Stress relaxation test for polymer were performed to calibrate the model. Induced porosity causes an increase in the energy absorption of a material. The results obtained from the finite element method effectively predict the mechanical behavior at low strain and in agreement with the experiment. Fibers were designed by varying the diameter of care and skin polymer to obtained modulus values in between 23 MPa to 165 MPa for solid fibers and 5.54 MPa to 29 MPa for the porous fibers. It was also observed that the location of the polymer at skin has a higher effect on the modulus as compared to when it is placed in the core. Foamed PCL modulus increased in the coaxial fibers as compared to the rule of the mixture that can be due to the interaction between the PBAT and porous PCL which enhanced its properties.

6.5 References

[1] Sill, Travis J., Horst A. von Recum, 2008, “Electrospinning: Applications in drug delivery and tissue engineering,” Biomaterials, Vol. 29(13), pp. 1989-2006.

[2] Zander, N.E.; Gillan, M.; Sweetser, D. Recycled PET Nanofibers for Water Filtration Applications. Materials2016, 9, 247

[3] Multiresonant frequency piezoelectric energy harvesters integrated with high sensitivity piezoelectric accelerometer for bridge health monitoring applications.(2017). Smart Materials Research, 2017, 1.

[4] Sander, E. A., Stylianopoulos, T., Tranquillo, R. T., & Barocas, V. H. (2009). Image-based biomechanics of collagen-based tissue equivalents: Multiscale models compared to fiber alignment predicted by polarimetric imaging. IEEE

Engineering in Medicine and Biology Magazine : The Quarterly Magazine of the Engineering in Medicine & Biology Society, 28(3), 10-18.

[5] Kiselev, P., & Rosell-Llompart, J. (2012). Highly aligned electrospun nanofibers by elimination of the whipping motion. Journal of Applied Polymer Science, 125(3), 2433-2441. doi:10.1002/app.36519

[6] Dalrymple, T., Choi, J., and Miller, K., “Elastomer Rate-Dependence: A Testing and Material Modeling Methodology,” Proceedings, Fall 172nd Technical Meeting of the Rubber Division of the American Chemical Society, Inc., Cleveland, OH, 2007

[7] Gorji M, Jeddi AAA, Gharehaghaji AA. The finite element modeling of electrospun PU nanofiber mesh using microstructure architecture analysis. Ind J Textile Fiber Res 2016.

CHAPTER 7

SUMMARY AND FUTURE WORK

7.1 Summary

In this dissertation, efforts are made to produce conductive non-woven fabrics with good mechanical and thermal characteristics. We create non-woven fabric from a new biological precursor (poly caffeyl alcohol) a linear lignin and compared it with commercially available kraft lignin. Electrospinning techniques were used to manufacture non-woven fabric, which was successfully transformed into conductive fibers by carbonization step. Carbonization at 900 °C imparted more graphitic properties to the PCFA carbon than to the Kraft lignin, as seen from G/D ratios of 1.92 vs 1.15 respectively. In this respect, the PCFA-derived carbon compares very well to commercial carbon from PAN and approaches that based on pitch. XPS results show 88% graphitic C-C bond for PCFA as compared to 79% for the Kraft lignin indicating higher crystallinity, which can be correlated to high G/D Raman ratio for PCFA. TGA curves also show higher thermal stability for PCFA indicating higher graphitization. Moreover, from the XRD and TEM a larger crystal size for the PCFA fiber was obtained which is correlates to the higher modulus and conductivity of the fiber. PCFA appears to be a promising new renewable source of both carbon fibers and pure carbon. In order to improve the strength and flexibility of the non-woven carbon fabric, PCFA was blended with the synthetic polymer Poly acrylonitrile (PAN) in 20%, 40%, and 60% concertation. Single and broad glass transition temperature observed from thermal analysis and DMA indicates good miscibility of the two polymers. FTIR results show the presence of characteristics peak of PAN and PCFA in the blends, however, the position of the peaks did not shift significantly indicating

no chemical crosslinking between PCFA and PAN during the electrospinning process. Raman spectroscopy shows an increase in the graphitic content of the blend with the addition of PCFA, resulting in an increase in the electrical conductivity up to (7.7 S/cm) of blend composition, which is enough for sensing and EMI shielding applications. The conductivity of the blended fabric was slightly over predicted by the rule of mixture theory. This shows the contribution of PCFA in a blend is restricted due to the presence of PAN which confines the growth of PCFA crystals and limits conductivity value. The impact of different carbonization condition including carbonization temperature, isothermal time and heating rate individually as well as collectively on the conductivity and architecture of non-woven fabric were analyze using two factorial design of experiment approach (DOE). A two-step manufacturing procedure was develop inspired by the architecture of plant fibers which provides stiffness and flexibility to the structure. Coaxial electrospinning and CO_2 foaming technique were used to introduce controlled porosity either on the skin or core of the fibers. Results show depending on the CO_2 miscibility to the polymer we can successfully manipulate the architecture of the cross-section of the electrospun fiber and can tailor to the required application. Hyperelastic and viscoelastic material model were develop using Finite Element analysis to design for the mechanical properties of the non-woven mesh. Results comparison to the experimental values indicates that polymers contribute less in a coaxial design as compared to the individual fibers for mechanical properties expect for foamed PCL(PBAT) sample where the supporting polymer enhanced the properties as compared to the individual fibers. Moreover, It was also observed that the location of the polymer at skin have a higher effect on the modulus as compared to when it is placed in the core. The manufacturing method developed can be

utilized for hierarchical functionalization of fibers by incorporating different conductive nanoparticles at a different level of fiber cross section for sensing applications in medical and sports industry.

7.2 Future Work

Conductivity and mechanical characteristics of the non-woven fabrics can be further be increased or tailored to the individual application using the manufacturing techniques and optimization tool presented in this dissertation. The future work will be directed to improve the conductivity by hierarchical functionalization of fiber cross-section by incorporating different conductive nanoparticles at different levels. These conductive fabrics can be used in an organic battery and fuel cell. Moreover, Incorporation of piezoelectric nanoparticles on the high surface area provides by porous fibers can be used for energy harvesting applications.